Search for non-Gaussian Signatures in the Cosmic Microwave Background Radiation
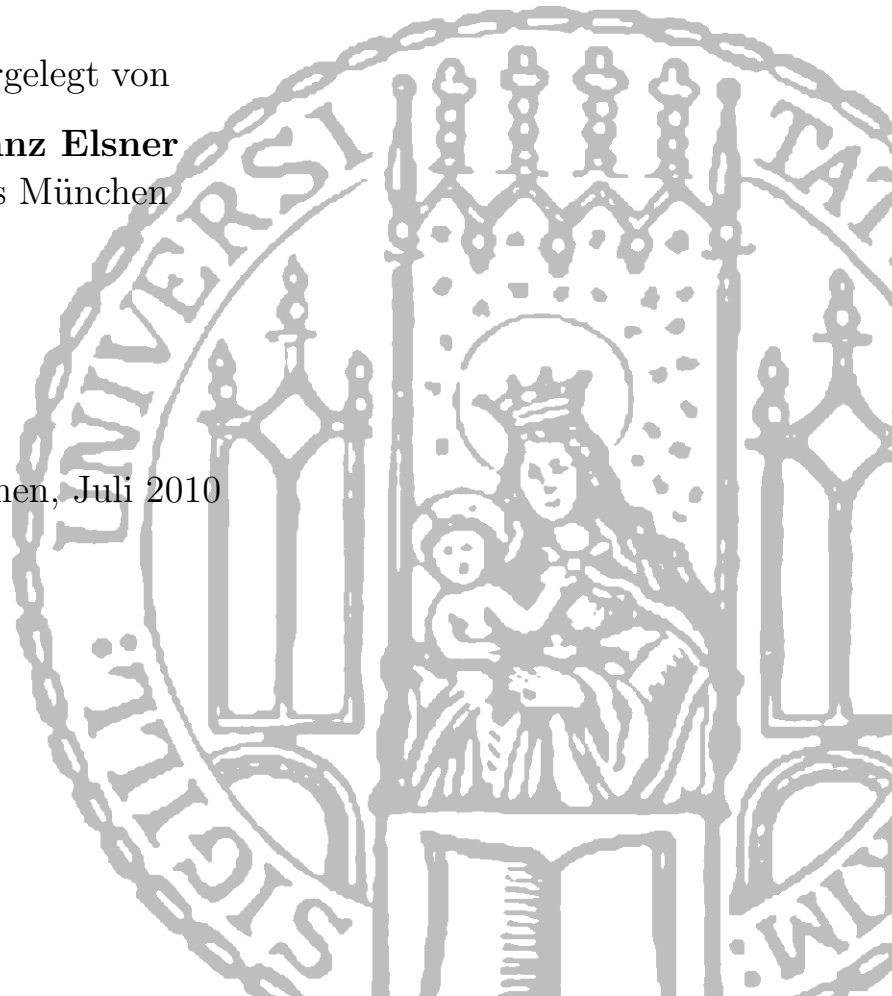
Dissertation

Fakultät für Physik
Ludwig-Maximilians-Universität München

vorgelegt von

Franz Elsner
aus München

München, Juli 2010

Erster Gutachter: Prof. Simon White
Zweiter Gutachter: Prof. Jochen Weller

Tag der mündlichen Prüfung: 19. November 2010

O glücklich, wer noch hoffen kann,
Aus diesem Meer des Irrtums aufzutauchen!
Was man nicht weiß, das eben brauchte man,
Und was man weiß, kann man nicht brauchen.

<div align="right"><i>Johann Wolfgang von Goethe</i>, Faust</div>

Zusammenfassung

Dem vorherrschenden Paradigma zufolge wurden die beobachteten Anisotropien der Mikrowellenhintergrundstrahlung in einer frühen Phase inflationärer Expansion des Universums erzeugt. Die einfachsten Modelle zur Beschreibung dieser Ära sagen nahezu perfekt Gaussförmige primordiale Fluktuationen voraus, allerdings können in naheliegender Weise konkurrierende Theorien formuliert werden, die einen wesentlich höheren nicht-Gaussförmigen Beitrag erwarten lassen. Damit wird aus der Suche nach Signaturen dieser Art ein grundlegendes Verfahren, die physikalischen Prozesse während der inflationären Phase des Universums näher zu bestimmen.

Ziel dieser Arbeit ist es, eine Bayesianische Methode zur Messung des nicht-Gaussförmigen Anteils lokaler Form in der Mikrowellenhintergrundstrahlung zu erarbeiten. Bayesianische Statistik legt großen Wert auf eine konsistente Formulierung des Problems, weiterhin werden die Fehlerbalken des Messwerts auf der Grundlage des jeweiligen Datensatzes bestimmt. Der erste Schritt besteht in der Entwicklung eines exakten Algorithmus zur Simulation von Temperatur- und Polarisationskarten der Mikrowellenhintergrundstrahlung mit beliebigem nicht-Gaussförmigen Beitrag. Ein Optimierungsschema erlaubt es, die Präzision der Simulationen vorherzusagen und aktiv zu steuern. Auf seiner Grundlage kann die numerische Effizienz des Programms gegenüber bisherigen Implementationen um eine Größenordnung verbessert werden. Der nächste Schritt gilt der Entwicklung des Formalismus zur Bayesianischen Extraktion des Anteils an nicht-Gaussförmigkeit. Wir benutzen einen Hamiltonschen Monte Carlo Algorithmus, um Zufallszahlen von der zugrunde liegenden Wahrscheinlichkeitsverteilung zu ziehen. Mit Hilfe dieser Zufallszahlen ist es möglich, die a-posteriori-Wahrscheinlichkeitsdichte des Anteils an nicht-Gaussförmigkeit in Abhängigkeit der Daten zu konstruieren. Die Anwendbarkeit des Schemas wird anhand eines vereinfachten Datenmodells demonstriert. Abschließend implementieren wir die nötigen Gleichungen für ein realistisches Experiment zur Vermessung der Mikrowellenhintergrundstrahlung, mit der Fähigkeit, anisotroper Rauschcharakteristik und lückenhafter Himmelsabdeckung Rechnung zu tragen. Ein direkter Vergleich zwischen herkömmlichem frequentistischen Schätzer und exaktem Bayesianischen Ansatz zeigt die Vorteile der neu entwickelten Methode. Bei einem signifikanten Nachweis eines nicht-Gaussförmigen Beitrags verhält sich der Schätzer nicht optimal – das Bayesianische Schema hingegen liefert immer die engstmöglichen Fehlergrenzen.

Abstract

The tremendous impact of Cosmic Microwave Background (CMB) radiation experiments on our understanding of the history and evolution of the universe is based on a tight connection between the observed fluctuations and the physical processes taking place in the very early universe. According to the prevalent paradigm, the anisotropies were generated during the era of inflation. The simplest inflationary models predict almost perfectly Gaussian primordial perturbations, but competitive theories can naturally be constructed, allowing for a wide range in primordial non-Gaussianity. For this reason, the test for non-Gaussianity becomes a fundamental means to probe the physical processes of inflation.

The aim of the project is to develop a Bayesian formalism to infer the level of non-Gaussianity of local type. Bayesian statistics attaches great importance to a consistent formulation of the problem and properly calculates the error bounds of the measurements on the basis of the actual data. As a first step, we develop an exact algorithm to generate simulated temperature and polarization CMB maps containing arbitrary levels of local non-Gaussianity. We derive an optimization scheme that allows us to predict and actively control the simulation accuracy. Implementing this strategy, the code outperforms existing algorithms in computational efficiency by an order of magnitude. Then, we develop the formalism to extend the Bayesian approach to the calculation of the amplitude of non-Gaussianity. We implement an exact Hamiltonian Monte Carlo sampling algorithm to generate samples from the target probability distribution. These samples allow to construct the full posterior distribution of the level of non-Gaussianity given the data. The applicability of the scheme is demonstrated by means of a simplified data model. Finally, we fully implement the necessary equations considering a realistic CMB experiment dealing with partial sky coverage and anisotropic noise. A direct comparison between the traditional frequentist estimator and the exact Bayesian approach shows the advantage of the newly developed method. For a significant detection of non-Gaussianity, the former suffers from excess variance whereas the Bayesian scheme always provides optimal error bounds.

Contents

Chapter 1

Introduction

1.1 A cosmic review

Since the 1970's, theoretical cosmology has made substantial progress in providing a comprehensive and consistent description of the history of the universe. With the development of new concepts in particle physics—in particular the gauge theories of weak, electromagnetic, and strong interactions—it was possible to extrapolate the matter equation of state beyond nuclear densities. Thereby, the properties of the elementary particles under extreme conditions were realized to differ fundamentally from what we observe in the low energy limit. Around that time, the concept of unifying weak, electromagnetic, and strong forces in phase transitions at high energies was introduced, pointing towards the fact that also the understanding of the fundamental interactions had to be revised.

Roughly one decade later, observational cosmology has entered its golden age. With the advent of novel technologies, new experiments became feasible resulting in a vastly increasing amount of astronomical data. For example, the introduction of large telescopes with sensitive spectrographs has led to the compilation of comprehensive galaxy catalogs, containing not only the angular position of the sources, but also additional redshift information (e.g. the *Center for Astrophysics Redshift Survey*, Huchra et al. 1983; the *Southern Sky Redshift Survey*, da Costa et al. 1998; the *2dF Galaxy Redshift Survey*, Colless 1999; the *Sloan Digital Sky Survey*, York et al. 2000; or the *6df Galaxy Survey*, Jones et al. 2004). By means of these catalogs, three-dimensional maps of the galaxy distribution could have been generated in
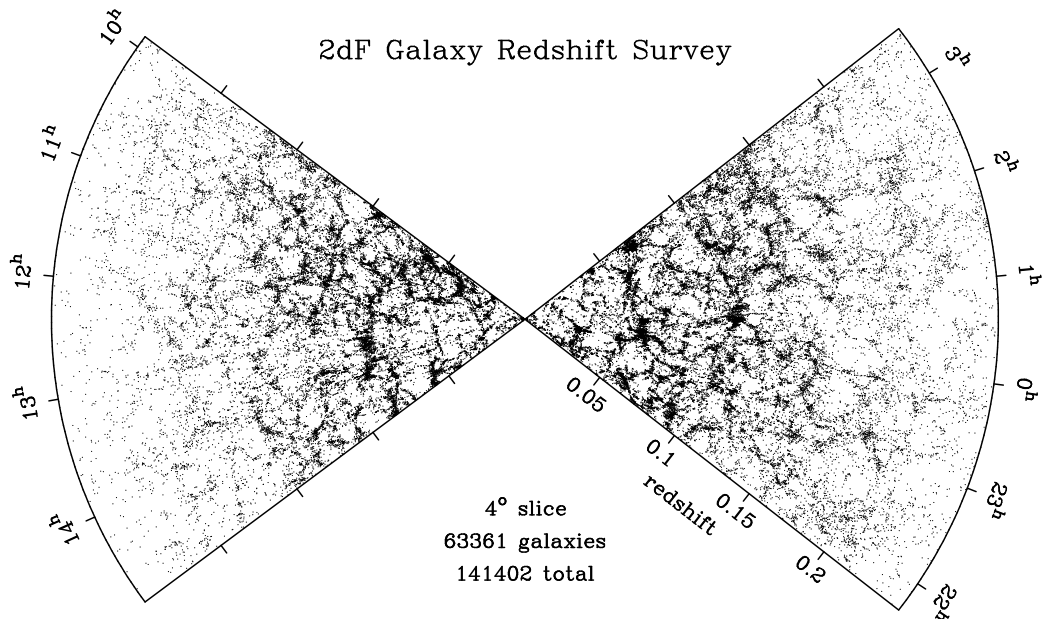
Figure 1.1: Distribution of galaxies. We show a map of the large scale structure constructed out of the *2dF Galaxy Redshift Survey* galaxy catalog. The slices are 4° in thickness (image courtesy of Peacock et al. 2001).

order to obtain a statistically meaningful representation of the large scale structure of the universe (Fig. 1.1). Another pillar of cosmology is the observation of the cosmic microwave background (CMB) radiation (Fig. 1.2). After the first detection by Penzias & Wilson (1965), detailed measurements of its anisotropies have turned out to be one of the most important sources of information in cosmology (e.g. by the *Cosmic Background Explorer* satellite, Smoot et al. 1992; Wright et al. 1992; the *Balloon Observations of Millimetric Extragalactic Radiation and Geophysics* experiment, Netterfield et al. 2002; Sievers et al. 2003; the *Wilkinson Microwave Anisotropy Probe* satellite, Bennett et al. 2003a; Spergel et al. 2003; the *Arcminute Cosmology Bolometer Array Receiver*, Kuo et al. 2004; or the *Degree Angular Scale Interferometer*, Leitch et al. 2005). With the increasing amount of observational data, it became possible to test the predictions of various theoretical models in detail. As a result, cosmology has evolved from a merely speculative to an evidence-based science over the last century.

4

Figure 1.2: The Cosmic Microwave Background radiation. We illustrate the CMB radiation full-sky map at $33\,GHz$ (*upper panel*) and $94\,GHz$ (*lower panel*) as observed by the *Wilkinson Microwave Anisotropy Probe* in galactic coordinates. The frequency dependent c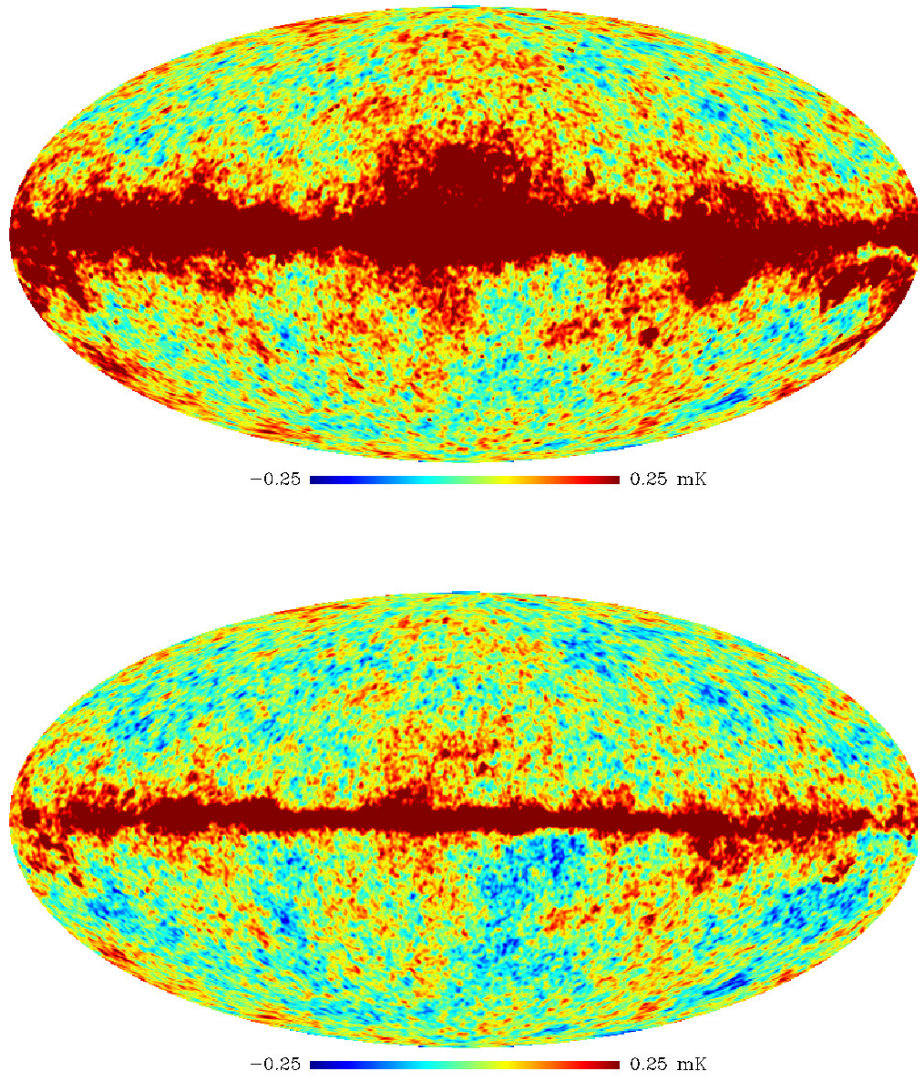ontribution of secondary sources due to galactic dust, synchrotron, and free-free emission is clearly visible at low latitudes.

The collation of fundamental results from theory and experiments has finally led to the formulation of the prevalent cosmological paradigm, the so called Λ-Cold Dark Matter (ΛCDM) cosmology (e.g. Linde 1990b; Dodelson 2003; Mukhanov 2005). That is, the evolution of the universe, which emerged in a hot big bang from an initial singularity, is governed by its dark energy and cold dark matter content. The theory is based on the *cosmological principle*, the cornerstone of modern cosmology, which postulates homogeneity and isotropy of the universe on scales larger than about $100\,Mpc$. A timeline of the history of the universe according to the standard model can be summarized as follows:

- *Planck epoch, $t < 10^{-43}\,s$.*
  Close to the Planck scale, the classical description of space-time brakes down. Here, a non-perturbative theory of quantum gravity is required. Although promising candidate theories exist (e.g. string theory, loop quantum gravity), the physical processes at the highest energies ($T > 10^{19}\,GeV$) remain to be understood.

- *Epoch of grand unification, $t \approx 10^{-36}\,s$.*
  According to theories of grand unification (GUT), at energies above $T \approx 10^{16}\,GeV$ all fundamental forces except for gravity are unified. Topological defects and many exotic particle species have probably been produced in this era. The theory of general relativity becomes appropriate to describe the dynamics of the universe.

- *Electroweak epoch, $t \approx 10^{-10}\,s$.*
  The strong force has now decoupled from the electroweak force in a phase transition. Baryon and fermion number violating processes are taking place. The energy scale of $T \approx 10^3\,GeV$ is directly accessible to experiments conducted on present day accelerators.

- *Quark epoch, $t \approx 10^{-5}\,s$.*
  After electroweak symmetry breaking, the fundamental forces have taken their present form. The universe was filled with a hot quark-gluon plasma, containing quarks, leptons and their antiparticles. According to the standard model of particle physics, the particle masses emerge from symmetry breaking via the Higgs mechanism.

- *Hadron epoch, $t \approx 10^{-1}\,s$.*
  The free quark-gluon plasma becomes confined in baryons and mesons.

6

The ratio of neutrons to protons freezes out. At about one second after the big bang, neutrinos decouple and start to stream freely through the universe.

- *Big bang nucleosynthesis, $t \approx 10^2 \, s$.*
  As nuclear reaction rates level off, the primordial nucleosynthesis sets in and starts to burn light elements. Besides 25% of helium, traces of deuterium, lithium, and beryllium have been produced.

- *Photon epoch, $t \approx 10^9 \, s$.*
  Due to the large entropy of the universe, its dominating constituent remains radiation until approximately $60\,000 \, yr$ after the big bang. Finally, after about $380\,000 \, yr$, atoms form and the universe becomes transparent, i.e. the mean free path of the CMB photons now is larger than the Hubble radius.

The fundamental parameters of the standard model of cosmology as obtained from a joint analysis of *Wilkinson Microwave Anisotropy Probe* (WMAP) data, baryon acoustic oscillations (BAO), and supernova (SN) experiments, are provided in table Table 1.1.

In the following, we briefly review the cosmological standard model, some of its problems, and their solutions as proposed within the framework of inflation. An overview with the focus on the discussion of inflation or the CMB radiation is given by, e.g., Mukhanov et al. (1992); Frieman (1994); Lyth & Riotto (1999); Brandenberger (1999); Bartolo et al. (2004); Burgess (2007); Linde (2008); Baumann (2009); Kinney (2009); Bartolo et al. (2010); Brandenberger (2010); Chen (2010); Liguori et al. (2010); Wands (2010). See also the textbooks of, e.g., Linde (1990b); Liddle & Lyth (2000); Dodelson (2003); Mukhanov (2005); Weinberg (2008).

1.2 Standard cosmology

1.2.1 Overview

Most of the cosmological observations can be explained within a simple hot big bang model, where the universe emerged out of an initial singularity with infinite temperature and density. Over time, the subsequent expansion led

Table 1.1: Cosmological parameters from WMAP7 + BAO + SN in ΛCDM cosmology (Komatsu et al. 2010)

Description	Symbol	Value
Hubble constant	H_0	$69.9 \pm 1.3 \, km \, s^{-1} \, Mpc^{-1}$
Age of the universe	t_0	$13.8 \pm 0.1 \, Gyr$
Baryon density	Ω_b	0.0461 ± 0.0015
Dark matter density	Ω_c	0.232 ± 0.013
Dark energy density	Ω_Λ	0.722 ± 0.015
Curvature fluctuation amplitude[1]	$\Delta_\mathcal{R}$	$(2.46 \pm 0.09) \times 10^{-9}$
Scalar spectral index	n_s	0.960 ± 0.13
Redshift of radiation-matter equality	z_{equ}	3249 ± 83
Redshift of decoupling	z_{dec}	1088.4 ± 1.1

[1]at $k = 2 \cdot 10^{-3} Mpc^{-1}$

to an adiabatic cool down to the temperature we observe nowadays in the CMB radiation, $T_{CMB} = 2.73 \, K$ (Fixsen et al. 1996).

The quantitative mathematical treatment of this process is based on Friedmann-Lemaître-Robertson-Walker (FLRW) space-times, the most general ansatz in agreement with the fundamental symmetries postulated by the cosmological principle (Friedmann 1922, 1924; Lemaître 1927; Robertson 1935, 1936a,b; Walker 1935). Here, the metric $g_{\mu\nu}$ takes a simple form in comoving spherical coordinates (r, θ, ϕ),

$$
\begin{aligned}
ds^2 &= g_{\mu\nu} dx^\mu dx^\nu \\
&= dt^2 - a(t)^2 \left[\frac{dr^2}{1 - \kappa r^2} + r^2 (d\theta^2 + \sin^2\theta d\phi^2) \right] ,
\end{aligned} \tag{1.1}
$$

where a is the time dependent scale factor, and the parameter $\kappa = -1, 0, 1$ determines the spatial curvature of the universe to be open, flat, or closed, respectively.

Now, it is straightforward to derive Hubble's law. Consider an object locally at rest, the physical distance to the origin reads

$$
x_{proper} = a(t) \, x_{comoving} . \tag{1.2}
$$

Using an overdot to indicate a derivative with respect to physical time, we obtain for the apparent motion

$$\dot{x}_{proper} = \dot{a}\, x_{comoving} \tag{1.3}$$

$$= \frac{\dot{a}}{a}\, x_{proper} \tag{1.4}$$

$$= H\, x_{proper}\,, \tag{1.5}$$

where we have introduced the Hubble parameter $H \equiv \dot{a}/a$ as factor of proportionality. The redshift of objects observed over cosmological distances can therefore be attributed to a global expansion of the universe (Lemaître 1927; Hubble 1929).

The dynamical evolution of the universe is governed by the Einstein equations (Einstein 1916),

$$R_{\mu\nu} - \frac{1}{2}g_{\mu\nu}R - \Lambda g_{\mu\nu} = 8\pi G\, T_{\mu\nu}\,. \tag{1.6}$$

Here, the indices run from $\mu, \nu = 0, \ldots 3$, $R_{\mu\nu}$ and R is the Ricci tensor and Ricci scalar, respectively, and the speed of light was set to unity. We further introduced the cosmological constant Λ, Newton's constant G, and the energy-momentum tensor, denoted by $T_{\mu\nu}$. Considering a homogeneous and isotropic universe (i.e. $T = diag(\rho, -p, -p, -p)$, where ρ is the energy density and p the pressure), we obtain the Friedmann equations (Friedmann 1922, 1924),

$$\left(\frac{\dot{a}}{a}\right)^2 + \frac{\kappa}{a^2} = \frac{8\pi G}{3}\,\rho + \frac{\Lambda}{3} \tag{1.7}$$

$$\frac{\ddot{a}}{a} = -\frac{4\pi G}{3}\,(\rho + 3p) + \frac{\Lambda}{3}\,. \tag{1.8}$$

Combining the two Friedmann equations, we derive the energy conservation equation,

$$\dot{\rho} + 3H(\rho + p) = 0\,, \tag{1.9}$$

which may also be written in terms of the of covariant derivative of the energy-momentum tensor, $T^{\mu\nu}{}_{;\nu} = 0$.

Regarding the constituents of the universe as perfect fluid at rest and parametrizing the equation of state by $p = w\rho$, we obtain the scaling relation

of the energy density for different particle species in an evolving universe from Eq. 1.9. For cold, non-relativistic matter $(w = 0)$, we find

$$\rho_m \propto a^{-3}, \tag{1.10}$$

whereas for radiation $(w = 1/3)$, we obtain a different scaling,

$$\rho_\gamma \propto a^{-4}. \tag{1.11}$$

The third relevant case we consider is a cosmological constant with equation of state $w = -1$. Here, we get

$$\rho_\Lambda = const., \tag{1.12}$$

i.e. the energy density is independent of the evolution of the scale factor. In an expanding universe with $\Lambda > 0$, the cosmological constant will therefore eventually dominate over all other species. For the cosmological parameters as provided in Table 1.1, we sketch the evolution of $\rho_{m, \gamma, \Lambda}$ in Fig. 1.3.

1.2.2 Problems of standard cosmology

Whereas being very successful in explaining important fundamental properties of the universe, the standard model of cosmology is faced with several serious issues that have been the driving force for a major revision. We will discuss three of them in greater detail in the following.

One problem is known as *flatness problem*, the fact that the total energy density of today's universe is remarkably close to the critical density, $-0.018 < \Omega_{tot} - 1 \equiv \rho_{tot}/\rho_{crit} - 1 < 0.006$ at 2-σ level (Komatsu et al. 2010). This observation has no natural explanation within the standard model of cosmology. Setting $\Lambda = 0$ for simplicity, we rewrite Eq. 1.7 in terms of the critical density $\rho_{crit} \equiv 3H^2/8\pi G$,

$$\rho\, a^2 - \rho_{crit}\, a^2 = \frac{3\kappa}{8\pi G}$$
$$\Leftrightarrow \frac{\Omega_{tot} - 1}{\Omega_{tot}} \rho\, a^2 = \frac{3\kappa}{8\pi G} = const. \tag{1.13}$$

For an universe dominated by matter or radiation, the product $\rho\, a^2$ scales as $\rho_m\, a^2 \propto a^{-1}$ or $\rho_\gamma\, a^2 \propto a^{-2}$, respectively (Eq. 1.10 et seq.). In order to explain the present day value of $\Omega_{tot} \approx 1$, the initial energy density had to
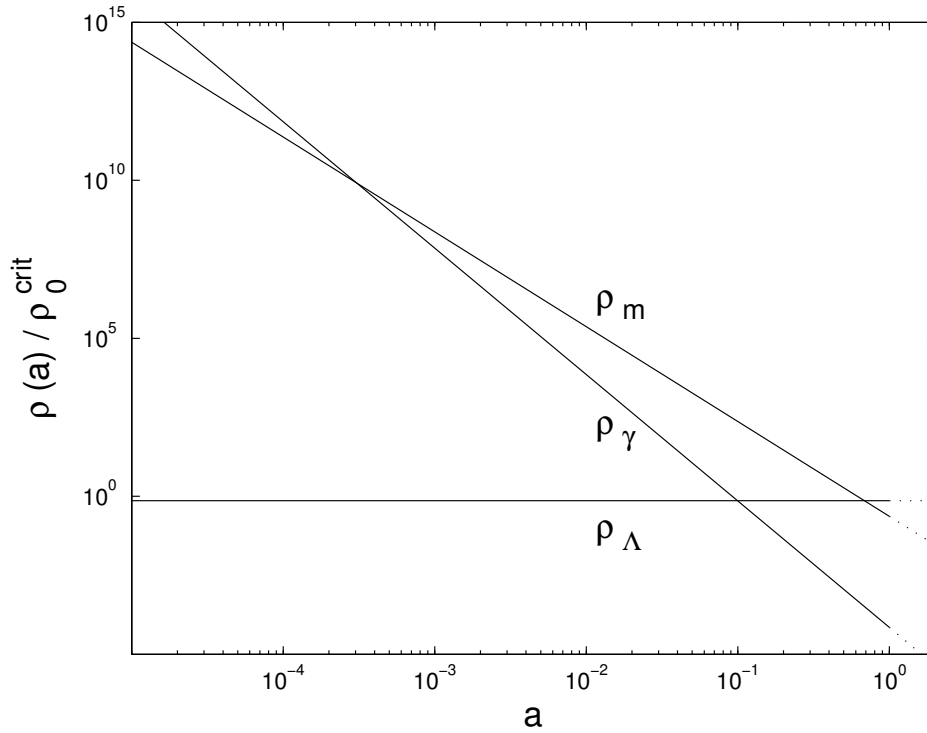
Figure 1.3: Evolution of energy density with scale factor. We show the energy density of radiation (ρ_γ), matter (ρ_m), and vacuum energy (ρ_Λ) normalized to the present day critical density $\rho_0^{crit} \equiv 3H_0^2/8\pi G$ as a function of the scale factor a. Radiation-matter equality happened around $z_{eq} = 3250$, the vacuum energy became dominant at a redshift of about $z = 0.5$.

be extremely close to the critical density. Extrapolating backwards in time to an energy of about $T = 10^{15}\,GeV$, for example, the deviation from unity was bounded by roughly

$$\frac{|\Omega_{tot} - 1|}{\Omega_{tot}} < 10^{-50}\,, \tag{1.14}$$

requiring an extreme amount of fine-tuning.

Another issue is the so called *horizon problem*. Observations of the CMB radiation have revealed a black body spectrum that is extremely isotropic over the entire sky, with characteristic fluctuations of the order 10^{-5} (Jarosik et al. 2010). A comparison between the past and the future light cone to recombination,

$$
\begin{aligned}
l_p &= \int_{t_{rec}}^{t_0} \frac{dt}{a} \\
&\approx 3\, t_0^{2/3}(t_0^{1/3} - t_{rec}^{1/3}) \\
l_f &= \int_{0 = t_{BB}}^{t_{rec}} \frac{dt}{a} \\
&\approx 3\, t_0^{2/3}\, t_{rec}^{1/3}\,,
\end{aligned}
\tag{1.15}
$$

reveals the former to be considerably larger than the latter, $l_p \gg l_f$ (see also left-hand panel in Fig. 1.4). This poses a serious problem within standard cosmology; according to Eqs. 1.15, the observable universe would have emerged from a huge number of causally disconnected regions which had never been in thermal equilibrium with each other. The almost perfect isotropy found in CMB radiation experiments remains unexplained.

The related *problem of structure formation* in standard cosmology is based on observational evidence for a nonrandom correlation between clusters of galaxies on scales as large as $100\,Mpc$ and beyond (see, e.g., Eisenstein et al. 2005). If the initial density perturbations were produced before recombination, the distance between them is too large to explain the correlation among them by causal processes (see right-hand panel in Fig. 1.4). This issue appears in standard FLRW cosmologies, as the Hubble radius increases faster than space expands. Therefore, primordial perturbations always enter the horizon from the outside, and on no account leave it from the inside. Furthermore, gravity alone turns out to be too weak to provide the seeds for structure formation on the larges scales after recombination. Hence, the

12
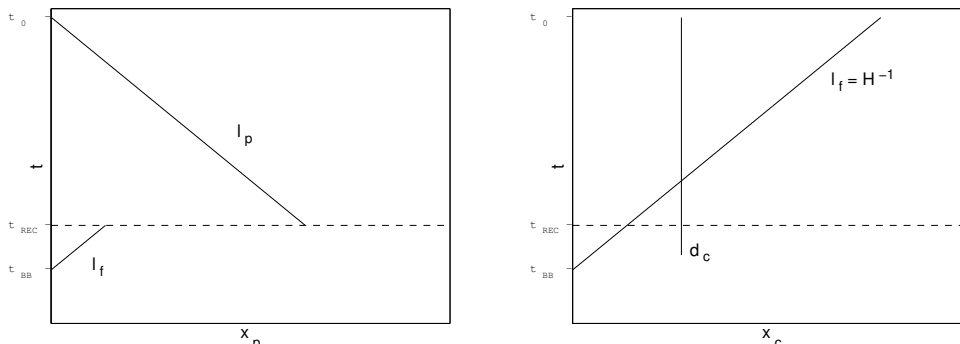
Figure 1.4: Qualitative space-time diagrams in standard cosmology. The horizon problem in physical coordinates versus time (*left panel*): The future light cone l_f from big bang to recombination is much smaller than the past light cone l_p from today to recombination. The structure formation problem in comoving coordinates versus time (*right panel*): The comoving distance d_c between two clusters is larger than the Hubble radius $c\,H^{-1}$ at recombination. (Plots after Brandenberger 1999.)

question of the origin of the primordial density perturbations and the observed large scale correlation cannot be answered satisfactorily within the framework of standard cosmology.

It is important to note that the problems discussed so far do not render the standard model of cosmology invalid, they only lack a sound explanation. The history of the universe can consistently be explained if we postulate a set of carefully adjusted initial conditions. We need to assume that the universe began homogeneously on superhorizon scales with exactly the right amplitude of fluctuations to explain the process of structure formation. Furthermore, in the beginning, the initial value of the total energy density must have been extremely close to unity to be consistent with observations. As such an universe needs an enormous amount of fine tuning, a theory seems desirable which naturally transforms a wide range of initial conditions to values that give rise to an universe similar to ours. As we will show in the next section, inflation is capable of doing so.

1.3 Inflation

1.3.1 The foundations of inflation

In order to find a natural solution to the problems outlined in Sect. 1.2.2, scientists have revised the standard model of cosmology to include the epoch of inflation. This theory makes strict predictions about the large scale structure of the universe on the basis of well understood mechanisms (Guth 1981; Sato 1981; Albrecht & Steinhardt 1982; Linde 1982; Bardeen et al. 1983; Linde 1983; Mukhanov 1985, see also the earlier work of Starobinskiĭ 1980).

The key feature of inflationary cosmology is that the scale factor of the universe underwent a phase of exponential expansion,

$$a(t) \propto e^{Ht} \,, \tag{1.16}$$

where the Hubble parameter H stayed (almost) constant over time. The expansion was driven by gravity which acted as a repulsive force during this period. According to the model, inflation set in subsequent to the GUT phase transition at a temperature of roughly $10^{15} \, GeV$ and was finished about $10^{-33} \, s$ after the big bang.

The postulation of such a period allows to easily address the flatness problem of standard cosmology (Linde 1982). Inflation strictly predicts the universe to be flat on cosmological scales, i.e. $\Omega_{tot} \equiv 1$. Any potentially large curvature that may have existed prior to the phase of accelerated expansion gets stretched to scales much larger than the Hubble radius and therefore becomes unobservable. This fact can be described quantitatively using Eq. 1.7. Assuming $\Lambda = 0$ for simplicity, we rewrite it to read

$$\Omega_{tot}(a) - 1 = \frac{\kappa}{a^2 H^2} \,. \tag{1.17}$$

During inflation, a vastly increased while the Hubble parameter H remained constant; the solution $\Omega_{tot} = 1$ becomes an attractor for any initial spatial curvature κ. From observations, we find that the scale factor has grown by more than about 60 e-folds during inflation (Baumann 2009), a constraint that can also be obtained from entropy considerations (Brandenberger 1999). Note that we can only provide a lower limit to the expansion rate as an upper bound can neither be inferred from theory, nor from observations.

Also, the era of inflation offers a natural solution to the horizon problem. During inflation, the scale factor underwent a phase of accelerated growth,
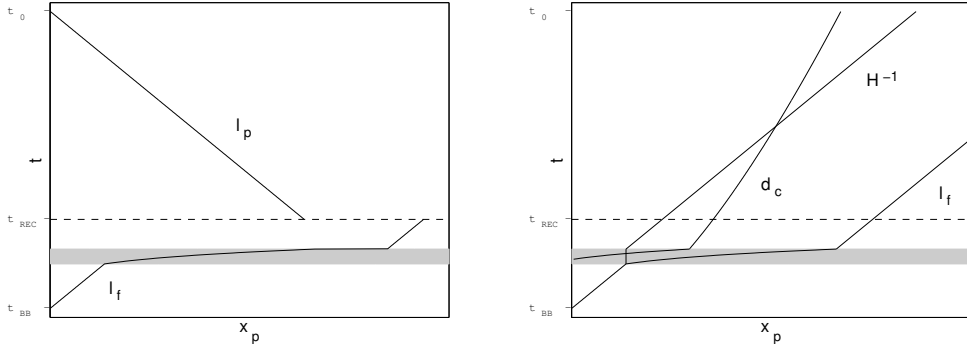
Figure 1.5: Same as Fig. 1.4, but revised to include the epoch of inflation (grayish regions). Solution to the horizon problem in physical coordinates versus time (*left panel*): Taking into account a period of exponential expansion, the future light cone l_f encloses the past light cone l_p. Solution to the structure formation problem in physical coordinates versus time (*right panel*): The distance d_c starts out within the Hubble radius, crosses the horizon and re-enters at later time. It never falls outside the future light cone. (Plots after Brandenberger 1999.)

$\ddot{a} > 0$, such that a finally increased much faster than the cosmic time t (see left-hand panel in Fig. 1.5). As a result, the future light cone from big bang to recombination expanded exponentially and now easily encloses the past light cone to recombination. Therefore, the formerly causally disconnected areas building up the source region of the CMB radiation had been into contact with each other before.

The problem of structure formation can be explained in a similar fashion (Fig. 1.5, right-hand panel). According to the theory of inflation, the seeds present day structure evolved from, were generated by quantum fluctuations on microscopic scales (Mukhanov & Chibisov 1981; Guth & Pi 1982; Hawking 1982; Starobinskiĭ 1982). As these diminutive dimensions get stretched out by many orders of magnitude, the correlations we observe on the largest scales naturally emerged out of fluctuations on small patches with well defined statistical properties.

15

1.3.2 A simple inflationary model

As we find inflation to be a very promising candidate to solve several problems encountered in standard cosmology, we now address the question of how to realize a phase of exponential expansion on the basis of known physical processes.

For inflation to be realized successfully, the Friedmann (Eq. 1.7) together with the continuity equation (Eq. 1.9) constrain the energy density to be dominated by a fluid with equation of state parameter $w = -1$. Although satisfying this condition, dark energy, today's dominant contribution to the total energy budget of the universe, could not have been the driving force behind inflation. As its energy density ρ_Λ remains constant during expansion, it was completely negligible in the radiation dominated epoch of the early universe (Fig. 1.3).

A quantitative calculation of the relevant processes relies on classical general relativity as a method to describe space and time, and quantum field theory (QFT) as a means to describe particle fields and interactions. In general, QFT deals with matter fields (fermions, spin 1/2 particles), and bosons as gauge bosons with spin 1, or scalar fields with spin 0 (e.g. Ryder 1996; Weinberg 1996; Zee 2003). To discuss the basic properties of the inflationary mechanism, we review a simple model in greater detail in what follows.

In a simple model, one postulates the existence of a dominating scalar field ϕ, the *inflaton*. We derive its dynamical evolution from the variation principle assuming the action

$$\mathcal{S} = \int d^4x \sqrt{-g} \left(\frac{1}{2} R + \mathcal{L}_\phi \right) , \qquad (1.18)$$

where $g \equiv \det(g_{\mu\nu})$ is the determinant of the metric, and R the Ricci scalar (e.g. Mukhanov 2005; Baumann 2009). We suppose a minimal coupling to gravity which neglects a back-reaction of the metric to the inflaton field. Variation of the action with respect to the first term results in Eqs. 1.6, the Einstein equations. The Lagrangian $\mathcal{L}_\phi$ is constrained by gauge invariance and renormalizability, and takes the form

$$\mathcal{L}_\phi = \frac{1}{2} g^{\mu\nu} \partial_\mu \phi \, \partial_\nu \phi - V(\phi) , \qquad (1.19)$$

consisting of the canonical kinetic term $T \propto (\partial\phi)^2$, and the inflaton potential V, describing the field's self-interaction. Obtaining the energy-momentum

tensor by varying the action with respect to the metric results, for a flat space-time, in the ϕ-depended contribution to the pressure and density,

$$p_\phi = \frac{1}{2}\dot{\phi}^2 - V(\phi)\,, \tag{1.20}$$

$$\rho_\phi = \frac{1}{2}\dot{\phi}^2 + V(\phi)\,. \tag{1.21}$$

Spatial variations $\nabla\phi$ have been neglected in the above expressions as they will be smoothed out shortly after the onset of inflation. The equation of state of such a scalar field, $p = -\rho + \dot{\phi}^2$, shows almost the desired structure. In the limit of a vanishing kinetic term, i.e. a potential dominated expression for pressure and energy density, an inflationary epoch can be realized. Furthermore, the equation of state offers a natural explanation for the end of inflation. When the kinetic term becomes important, the approximation $w = -1$ brakes down and inflation terminates.

The dynamics of the inflaton field is described by the Klein-Gordon equation

$$\ddot{\phi} + 3H\dot{\phi} + V'(\phi) = 0\,, \tag{1.22}$$

which shows the same structure as the equation of motion of a harmonic oscillator with friction term (Linde 1990b). It is now possible to further quantify the conditions for the potential V under which an inflationary period can be realized. From the Friedman equations (Eq. 1.7 et seq.), we derive an expression for the so called slow-roll parameter ϵ,

$$\begin{aligned}
\frac{\ddot{a}}{a} &= -\frac{4\pi G}{3}\rho\left(1 + 3w\right) \\
&= H^2\left[1 - \underbrace{3/2\left(w + 1\right)}_{\equiv\epsilon}\right]\,,
\end{aligned} \tag{1.23}$$

which can be expressed in terms of the Hubble parameter,

$$\epsilon = -\frac{\dot{H}}{H^2}\,. \tag{1.24}$$

To sustain accelerated expansion, $\epsilon < 1$ is mandatory. For inflation to last long enough, the second time derivative of the inflaton field must be small. This condition is usually expressed in terms of a second slow-roll parameter, η,

$$\eta \equiv -\frac{\ddot{\phi}}{H\dot{\phi}}\,. \tag{1.25}$$

17

Imposing $|\ddot{\phi}| < |3H\dot{\phi}|$, $|\ddot{\phi}| < |V'|$ is equivalent to the constraint $|\eta| < 1$.

If the above mentioned conditions are met, i.e. $\epsilon < 1$ and $|\eta| < 1$, we find for the dynamical evolution of the variables from Eq. 1.7 and Eq. 1.22

$$H \approx \sqrt{\frac{1}{3} V(\phi)}$$
$$\approx const. \tag{1.26}$$
$$\dot{\phi} \approx -\frac{V'}{3H}\,, \tag{1.27}$$

thus, an exponential increase of the scale factor,

$$a(t) \propto \mathrm{e}^{Ht}\,, \tag{1.28}$$

until inflation terminates when finally $\epsilon(\phi_f) = 1$ is reached. As an example of a potential fulfilling the requirements, a Coleman-Weinberg type potential (Coleman & Weinberg 1973) is shown on the left-hand side in Fig. 1.6.

During inflation, the universe expanded by at least a factor of 10^{30}. Its constituents, i.e. radiation and particles, potentially contributing substantially to the energy density prior to inflation, have been extremely diluted. At the end of inflation, the temperature had dropped down to essentially zero; the universe was cold and empty except for the scalar inflaton field. Shortly afterwards, the inflaton decayed completely and all of its energy was injected into the particle sector; this epoch is called *reheating* (Abbott et al. 1982; Kofman et al. 1994, 1997). During reheating, the temperature increased to about its original value and the universe was repopulated with the precursors of present day particles and radiation. We qualitatively sketch the thermal history of the early universe in the right-hand panel of Fig. 1.6.

Besides from the simple model of a single scalar field as described above, the era of inflation can be realized within a variety of scenarios which only need to mimic a scalar condensate in slow-roll regime. For example, in k-inflation, an exponential expansion is achieved even without a potential term (Armendáriz-Picón et al. 1999; Garriga & Mukhanov 1999). In this models, the inflaton Lagrangian Eq. 1.19 gets modified to contain higher order (i.e. non-quadratic) terms,

$$\mathcal{L}_\phi \rightarrow \widehat{\mathcal{L}}_\phi = P(\phi, X)\,, \tag{1.29}$$

where P is a functional of $X \equiv g^{\mu\nu} \partial_\mu \phi \, \partial_\nu \phi$. To obtain a slow variation of the field, these models impose a limit to the inflaton "speed of sound", which
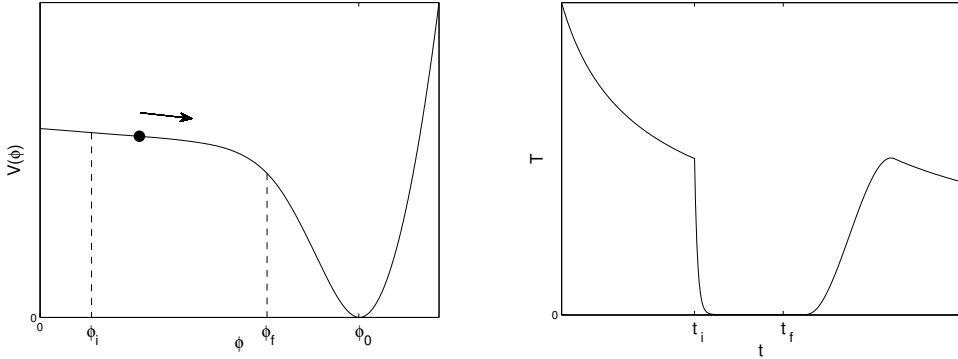
Figure 1.6: Qualitative sketch of inflation. *Left panel*: The inflaton field evolves slowly from its initial false vacuum state at ϕ_i to the minimum of the potential at ϕ_0. Inflation ends at ϕ_f, when the kinetic energy of the inflaton can no longer be neglected. *Right panel*: Prior to inflation, the temperature decreases moderately with time, $T \propto a^{-1} \propto t^{-1/2}$. With the onset of the exponential expansion at t_i, particles and radiation get rapidly diluted and the universe becomes cold and empty. After t_f, the end of inflation, reheating increases the temperature to about its original value.

differs generically from the speed of light. In another class of models, the assumption is relaxed that the inflaton field drives both the expansion of the universe and the generation of the primordial perturbation. Motivated by particle physics, in multiple field inflationary models (Linde 1990a; Copeland et al. 1994) at least one additional scalar field χ is introduced which may couple to the inflaton via a modified potential term in the Klein-Gordon equation (Eq. 1.22),

$$V'(\phi) \to \widehat{V}'(\phi, \chi) \,. \tag{1.30}$$

Likewise, by adding corrections to the Einstein-Hilbert term of the action Eq. 1.18, it is possible to realize inflation entirely within the theory of gravity (Barrow & Ottewill 1983; Starobinskiĭ 1983). With the introduction of higher order spatial curvature terms,

$$\mathcal{S} \to \widehat{\mathcal{S}} = \int d^4x \, \sqrt{-g} \left(\frac{1}{2} R + c_1 R^2 + c_2 R_{\mu\nu} R^{\mu\nu} + \dots \right) , \tag{1.31}$$

19

the equations of motions are no longer of second order only. Thereby, the gravitational field has gained extra degrees of freedom, generically including a scalar field that can imitate the role of the inflaton.

1.4   Inflation and non-Gaussianity

1.4.1   Classification scheme

The properties of the universe after the epoch of inflation are, to a large extent, independent of the details of its actual physical realization. This, on the one hand, makes inflation a robust theory with strict and well testable predictions. On the other hand, if we would like to learn more about the underlying scenario, we are forced to develop and conduct sophisticated experiments. On closer inspection, it turns out that there are three general tests inflationary models can be put to: measurements of the tilt of the primordial power spectrum, the test for relic gravitational waves, and the search for primordial non-Gaussianity.

If the inflaton was responsible for both driving the exponential expansion and generating the primordial perturbations, measurements of the spectral tilt and its scale dependence turn out to be a valuable tool to distinguish between various slow-roll models. A deviation from the Harrison-Zeldovich spectral index $n_s = 1$ has been successfully proven by WMAP data (see Table 1.1) and experiments at the sensitivity level of the Planck satellite mission will significantly constrain the functional form of the inflaton potential. However, if the assumption of a single field in slow-roll approximation is relaxed, measurements of the spectral tilt may lose their predictive power to a large extent (Bartolo et al. 2004).

During a de Sitter phase of accelerated expansion, long wavelength gravitational waves get naturally produced (e.g. Starobinskiĭ 1979; Fabbri & Pollock 1983; Abbott & Wise 1984; Sahni 1990). As their creation is unrelated to the mechanism responsible for seeding the primordial perturbations, they provide an independent test for the inflationary epoch. In particular, from the amplitude of the gravitational waves, it is possible to unravel the energy scale where inflation occurred (Lyth 1997). However, due to their extremely tiny effects on the ambient medium, the detection of primordial gravitational waves is very challenging. The fact that their amplitude is predicted to be highly suppressed in some classes of inflationary models can further exacer-

bate the situation. Besides from measuring effects of incident gravitational waves directly, a promising avenue towards a detection is to search for so called B-modes in the polarization signature of the CMB radiation. However, for the time being, it has only been possible to impose upper limits on the strength of primordial gravitational waves (see, e.g., Jenet et al. 2006; Ade et al. 2008; The LIGO Collaboration & The Virgo Collaboration 2009; Komatsu et al. 2010).

The third test for inflationary models is the search for non-Gaussian signatures in the primordial perturbations. For the simplest models of inflation, linear theory predicts them to be Gaussian (Maldacena 2003; Creminelli & Zaldarriaga 2004, see also Sect. 1.4.2). Very recently, the full second order treatment of the problem has quantified the corrections to this prediction (Beneke & Fidler 2010; Pitrou et al. 2010); the effect of non-linear mode coupling introduces small non-Gaussian phase correlations. In order to realize this lowest possible level of non-Gaussianity, four conditions have to be fulfilled (Bartolo et al. 2004):

- *Slow-roll condition.* The large friction term in the Klein-Gordon equation (Eq. 1.22) highly suppressed temporal variations of the inflaton field, $|\dot{\phi}| \ll 1$.

- *Single field model.* Both the accelerated expansion of the universe and the generation of the primordial perturbations were driven by a single scalar field.

- *Canonical kinetic term.* The kinetic term in the inflaton Lagrangian Eq. 1.19 is given by the canonical quadratic term, i.e., $T \propto g^{\mu\nu} \partial_\mu \phi \, \partial_\nu$.

- *Bunch-Davies vacuum.* The evolution of the inflaton field started out from the preferred de Sitter invariant ground state (Bunch & Davies 1978).

If at least one of the above mentioned conditions is violated, the primordial perturbations are no longer expected to be Gaussian. Conversely, a significant detection of non-Gaussianity in e.g. CMB radiation experiments has the potential to inevitably rule out all single field inflationary models (Creminelli & Zaldarriaga 2004).

Note, however, that the non-Gaussian contribution can only be a very subtle effect—current experiments constrain it to a level below about 0.1 % (Slosar et al. 2008; Komatsu et al. 2010).

A Gaussian random field is fully described by its power spectrum and no additional information can be extracted from the data set by calculating other statistical quantities. As for a Gaussian field the n-point correlation functions vanish exactly if n is odd, the lowest non-trivial order, the 3-point function, turns out to be a powerful tool to test an arbitrary field for a non-Gaussian contribution. For our particular purpose, i.e. for the analysis of CMB radiation data, it turns out to be convenient to consider the corresponding Fourier transform, the so called *bispectrum*, which we defined as

$$\langle \Phi(\vec{k}_1)\Phi(\vec{k}_2)\Phi(\vec{k}_3)\rangle = (2\pi)^3\delta^3(\vec{k}_1 + \vec{k}_2 + \vec{k}_3)F(k_1, k_2, k_3)\,. \tag{1.32}$$

Here, Φ is the gauge invariant metric perturbation as introduced by Bardeen (1980), and $F(k_1, k_2, k_3)$ defines the shape function which fully characterizes the momentum dependence of the specific bispectrum signature (Babich et al. 2004; Fergusson & Shellard 2009). Restricted to sub-horizon scales and written in longitudinal (conformal-Newtonian) gauge, the perturbations Φ coincide with the ordinary Newtonian gravitational potential up to a minus sign (Mukhanov 2005).

Dependent on the process responsible for the generation of primordial non-Gaussianity, the function $F(k_1, k_2, k_3)$ in Eq. 1.32 will take different shapes. As a result, it is possible to characterize the functional dependence of the bispectrum in terms of the contribution from different momentum vectors according to the underlying physical model responsible for generating the non-Gaussianity. For example, we obtain

$$F^{equ}(k_1, k_2, k_3) \propto \frac{(k_1 + k_2 - k_3)(k_2 + k_3 - k_1)(k_3 + k_1 - k_2)}{k_1 k_2 k_3} \tag{1.33}$$

for non-Gaussianity of equilateral type, as predicted by inflationary models with modified kinetic term in the inflaton Lagrangian (Babich et al. 2004). Here, a considerable amount of power comes from momentum configurations where $k_1 \approx k_2 \approx k_3$, i.e. from modes that were shifted outside the horizon during inflation at roughly the same time.

Non-Gaussianity of folded type is produced if we allow for variations in the vacuum ground state of the inflaton field. A deviation from Bunch-Davies vacuum may be the result of trans-Planckian effects during inflation. Although we completely lack a consistent description of the processes at the

22

highest energies, it is nevertheless possible to predict the expected contribution to the bispectrum,

$$F^{vac}(k_1, k_2, k_3) \propto \frac{1}{k_1^3 k_2^3} + \frac{1}{k_1^3 k_3^3} + \frac{1}{k_2^3 k_3^3} + \frac{3}{k_1^2 k_2^2 k_3^2} - \frac{1}{k_1 k_2^2 k_3^2} - \frac{1}{k_1 k_3^2 k_2^2}$$
$$- \frac{1}{k_2 k_1^2 k_3^2} - \frac{1}{k_2 k_3^2 k_1^2} - \frac{1}{k_3 k_1^2 k_2^2} - \frac{1}{k_3 k_2^2 k_1^2} \,. \tag{1.34}$$

Here, the most important configuration of the momenta in the shape function is approximately given by $k_h \approx k_i \approx k_j/2$ (Chen et al. 2007).

Likewise, if we violate the single field condition, we introduce non-Gaussianity of local type,

$$F^{loc}(k_1, k_2, k_3) \propto \frac{1}{k_1^3 k_2^3} + \frac{1}{k_1^3 k_3^3} + \frac{1}{k_2^3 k_3^3}$$
$$= \frac{\sum_i k_i^3}{\prod_i k_i^3} \,, \tag{1.35}$$

where most of the power stems from modes which satisfy the squeezed triangle configuration, $k_h \approx k_i \gg k_j$ (Babich et al. 2004). The shape functions of the three inflationary classes discussed are plotted in Fig. 1.7. As they are intrinsically very different, it will be possible to discern between them once a significant detection of non-Gaussianity has been made.

We will concentrate on local non-Gaussianity in the remainder of the thesis. It has been proven to be of particular importance, as a significant detection of that kind of non-Gaussianity would inevitably rule out *all* single field inflationary models (Creminelli & Zaldarriaga 2004), irrespective of other details of their realization (e.g. form of the inflaton potential, ground state, kinetic term, or slow-roll condition). The shape function Eq. 1.35 of non-Gaussianity of local type was derived from the characteristic functional form of the primordial perturbations Φ. When perturbatively expanded in the regime of weak non-Gaussianity, multi-field inflationary models predict a specific non-Gaussian signature which is localized in real space (Salopek & Bond 1990; Gangui et al. 1994),

$$\Phi(r) = \Phi_L(r) + f_{NL} \left(\Phi_L^2(r) - \langle \Phi_L^2(r) \rangle \right) \,. \tag{1.36}$$

Here, Φ_L is a Gaussian random field with power spectrum as predicted by inflation, and f_{NL} is the dimensionless measure of non-Gaussianity. Current
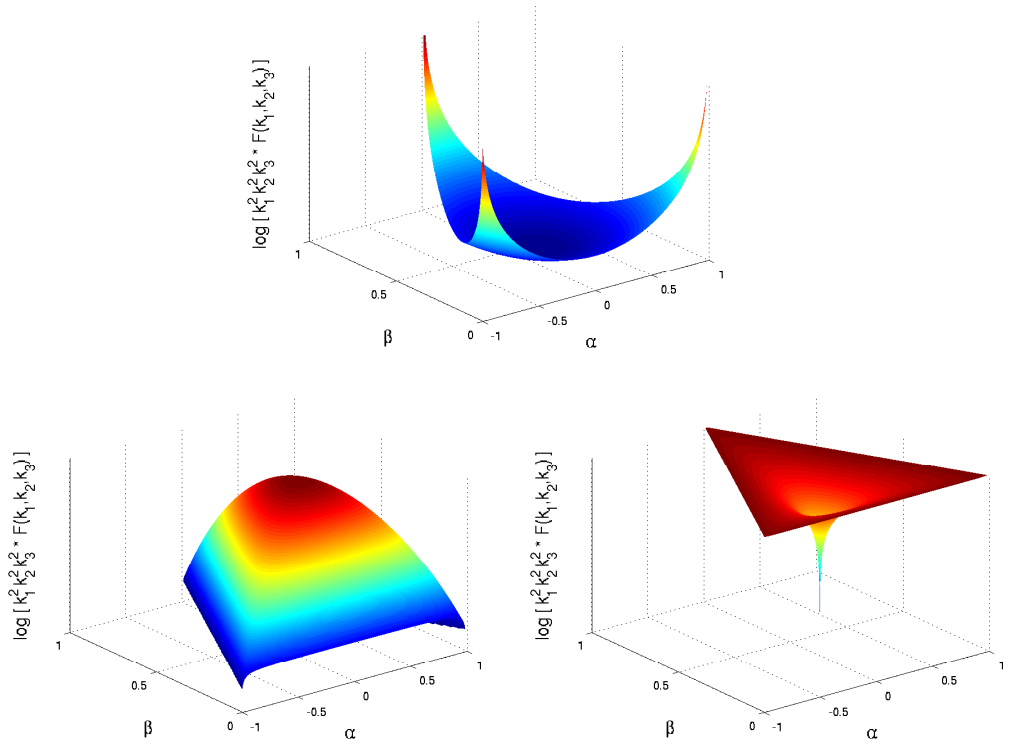
Figure 1.7: Bispectrum shape functions. We show the momentum dependent contribution to the bispectrum of local type, predicted by multi-field inflationary models (*upper panel*). For comparison, we illustrate the shape function of equilateral type, typically encountered in models which include deviations from the canonical kinetic term in the inflaton Lagrangian (*lower left panel*). Also, we plot the bispectrum signature of folded type, characteristic for models with modified inflaton vacuum state (*lower right panel*). We parametrized the momenta via $k_1 = (1 - \beta) k$, $k_2 = 1/2 (1 + \alpha + \beta) k$, and $k_3 = 1/2 (1 - \alpha + \beta) k$.

limits on the amplitude of non-Gaussianity from the WMAP 7-year data release are

$$-10 < f_{\mathrm{NL}} < 74$$

at 2-σ level (Komatsu et al. 2010). This result was derived within a frequentist approach by means of a bispectrum estimator (Komatsu et al. 2005; Smith et al. 2009). In the limit of vanishing non-Gaussianity, the estimator is optimal, i.e. it saturates the Cramer-Rao bound.

The data obtained with the Planck satellite mission will allow for a significant improvement of the error bars by almost one order of magnitude—a Fisher matrix forecast predicts a formal 1-σ error in f_{NL} of about 5 for a CMB radiation temperature only analysis which may be further improved to finally achieve a f_{NL} of 3 if polarization information is taken into account (Yadav et al. 2007).

1.4.2 Single field inflation

For simple inflationary models where only one dynamical field was present, the level of primordial non-Gaussianity from first order perturbation theory is predicted to be very small (Gangui et al. 1994; Maldacena 2003; Creminelli & Zaldarriaga 2004; Lyth 2007; Bartolo et al. 2008). To relate to this result, we follow the arguments in Creminelli & Zaldarriaga (2004) and first define the curvature perturbations[1], ζ, via the spatial components of the metric of uniform energy density slices,

$$g_{ij} \equiv a(t)^2 \mathrm{e}^{2\zeta(t,x)} h_{ij}(t,x) \,, \tag{1.37}$$

where h_{ij} encodes the tensor perturbations, but will be of no relevance for our discussion here, i.e. it is save to assume $h_{ij} = \delta_{ij}$.

Interested in the bispectrum of ζ in the squeezed limit, we set $k_1 \ll k_2, k_3$ without loss of generality and write

$$\langle \zeta(\vec{k}_1)\zeta(\vec{k}_2)\zeta(\vec{k}_3) \rangle \approx \langle \zeta(\vec{k}_1) \langle \zeta(\vec{k}_2)\zeta(\vec{k}_3) \rangle_{\zeta(\vec{k}_1)} \rangle \,, \tag{1.38}$$

where the 2-point function $\langle \zeta(\vec{k}_2)\zeta(\vec{k}_3) \rangle$ is to be evaluated for a given value $\zeta(\vec{k}_1)$.

---

[1]Note, that in the matter dominated era, the curvature perturbations can simply be rewritten in terms of the gauge invariant potential, $\Phi = \frac{3}{5}\zeta$.

In the relevant regime, i.e. when the modes k_2 and k_3 are crossing the horizon, k_1 is already far outside the horizon and therefore frozen (Salopek & Bond 1990). As a result, it is justified to consider $\zeta(\vec{k}_1) = \zeta^{\mathrm{B}}$ as a purely classical background affecting the metric Eq. 1.37 only on the largest scales.

We now consider the real space expression of $\langle \zeta(\vec{k}_2)\zeta(\vec{k}_3)\rangle_{\zeta^{\mathrm{B}}}$, and expand it to linear order for small perturbations of the background,

$$\langle \zeta(\vec{x}_2)\zeta(\vec{x}_3)\rangle_{\zeta^{\mathrm{B}}} = \langle \zeta(\vec{x}_2)\zeta(\vec{x}_3)\rangle_{\zeta^{\mathrm{B}}=0} + \zeta^{\mathrm{B}}\frac{\partial}{\partial\zeta^{\mathrm{B}}}\langle \zeta(\vec{x}_2)\zeta(\vec{x}_3)\rangle_{\zeta^{\mathrm{B}}}\big|_{\zeta^{\mathrm{B}}=0} + \mathcal{O}((\zeta^{\mathrm{B}})^2)\,.$$
(1.39)

As the wave vector k_1 is small with respect to k_2 and k_3, we first note that the background ζ^{B} is almost constant over the relevant distances $\vec{x}_2 - \vec{x}_3$. As a result, the small-scale dependency of $\langle \zeta(\vec{x}_2)\zeta(\vec{x}_3)\rangle_{\zeta^{\mathrm{B}}}$ must be attributed solely to the change of the physical distance as mediated by the metric, $\delta x_{phys} = a\,\mathrm{e}^{\zeta^{\mathrm{B}}}\delta x$. Therefore, it is possible to rewrite the derivative in Eq. 1.39,

$$\frac{\partial}{\partial\zeta^{\mathrm{B}}}\langle \zeta(x)\zeta(0)\rangle_{\zeta^{\mathrm{B}}} = x\frac{d}{dx}\langle \zeta(x)\zeta(0)\rangle_{\zeta^{\mathrm{B}}}\,.$$
(1.40)

Substituting this expression into Eq. 1.39 will lead after a Fourier transformation to the consistency relation (Maldacena 2003)

$$\lim_{\vec{k}_1\to 0}\langle \zeta(\vec{k}_1)\zeta(\vec{k}_2)\zeta(\vec{k}_3)\rangle \approx (2\pi)^3\,\delta(\vec{k}_1+\vec{k}_2+\vec{k}_3)\,(1-n_s)\,\mathcal{P}(k_1)\,\mathcal{P}(k_2)\,,$$
(1.41)

where we made use of the primordial power spectrum $\mathcal{P}(k)$ and its spectral tilt according to $1 - n_s \equiv -\frac{d\ln(k^3\mathcal{P}(k))}{d\ln k}$. As the spectral tilt is known to be small, the primordial non-Gaussianity of local type in single field inflationary models is vanishing, $f_{\mathrm{NL}} < 1$.

For the calculation presented here, no assumptions on the specific model were made, thus, the result is valid for single field inflation in general. However, in this simple approach, one relies on a strictly classical prescription of the process neglecting quantum mechanical effects. Once the calculation is repeated within a proper field theoretical framework, the above conclusion may not hold in full generality (Ganc & Komatsu 2010).

1.4.3 Generating primordial non-Gaussianity

A non-Gaussian contribution of local type to the otherwise Gaussian primordial fluctuations is generically predicted if more than one scalar field played

a crucial role in the process of generating the primordial perturbations. A simple and well studied model falling within this important class is the curvaton scenario (Mollerach 1990; Linde & Mukhanov 1997; Moroi & Takahashi 2001; Enqvist & Sloth 2002; Lyth & Wands 2002).

Here, a weakly coupled second scalar field is introduced, the curvaton χ, which has a small mass during inflation but contributes negligibly to the total energy density. Therefore, its quantum fluctuations initially sources perturbations of isocurvature (entropy) type. After the end of inflation, when the inflaton has already decayed into radiation, the temperature of the universe drops such that the curvaton field's energy density eventually contributes an important fraction to the total energy density. In this epoch, it becomes a source of curvature fluctuations. It starts to oscillate around the minimum in an approximately quadratic potential. As the curvaton obeys the equation of state of a cold, non-relativistic fluid with equation of state parameter $w = 0$, its energy density decreases as $\rho_\chi \propto a^{-3}$ and therefore more slowly than that of the radiation (scaling as $\rho_\gamma \propto a^{-4}$). In order not to dominate the total energy density at later times, the curvaton is supposed to decay well before the onset of primordial nucleosynthesis. During decay into thermalized radiation, the inhomogeneous density of the curvaton field will finally be converted into primordial adiabatic perturbations.

Besides from generating primordial perturbations after the end of inflation, another important difference to the conventional single field model is the fact that the seed fluctuations originally are of isocurvature instead of adiabatic type. As a result, the mechanism responsible for suppressing non-Gaussianity in the single field models is no longer valid. For a more quantitative description of the underlying processes in multi-field models in general, we shall review the so called δN formalism in the following (Starobinskiĭ 1985; Salopek & Bond 1990; Sasaki & Stewart 1996; Lyth et al. 2005; Lyth & Rodríguez 2005).

We start out from the definition equation of the curvature perturbation Eq. 1.37. Written in this way, ζ can be interpreted as the perturbation to the scale factor $\ln a(t)$. Allowing for a spatially inhomogeneous expansion factor, $N(t) \to N(t, x)$, we find that the curvature perturbation encodes the fluctuations in the expansion,

$$
\begin{aligned}
\zeta(t, x) &= \delta N \\
&\equiv N(t, x) - \langle N(t, x) \rangle_x \,,
\end{aligned} \tag{1.42}
$$

27

where we introduced the unperturbed median expansion rate $\langle N(t,x)\rangle_x \equiv \ln \frac{a(t)}{a(t_i)}$. As a rough estimate, one can obtain ζ from the spatial variations in the duration of the expansion,

$$
\begin{aligned}
\zeta &\approx H \, \delta t \\
&\approx H \frac{\delta\chi}{\dot{\chi}} \, ,
\end{aligned}
\tag{1.43}
$$

where χ is the relevant scalar field, e.g. the inflaton, or the curvaton. Finally, we assume that the dynamical evolution of each patch of the universe is independent of all other patches ('separate universe' assumption). With this simplification, the energy is locally conserved (Rigopoulos & Shellard 2003; Lyth et al. 2005).

Given an arbitrary number of light scalar fields with small Gaussian fluctuations, $\chi_i(x) = \bar{\chi}_i + \delta\chi_i(x)$, we derive an approximate expression for the small inhomogeneities in the expansion factor,

$$
\delta N \approx N_{,i}\delta\chi_i + 1/2 N_{,ij}\delta\chi_i\delta\chi_j + \mathcal{O}(\delta\chi^3)\,,
\tag{1.44}
$$

where we defined the partial derivative of N via $N_{,i} \equiv \frac{\partial N}{\partial \chi_i}$, and sum over all repeated indices. We identify the nearly flat power spectrum of the scalar field perturbations (Bunch & Davies 1978),

$$
\langle \delta\chi(k_1)\delta\chi^*(k_2)\rangle = (2\pi)^3 \frac{H_{\looparrowright}^2}{2k_1^3}\,\delta(k_1 - k_2)\,,
\tag{1.45}
$$

where we used the Hubble parameter at horizon exit of the corresponding modes, $H_{\looparrowright}$. Combining Eq. 1.42 and Eq. 1.44, we conclude for the curvature perturbation power spectrum at first order (Sasaki & Stewart 1996)

$$
\langle \zeta(k_1)\zeta^*(k_2)\rangle = (2\pi)^5 \frac{\mathcal{P}_\zeta}{2k_1^3}\,\delta(k_1 - k_2)\,,
\tag{1.46}
$$

where

$$
\mathcal{P}_\zeta = \left(\frac{H_{\looparrowright}}{2\pi}\right)^2 \sum_i N_{,i}^2\,.
\tag{1.47}
$$

In analogy to Eq. 1.36, we introduce the level of non-Gaussianity, f_{NL}, as overall prefactor to a non-linear transform of the curvature perturbations,

$$
\begin{aligned}
\zeta(r) &= \zeta_{\mathrm{L}}(r) + \frac{3}{5}\,f_{\mathrm{NL}}\left(\zeta_{\mathrm{L}}^2(r) - \langle \zeta_{\mathrm{L}}^2(r)\rangle\right) \\
&\equiv \zeta_{\mathrm{L}}(r) + \frac{3}{5}\,f_{\mathrm{NL}}\,\zeta_{\mathrm{NL}}(r)\,.
\end{aligned}
\tag{1.48}
$$

Interested in the corresponding expression in momentum space, we rephrase the non-Gaussian term as

$$\zeta_{NL}(k) = \int \frac{d^3p}{(2\pi)^3} \zeta_{\rm L}(k+p)\zeta_{\rm L}^*(p) - (2\pi)^3\sigma^2\delta^3(k)\,, \qquad (1.49)$$

where the second term subtracts the variance σ^2 of the field to ensure $\langle\zeta_{NL}\rangle = 0$. Now, we identify an important non-vanishing contribution to the bispectrum (Komatsu & Spergel 2001),

$$\langle\zeta(k_1)\zeta(k_2)\zeta(k_3)\rangle \supseteq \langle\zeta_{\rm L}(k_1)\zeta_{\rm L}(k_2)\zeta_{\rm NL}(k_3)\rangle + 2\,{\rm cycl.}$$
$$= \frac{6}{5}f_{\rm NL}(2\pi)^3\left[P(k_1)P(k_2) + 2\,{\rm cycl.}\right]\,. \qquad (1.50)$$

On the other hand, we use Eq. 1.44 to expand the expression to fourth order in $\delta\chi$,

$$\langle\zeta(k_1)\zeta(k_2)\zeta(k_3)\rangle = N_{,i}N_{,j}N_{,h}\langle\delta\chi_i(k_1)\delta\chi_j(k_2)\delta\chi_h(k_3)\rangle$$
$$+ N_{,i}N_{,j}N_{,hk}\left[\langle\delta\chi_i(k_1)\delta\chi_j(k_2)\delta\chi_h(k_3)\delta\chi_k(k_3)\rangle + 2\,{\rm cycl.}\right]$$
$$+ \mathcal{O}(\delta\chi^4)\,. \qquad (1.51)$$

The first term on the right hand side vanishes as it contains the expectation value of an odd number of independent Gaussian variables. For an explicit expression of the amplitude of non-Gaussianity, we finally obtain (Lyth & Rodríguez 2005; Byrnes et al. 2006; Sasaki et al. 2006)

$$f_{\rm NL} = \frac{5}{6}\frac{\sum_{ij}N_{,ij}N_{,i}N_{,j}}{(\sum_i N_{,i}^2)^2}\,, \qquad (1.52)$$

where we have used Eq. 1.45 and Eq. 1.47 to rewrite $H_{\not\!\!P}$ in terms of derivatives of N.

An application of this formula to the curvaton scenario as discussed above allows us to predict the range of non-Gaussianity expected in this model. Considering perturbations in the curvaton field around a mean value $\bar\chi$, $\chi = \bar\chi + \delta\chi$, we find for the contribution to the energy density in a quadratic potential (Tseliakhovich et al. 2010)

$$\bar\rho_\chi \propto \langle\chi^2\rangle$$
$$= \bar\chi^2 + \langle\delta\chi^2\rangle\,,\ {\rm hence}$$
$$\frac{\delta\rho_\chi}{\bar\rho_\chi} \approx \frac{2\delta\chi}{\bar\chi} + \frac{\delta\chi^2 - \langle\delta\chi^2\rangle}{\bar\chi^2}\,. \qquad (1.53)$$

Obviously, the above equation resembles the definition equation of local non-Gaussianity, Eq. 1.36. Any non-Gaussian signature in $\delta\rho_\chi$ will finally be imprinted onto the CMB radiation.

We now define N as expansion factor from the onset of the oscillations of the curvaton field after the end of inflation until its decay. We introduce the ratio of the curvaton energy density compared to the total energy density at decay time t_f,

$$r = \frac{\rho_f^\chi}{\rho_f}. \tag{1.54}$$

In the following, we focus on the most relevant case, the limit of a radiation dominated universe, $r < 1$.

For a slice of uniform total energy density, the perturbation of the expansion factor is given by

$$\delta N = r\frac{\delta\rho_f^\chi}{4\rho_f^\chi}, \text{ thus} \tag{1.55}$$

$$N = r\frac{\ln(\rho_f^\chi)}{4} + \mathcal{C}_1, \tag{1.56}$$

where we introduced an arbitrary constant of integration. We now make use of the fact that the curvaton energy density perturbation remains constant during the period considered here, and rewrite it as a function of the amplitude of the curvaton field when the oscillation started, χ_i,

$$\begin{aligned}
N &= r\frac{\ln(1/2 m_\chi^2 \chi_i^2)}{4} + \mathcal{C}_1 \\
&= r\frac{\ln(\chi_i)}{2} + \mathcal{C}_2, \tag{1.57}
\end{aligned}$$

where we have used a quadratic approximation for the potential $V(\chi)$, and the particle mass m_χ. Finally, we apply Eq. 1.52 to predict the level of non-Gaussianity of local type in the curvaton scenario,

$$\begin{aligned}
f_{\text{NL}} &= \frac{5}{6}\frac{N_{,\chi\chi}}{(N_{,\chi})^2} \\
&= -\frac{3}{5r}. \tag{1.58}
\end{aligned}$$

Hence, the curvaton scenario generically predicts a negative value of f_{NL} and the free parameter r is already highly constrained by the latest observational

bounds (Komatsu et al. 2010). The analysis can be extended to the case of two or more curvaton fields (Assadullahi et al. 2007; Choi & Gong 2007), or to include higher order terms in the curvaton potential, leading to a non-linear dynamical evolution prior to the decay (Enqvist & Nurmi 2005; Huang 2008). As a result, the predicted value of f_{NL} can also become large and positive (Enqvist et al. 2010).

We now review another class of early universe scenarios predicting a significant level of local non-Gaussianity. The ekpyrotic and cyclic universe models were recently introduced to apply concepts adopted from string theory within a cosmological framework (Gordon et al. 2001; Khoury et al. 2001, 2002; Notari & Riotto 2002; Steinhardt & Turok 2002a,b). Although not yet fully understood and still plagued by very serious problems (see, e.g., Kallosh et al. 2001; Lyth 2002; Kallosh et al. 2008; Linde et al. 2010, especially violating the null energy condition turns out to be problematic), these models may offer a way to overcome some shortfallings of inflation. Here, the period of inflation gets completely replaced by a phase of slow contraction postulated to take place prior to the big bang. It can be shown that during such an epoch, almost scale-invariant scalar perturbations in a flattened region of space can be generated, resolving the problems of standard cosmology (Erickson et al. 2007). In addition to the absence of gravitational waves, a significant level of local non-Gaussianity is predicted, both potentially observational signatures that in principle would allow to distinguish ekpyrotic models from the simplest inflationary scenarios.

To realize an ekpyrotic epoch of contraction, we first note that from Eq. 1.9 we can derive the general functional dependence of the energy density of a particle species on the scale factor,

$$\rho \propto a^{-3(1+w)} \, . \tag{1.59}$$

In the pre-bounce contracting phase, the existence of a component with a very large equation of state parameter $w \gg 1$ is postulated. Once the scale factor decreases, it will finally dominate over matter ($\rho_m \propto a^{-3}$) and radiation ($\rho_\gamma \propto a^{-4}$). As a result, the relative energy density of radiation and its perturbations will decrease until it eventually becomes a negligible fraction of the total energy density; the space becomes flat.

It is possible to introduce this new kind of matter with $w \gg 1$ by means of scalar fields. For the primordial perturbations to gather a nearly scale invariant spectrum in agreement with observations, more than one of such fields

is necessary (Koyama & Wands 2007; Koyama et al. 2007b). For simplicity, however, we will restrict the discussion to single field ekpyrotic models in the following.

For the self-interaction of the scalar field, a steep, negative potential is required in ekpyrotic scenarios, e.g. of the form (Buchbinder et al. 2007; Lehners et al. 2007)

$$V(\chi) = -V_0 \, \mathrm{e}^{-C\chi} \,, \tag{1.60}$$

where C is a positive constant. This is a simple parametrization of the potential encountered in heterotic M-theory (Hořava & Witten 1996; Witten 1996; Lukas et al. 1999b,a). The original version of ekpyrotic models proposed an effective 5-dimensional Universe consisting of two bounding (3+1)-dimensional branes separated through a finite bulk volume. The visible of the two branes corresponds to the usual four-dimensional universe we live in, whereas the hidden brane remains inaccessible (Khoury et al. 2001). Then, the potential Eq. 1.60 induces a force acting along the fifth dimension with a certain probability to make the branes collide. Such an approach, collision, and subsequent phase of recession corresponds to a full cycle in the evolution of the universe with collapse, bounce, and expansion. Here, we will assume a regular bounce during which the curvature perturbations on super-horizon scales remain unaffected. As a result, the entropy perturbations generated during the ekpyrotic phase can be directly mapped to the adiabatic perturbations after the bounce.

Following Koyama et al. (2007a); Creminelli & Senatore (2007); Lehners (2010), to quantify the non-Gaussian contribution expected in ekpyrotic models, we neglect the effect of gravity. We consider small perturbations of the scalar field χ around its mean value, $\chi(x,t) = \bar{\chi}(t) + \delta\chi(x,t)$, and start out with the evolution equation of the unperturbed spatially invariant field,

$$\ddot{\chi}(t) + V_{,\chi}(\chi(t)) = 0 \,, \tag{1.61}$$

and constrain the functional form of the potential by requiring a scale invariant power spectrum of the field perturbations. For the Fourier modes of the fluctuations, the equation of motion takes the form of a wave equation (Creminelli & Senatore 2007),

$$\ddot{\delta\chi} + \left[k^2 + V_{,\chi\chi}(\chi) \right] \delta\chi = 0 \,. \tag{1.62}$$

In the regime $V_{,\chi\chi} < -k^2 < 0$, the solution to Eq. 1.62 stops oscillating and freezes out. As a result, a functional dependence of $V_{,\chi\chi} \propto t^{-2}$ is required to

obtain a power law solution in this region of parameter space. Adopting this form, one finds the asymptotic behavior of the field perturbations,

$$\delta\chi(k,t) \propto k^{-1/2} f(kt) \,, \tag{1.63}$$

where the function $f(kt)$ describes the oscillatory behavior of the perturbations. To maintain a scale invariant solution after freeze-out, we enforce $\delta\chi(k,t) \propto t^{-1}$ and eventually obtain the explicit expression for the second derivative of the potential

$$V_{,\chi\chi} = -\frac{2}{t^2} \,. \tag{1.64}$$

Finally, we find the normalized solution to Eq. 1.62,

$$\delta\chi(k,t) = \frac{1}{\sqrt{2k}} \left(1 - \frac{i}{kt} \right) e^{-ikt} \,. \tag{1.65}$$

To derive an explicit expression for the potential, we calculate the time derivative of Eq. 1.61,

$$\dddot{\chi} - \frac{2}{t^2}\dot{\chi} = 0 \,, \tag{1.66}$$

with power law solution $\dot{\chi}(t) = -2M/t$, where we introduced a constant of integration M and neglected the decaying term $\propto t^2$. Integration yields to the expression

$$\chi(t) = -2M \log(-t) + \mathcal{C} \,, \tag{1.67}$$

which we use to replace the time variable in the equation for the potential $V_{,\chi\chi} = -2/t^2$ in favor of χ to finally obtain

$$V(\chi) = -V_0\, e^{\chi/M} \,, \tag{1.68}$$

resembling the suggested functional form of the potential in Eq. 1.60.

To calculate the level of non-Gaussianity in ekpyrotic models, we adopt the procedure of Maldacena (2003) and write the leading order component in the bispectrum by means of the interaction Hamiltonian,

$$\langle\delta\chi(k_1)\delta\chi(k_2)\delta\chi(k_3)\rangle = -i\int_{-\infty}^{t} \langle\delta\chi(k_1)\delta\chi(k_2)\delta\chi(k_3)H_{int}(t')\rangle dt' + \text{c.c.} \,, \tag{1.69}$$

33

The cubic self-interaction is described by

$$H_{int}(t) = \frac{V_{,\chi\chi\chi}}{3!}\delta\chi^3$$
$$= -\frac{2}{t^2}\frac{\delta\chi^3}{3!M} \, , \qquad (1.70)$$

where we made use of Eq. 1.68. Substituting Eq. 1.65, it is possible to identify the leading order term in the bispectrum for small t (Creminelli & Senatore 2007),

$$\langle\delta\chi(k_1)\delta\chi(k_2)\delta\chi(k_3)\rangle = (2\pi)^3\delta(k_1 + k_2 + k_3)\frac{\sum_i k_i}{\prod_i k_i}\frac{1}{8Mt^4} \, . \qquad (1.71)$$

The characteristic momentum dependence found here unravels a non-Gaussian contribution of local type (cf. Eq. 1.35).

The free choice of the parameter M results in a model dependent non-Gaussian contribution. However, in reasonable scenarios, the expected range of non-Gaussianity lies around $-50 \lesssim f_{\rm NL} \lesssim 60$ (Lehners & Renaux-Petel 2009)—it is significantly wider than for single field inflationary models.

1.4.4   Secondary sources of non-Gaussianity

Due to a tight coupling between the primordial plasma and photons, non-Gaussianity in the perturbations will leave an imprint onto the CMB radiation, opening up the opportunity to construct dedicated tests searching for this signature. However, as various physical mechanisms are capable of modifying the pristine fluctuations in the CMB radiation on their way from recombination at redshift $z \approx 1100$ to the detectors at present time (Aghanim et al. 2008), secondary non-Gaussianity of non-primordial origin will be induced. As it is imperative to quantify the expected amount of contamination, these effects have been subject to extensive studies in literature (e.g. by Goldberg & Spergel 1999; Spergel & Goldberg 1999; Verde & Spergel 2002; Castro 2003; Serra & Cooray 2008; Hanson et al. 2009; Khatri & Wandelt 2009; Pitrou 2009).

The most important among all possible contributions to non-primordial non-Gaussianity stems from the correlation between the non-linear integrated Sachs-Wolfe effect[2] (ISW, Sachs & Wolfe 1967) and weak gravitational lensing. The ISW effect, originating from the time evolution of the gravitational

---

[2]That is, the linear ISW plus the Rees-Sciama effect, Rees & Sciama 1968

potential during photon crossing, affects the CMB radiation pattern on large scales. Contrary, lensing induced by galaxy clusters (themselves residing in potential wells), modifies the fluctuations on small scales. The correlation between these two effects will, therefore, peak for squeezed triangle momentum configurations, mimicking the shape function of non-Gaussianity of local type. While for WMAP data this mechanism should lead to only a small bias $\Delta f_{\mathrm{NL}} \approx 3$ (Komatsu et al. 2010) which has not been detected directly (Munshi et al. 2009), for the analysis of Planck satellite data the effect will play an important role and may lead to a contribution of up to $\Delta f_{\mathrm{NL}} \approx 10$ (Mangilli & Verde 2009).

Beyond, radiation from residual point sources has been discussed as possible secondary source of non-Gaussianity. They are either radio sources, luminous infrared galaxies, or galaxy clusters inducing spectral distortions due to Compton upscattering of CMB photons via the Sunyaev-Zeldovich effect (Sunyaev & Zeldovich 1970). To reasonable approximation, they have a constant bispectrum amplitude which is independent of the multipole moments considered, though their contribution varies in different frequency bands (Komatsu et al. 2003). To reduce the effect of radio sources, a point-source mask is usually imposed to the data prior to the analysis, constructed either from the CMB radiation maps themselves, or with the help of dedicated radio surveys as e.g. the GB6 (Gregory et al. 1996), or the PMN surveys (Griffith & Wright 1993). However, as sources can only be detected and removed down to an experiment-specific flux limit, a residual contribution will remain in the data. Recently, an estimate of the contribution of point sources to local non-Gaussianity has been quantitatively specified. The correction is most important at low frequencies but will probably not exceed $\Delta f_{\mathrm{NL}} \lesssim 1$ for Planck data (Babich & Pierpaoli 2008).

Another large contribution to the radiation in the GHz regime is generated within our Galaxy (Bennett et al. 2003b; Gold et al. 2009). A relevant physical process of particular importance at low frequencies is synchrotron emission from relativistic electrons interacting with the Galactic magnetic field. Similar in spectral shape and therefore also important at low frequencies is free-free radiation generated by electrons scattering off charged particles. A third component whose contribution is becoming dominant towards higher frequencies is sourced by emission from thermal dust. To correct for this class of secondary sources, foreground templates describing the spatial pattern of the emission are marginalized over in the analysis (Smith et al. 2009). They were constructed from a 408 MHz full sky survey (synchrotron

template, Haslam et al. 1981), Hα line emission maps (free-free template, Finkbeiner 2003), and infrared emission data (dust template, Finkbeiner et al. 1999). To constrain the foreground emission at the frequencies of the CMB radiation experiment, the templates have to be extrapolated assuming a specific spectral index for the component. A comparison between the deduced f_{NL} values from raw and cleaned WMAP 7-year data indicates that the smooth components amount for a non-Gaussian signal of about $\Delta f_{NL} \approx 10$ when a conservative sky mask is imposed (Komatsu et al. 2010). However, the residuals after template marginalization are probably negligible (Smith et al. 2009).

The issue of a different kind of non-Gaussianity, primary non-Gaussianity, has recently been comprehensively addressed in Pitrou et al. (2010) (see also Beneke & Fidler 2010). It specifies the contribution from phase correlations arising due to non-linear processes between the end of inflation and recombination. To quantify this contribution, the full second order Boltzmann equation was solved, including all components of the cosmic fluid. It was found that these effects will induce excess non-Gaussianity at a level of about $\Delta f_{NL} \simeq 5$.

1.5 Bayesian statistics

In this thesis, we pursue the goal to develop a *Bayesian* method to search for non-Gaussianity in CMB radiation data. Unfortunately, using Bayesian statistics is still a less common alternative to the currently predominant *frequentist* approach—we therefore briefly outline its foundations in what follows (for a more comprehensive discussion, see the textbooks of, e.g., Leonard & Hsu 2001; Gill 2002; MacKay 2005; Bolstad 2007; Hobson et al. 2010).

The frequentist approach is characterized by basic ideas that can be summarized as follows:

- Probabilities are defined as relative frequencies in infinite repetitions of random experiments.

- The parameters that characterize a population are fully determined yet unknown constants.

- The quality of statistical methods is assessed by how well they perform given an infinite number of repetitions of the experiment.

In the frequentist approach, it is only possible to quantify the probability of random variables. But as physical parameters like e.g. the speed of light, Newton's constant, or the level of primordial non-Gaussianity are fixed, probability statements about their numerical values cannot be made. To circumvent this problem, a sampling distribution is constructed, the probability distribution of a given statistic obtained from random samples drawn from the population. Finally, a confidence interval of the parameter is deduced from the width of that distribution.

An intrinsic shortcoming of this procedure is the ambiguity in the definition of estimators, i.e. the statistics used to measure the parameter of interest. For a given problem, several of them can usually be constructed. In general, their outcome will be different, necessitating the development of sophisticated methods to judge over performance and reliability of estimators. Another objection concerns the generation of the sampling distribution. As it involves random realizations drawn from the population that actually have not been observed in the experiment, information other than that carried in the data become relevant.

Bayesian statistics, on the contrary, is based on an extended interpretation of probability. Here, it is used in a more general way, to measure a *degree of belief* in a certain proposition. On the basis of three axioms, it is possible to map the degree of belief onto a probability (Cox 1946). Denoting the degree of belief in proposition a by $D(a)$, we define the degree of belief in a conditional proposition a given a second proposition b to be true by $D(a|b)$. Then, the axioms are:

- *Ordering:* If $D(a) \leq D(b)$ and $D(b) \leq D(c)$, then $D(a) \leq D(c)$, where "$\leq$" is a suitable order operator.

- *Negation:* There exists a relation f between the degree of belief in a proposition a and its negation $\bar{a}$ such that $D(a) = f[D(\bar{a})]$.

- *Conjunction:* A conjunction of propositions a and b can be expressed via a function g such that $D(a, b) = g[D(a|b), D(b)]$, where $D(a|b)$ is the conditional degree of belief as defined above.

If the axioms are fulfilled, the degrees of belief can be mapped onto usual probabilities with the well-known properties, $P(\text{false}) = 0$, $P(\text{true}) = 1$, $0 \leq P(a) \leq 1$, and comply with the relations $P(a) = 1 - P(\bar{a})$, $P(a, b) = P(a|b) P(b)$.

With this redefinition, we can apply the concept of probability to a much broader class of problems from the outset. For example, although the Hubble constant is not a random variable, we may ask the question: "What is the probability to find its current value within the range $69\,km\,s^{-1}\,Mpc^{-1} \leq H_0 \leq 71\,km\,s^{-1}\,Mpc^{-1}$?" It is important to note that we are forced to provide limits like that to H_0 because our knowledge about its true value is incomplete, not because it is the outcome of a random experiment with a given probability distribution.

The cornerstone of Bayesian statistics is the theorem of Bayes that allows to specify how the knowledge about a parameter of interest λ should be updated after new data D were taken into account (Bayes & Price 1763). It formally results from symmetry considerations of the joint distribution of two events; from

$$P(\lambda, D) = P(\lambda|D)P(D)\,, \text{ and}$$
$$P(\lambda, D) = P(D, \lambda)$$
$$= P(D|\lambda)P(\lambda)\,, \text{ we follow}$$
$$P(\lambda|D) = \frac{P(D|\lambda)P(\lambda)}{P(D)}\,. \tag{1.72}$$

In the above expression, $P(\lambda)$ is the *prior distribution*, representing our knowledge about λ before the data were taken into account, $P(D|\lambda)$ is the so called *likelihood function* of the parameter, and the normalization constant $P(D)$ is the *evidence*. Together, they build up the *posterior distribution*, $P(\lambda|D)$, which mirrors our updated knowledge about the parameter after the data have been analyzed.

Let us now summarize the main characteristics of the Bayesian approach to statistics:

- The parameters we want to constrain are put on the same level with random variables.

- We use the degree of belief to interpret probability statements about parameters.

- Inference about parameters is made by directly applying the rules of probability calculus.

- To update our knowledge about parameters when new data arrive, we make use of Bayes' theorem (Eq. 1.72).

38

Contrary to the frequentist approach, the Bayesian concept offers a consistent and unambiguous way to update our (subjective) prior knowledge about a parameter when new data become available. That is, an independent analysis that makes use of the same data and prior distribution will lead to identical results. Furthermore, only information from the data that have actually been observed enter the analysis, obviating the necessity to construct sampling distributions from possible (but unrealized) outcomes of the experiment.

For illustrative purposes, we include a brief discussion of a simple example (based on MacKay 2005) to compare the two schools of statistics against each other. Let us assume that a coin have been tossed $N = 250$ times and a sequence of $n_h = 141$ heads was observed. Now, we want to contrast the hypothesis $\mathcal{H}_0$ "the coin is fair" with hypothesis $\mathcal{H}_1$ "the coin is biased" in a quantitative way.

In the frequentist analysis, which we discuss first, one completely concentrates on the null hypothesis. We expect the number of heads to follow a binomial distribution

$$P(n_h|N, p) = \binom{N}{n_h} p^{n_h}(1 - p)^{N - n_h} , \qquad (1.73)$$

where $p \equiv 1/2$ for a fair coin as stated in $\mathcal{H}_0$. Then, we specify the probability to find an as extreme value for n_h as observed in the data,

$$\begin{aligned} P(n_h = 141) &= 2 \sum_{n=141}^{250} \binom{250}{n} 1/2^{250} \\ &= 0.0497 , \end{aligned} \qquad (1.74)$$

i.e. in the frequentist analysis, we reject the null hypothesis at a significance level of 5 %. As a result, we conclude that the coin is biased at a confidence level of 95 %.

We will now focus on the Bayesian analysis. In the language of Bayesian statistics, we have to perform a model comparison between model $\mathcal{H}_0$ (the coin is fair) and model $\mathcal{H}_1$ (the coin is biased) given the data. To this end, we define the probabilities of (that is, our degree of belief in) $\mathcal{H}_0$,

$$P(\mathcal{H}_0|n_h) = \frac{P(n_h|\mathcal{H}_0)P(\mathcal{H}_0)}{P(n_h)} , \qquad (1.75)$$

and $\mathcal{H}_1$,

$$P(\mathcal{H}_1|n_h) = \frac{P(n_h|\mathcal{H}_1)P(\mathcal{H}_1)}{P(n_h)}\,, \tag{1.76}$$

using Bayes' theorem. For the analysis, we further have to specify the subjective prior distribution of p which we choose to be flat, $P(p|\mathcal{H}_1) = 1$. Not preferring any of the two hypotheses a priori (i.e. $P(\mathcal{H}_0) \equiv P(\mathcal{H}_1) = 1/2$), we construct the so called Bayes factor, the likelihood ratio of the hypotheses,

$$\begin{aligned}
\frac{P(n_h|\mathcal{H}_1)}{P(n_h|\mathcal{H}_0)} &= \frac{\int_0^1 dp\, p^{n_h}(1-p)^{N-n_h}P(p|\mathcal{H}_1)}{(1/2)^{n_h}(1-1/2)^{N-n_h}} \\
&= \frac{\frac{141!109!}{251!}}{(1/2)^{250}} \\
&= 0.61\,. \tag{1.77}
\end{aligned}$$

In fact, the Bayesian analysis reveals that hypothesis $\mathcal{H}_0$ is actually slightly *preferred* over hypothesis $\mathcal{H}_1$, i.e. for the choice of the prior as stated above, we conclude that the coin is fair. Note, however, that a Bayes factor close to one signalize indecisive data. The result will therefore be relatively sensitive to the prior distribution $P(p|\mathcal{H}_1)$. But even for an overidealized choice of the prior—an a posteriori constructed delta function exactly matching the relative frequency of heads in the data, $P(p|\mathcal{H}'_1) = \delta(p-141/250)$—we obtain a Bayes factor of

$$\begin{aligned}
\frac{P(n_h|\mathcal{H}'_1)}{P(n_h|\mathcal{H}_0)} &= \frac{p^{141}(1-p)^{109}\big|_{p=\frac{141}{250}}}{(1/2)^{250}} \\
&= 7.8\,, \tag{1.78}
\end{aligned}$$

indicating only moderate evidence in favor of $\mathcal{H}'_1$.

This example illustrates the basic concepts and advantages of Bayesian statistics. Directly applying the rules of probability theory to a degree of belief provides the framework for a powerful and consistent analysis. Instead of specifying the probability to find an as extreme outcome as in the data given the null hypothesis to be correct and assuming an infinite repetition of the experiment (as it is done in the frequentist approach), the Bayesian method allows us to directly address the relevant question, namely which of the two competing models is actually preferred by the data.

1.6   Outline of the thesis

The objective of this thesis is to search for primordial non-Gaussianity of local type in CMB radiation data using Bayesian statistics. To this end, we first develop an improved algorithm to simulate CMB radiation temperature and polarization maps containing an arbitrary level of primordial non-Gaussianity of local type in Chap. 2. We formulate an optimization scheme that allows us to control the simulation accuracy and speed up the calculation by about one order of magnitude. Then, we introduce the Bayesian approach to infer the level of non-Gaussianity from a data set and demonstrate the principal aspects on the basis of a simplified toy model (Chap. 3). Also, we contrast an exact treatment of the problem with an approximate yet computationally more efficient implementation. As a next step, we provide a detailed comparison to the conventional frequentist approach in Chap. 4. Against the background of realistic CMB radiation temperature maps, we examine the performance of the competing methods. We summarize our results in Chap. 5. In App. A, we provide supplementary information to the simulation algorithm, and we finally discuss the extension of the analysis scheme to constrain higher order non-Gaussian terms in App. B.

Chapter 2

Improved simulation of non-Gaussian temperature and polarization CMB maps

Franz Elsner[1], and Benjamin D. Wandelt[2,3,4]

[1]Max-Planck-Institut für Astrophysik, Karl-Schwarzschild-Straße 1, 85748 Garching, Germany

[2]Department of Physics, University of Illinois at Urbana-Champaign, 1110 W. Green Street, Urbana, IL 61801, USA

[3]Department of Astronomy, University of Illinois at Urbana-Champaign, 1002 W. Green Street, Urbana, IL 61801, USA

[4]California Institute of Technology, MC 130-33, Pasadena, CA 91125, USA

Abstract

We describe an algorithm to generate temperature and polarization maps of the cosmic microwave background radiation containing non–Gaussianity of arbitrary local type. We apply an optimized quadrature scheme that allows us to predict and control integration accuracy, speed up the calculations, and reduce memory consumption by an order of magnitude. We generate 1000 non–Gaussian CMB temperature and polarization maps up to a multipole moment of $\ell_{max} = 1024$. We validate the method and code using the power spectrum and the fast cubic (bispectrum) estimator and find consistent results. The simulations are provided to the community[1].

---

[1] Available at `http://planck.mpa-garching.mpg.de/cmb/fnl-simulations`

2.1 Introduction

The simplest models of inflation predict almost perfectly Gaussian primordial fluctuations, generated by a single scalar quantum field in ground state (Guth 1981; Bardeen et al. 1983; Mukhanov et al. 1992), but a large number of alternative scenarios can easily be constructed. To test competing inflationary models, measurements of statistical properties of the cosmic microwave background (CMB) radiation have turned out to be of particular importance. Combined with constraints on the scalar spectral index n_s and the search for gravitational waves imprinted on the polarization signature, the test for non-Gaussianity is a fundamental means to probe the physical processes of inflation.

Among all inflationary models predicting significant levels of non-Gaussianity, two broad classes can be distinguished. Non–Gaussianity of *equilateral* type is realized primarily in models with non–minimal Lagrangian including higher order derivatives (Alishahiha et al. 2004; Senatore 2005; Chen 2005; Langlois et al. 2008). Non–Gaussianity of *local* type is achieved to very good approximation in multi–field inflation (Moroi & Takahashi 2001; Enqvist & Sloth 2002; Lyth et al. 2003), or in cyclic/ekpyrotic universe models (Khoury et al. 2001; Steinhardt & Turok 2002; Lehners & Steinhardt 2008).

Concentrating on *local* non-Gaussianity, we parameterize the primordial curvature perturbations, Φ, by introducing an additional quadratic dependence on a purely Gaussian auxiliary field Φ_L, that is local in real space, of the form (Verde et al. 2000; Komatsu & Spergel 2001)

$$\Phi(r) = \Phi_\mathrm{L}(r) + f_\mathrm{NL}\,\Phi_\mathrm{NL}(r)\,, \tag{2.1}$$

where $\Phi_\mathrm{NL}(r)$ is defined as

$$\Phi_\mathrm{NL}(r) = \Phi_\mathrm{L}^2(r) - \langle \Phi_\mathrm{L}^2(r) \rangle\,, \tag{2.2}$$

and f_NL is the dimensionless measure of the amplitude of non-Gaussianity. Primordial non-Gaussianity in the curvature perturbations Φ will be encoded in the CMB signal.

Simulations of maps containing non-Gaussianity of local type have been extensively used in the context of WMAP data analysis. They play a crucial role in probing the sensitivity of analysis tools and provide the opportunity to quantitatively estimate the contribution of secondary anisotropies or instrumental effects to the measured level of non-Gaussianity in experimental

data. With the advent of Planck, probing the non-Gaussian contribution within the CMB radiation even more accurately, the requirements for high resolution, high accuracy simulations of non-Gaussian CMB temperature and polarization maps will further increase.

To meet the demand for simulated non-Gaussian maps, several different approaches have been taken. First simulations of temperature maps with primordial non-Gaussianity of local type have generated the underlying primordial perturbation in Fourier space (Komatsu et al. 2003). This approach is computationally very demanding while it is difficult to preserve numerical accuracy. A different method has been proposed in Liguori et al. (2003, 2007), where the authors work with 'filter' functions to introduce the proper spatial correlations of the primordial potential. Recently, a fast, specifically tailored algorithm for the weakly non-Gaussian regime has been introduced by Smith & Zaldarriaga (2006), that focuses on simulating maps with a given three–point function. While it is not restricted to non-Gaussianity of local type, higher order correlations are not guaranteed to match the model.

The algorithm presented here was closely inspired by the work of Liguori et al. (2003). We focus on an enhancement of their algorithm in view of its numerical efficiency. Our idea is to precompute quadrature nodes and weights; this is similar in spirit to Smith & Zaldarriaga (2006), but aims at assuring accurately simulated maps to all correlation orders, rather than focusing exclusively on the three–point function.

This paper is organized as follows. In Sect. 2.2, we present a new approach to simulate non-Gaussian temperature and polarization maps. An optimization scheme is provided in Sect. 2.3 that allows for an increase in computational efficiency. We then apply the fast estimator to simulated CMB maps to check our results for consistency (Sect. 2.4). Finally, we summarize our findings in Sect. 2.5.

Throughout the paper we assume the following $WMAP5+BAO+SN$ cosmological parameters[2]: $\Omega_\Lambda = 0.721$, $\Omega_c h^2 = 0.1143$, $\Omega_b h^2 = 0.02256$, $\Delta_{\mathcal{R}}^2(0.002\ Mpc^{-1}) = 2.457 \cdot 10^{-9}$, $h = 0.701$, $n_s = 0.96$, and $\tau = 0.084$.

2.2   Simulation of non–Gaussian CMB maps

We describe a new, direct method to simulate non-Gaussian CMB temperature and polarization maps below. Our objective is to generate a set of linear

---

[2]Obtained from `http://lambda.gsfc.nasa.gov/product/map/dr3/parameters.cfm`

and non–linear spherical harmonic coefficients that are valid realizations of temperature and polarization fluctuations, $\{a_{\text{L }\ell m},\ a_{\text{NL }\ell m}\}$, for a given cosmological model. A map with any desired level of non-Gaussianity, f_{NL}, can then be realized by linear combination,

$$a_{\ell m} = a_{\text{L }\ell m} + f_{\text{NL}} \cdot a_{\text{NL }\ell m}\,. \tag{2.3}$$

The expansion coefficients $a_{\ell m}$ of the CMB temperature and polarization anisotropies in harmonic space are related to the primordial fluctuations $\Phi_{\ell m}(k)$ via the equation (Komatsu et al. 2003)

$$a_{\ell m}^i = \frac{(-\imath)^\ell}{2\pi^2} \int dk\, k^2\ \Phi_{\ell m}(k)\ g_\ell^i(k)\,. \tag{2.4}$$

Here, $g_\ell^i(k)$ is the transfer function of temperature ($i = T$) or polarization ($i = E$) in momentum space. Analogously, we can define an equivalent equation as a function of comoving distance,

$$a_{\ell m}^i = \int dr\, r^2\ \Phi_{\ell m}(r)\ \alpha_\ell^i(r)\,, \tag{2.5}$$

where we have used the real space transfer function according to

$$\alpha_\ell^i(r) = \frac{2}{\pi} \int dk\, k^2\ g_\ell^i(k)\ j_\ell(kr)\,, \tag{2.6}$$

where $j_\ell(kr)$ denotes the spherical Bessel function of order ℓ.

We can now outline our recipe for simulating non-Gaussian CMB maps as following: (i) Generate the multipole moments of a purely Gaussian gravitational potential $\Phi_{\text{L }\ell m}(r)$ as a function of conformal distance. (ii) Compute the spherical harmonic transform to derive the corresponding expression in pixel space, $\Phi_{\text{L}}(r)$. (iii) Square it and subtract the variance according to Eq. 2.2 to get the non-Gaussian potential $\Phi_{\text{NL}}(r)$. (iv) Inverse transform to spherical harmonic space to obtain $\Phi_{\text{NL }\ell m}(r)$. (v) Solve the radial integral Eq. 2.5 for $\Phi_{\text{L }\ell m}(r)$ and $\Phi_{\text{NL }\ell m}(r)$ separately to compute $\{a_{\text{L }\ell m}^T,\ a_{\text{L }\ell m}^E;\ a_{\text{NL }\ell m}^T,\ a_{\text{NL }\ell m}^E\}$.

One difficulty in this approach is that we have to take into account the radial correlation of the gravitational potential in step (i). Its covariance matrix is determined by the primordial power spectrum predicted by inflation, $\mathcal{P}(k)$, and is given by (Liguori et al. 2003)

$$\left\langle \Phi_{\text{L }\ell_1 m_1}(r_1)\, \Phi_{\text{L }\ell_2 m_2}^*(r_2) \right\rangle = 4\pi\, \delta_{\ell_2}^{\ell_1}\, \delta_{m_2}^{m_1} \int dk\, \frac{\Delta_{\mathcal{R}}^2(k)}{k}\, j_{\ell_1}(kr_1)\, j_{\ell_2}(kr_2)\,, \tag{2.7}$$

where we have replaced $\mathcal{P}(k)$ by

$$\Delta_{\mathcal{R}}^2(k) = \frac{k^3}{2\pi^2} \cdot \mathcal{P}(k) \, , \qquad (2.8)$$

that is constant for vanishing spectral tilt ($n_s = 1$). The covariance matrix will be denoted by $P_{\Phi\,\ell}(r_1, r_2)$ in what follows. To draw a random realization of the linear gravitational potential at distances $\mathbf{r} = (r_1, r_2, \ldots, r_n)$, we calculate

$$\Phi_{\mathrm{L}\,\ell m}(\mathbf{r}) = P_{\Phi\,\ell}^{1/2} \cdot \mathbf{g} \, , \qquad (2.9)$$

where $\mathbf{g}$ is a vector of independent complex Gaussian random variables with zero mean and unit variance.

For this algorithm to run efficiently, we have to reduce the number of quadrature points in the numerical evaluation of the radial integral (Eq. 2.5), to keep the number of computationally expensive spherical harmonic transformations necessary to generate the non-Gaussian gravitational potential as low as possible. Details of the implementation together with an optimization scheme will be described in the next section.

2.3   Implementation and Optimization

To be able to perform the steps outlined in the last section, we first have to precompute the necessary auxiliary data. This needs to be done only once for a given set of cosmological parameters. First, we obtained the transfer functions in momentum space from a modified version of the latest CAMB software package[3] (Lewis et al. 2000). We then derived their equivalent expressions in real space using Eq. 2.6. Examples of temperature and polarization transfer functions as a function of conformal distance for several multipole moments are shown in Fig. 2.3.

As a next step, we calculate the covariance matrix of the gravitational potential on a fine grid with $N_{tot} = 400$ shells from the origin to the present time cosmic horizon (Eq. 2.7). As a start, we resolve the last scattering surface with uniform spacing using an increment of $\Delta r \approx 3.5\ Mpc$ and chose a larger interval elsewhere ($\Delta r \approx 100\ Mpc$). This simple approach will be refined later. Using the derived quantities, it is now possible to generate

---
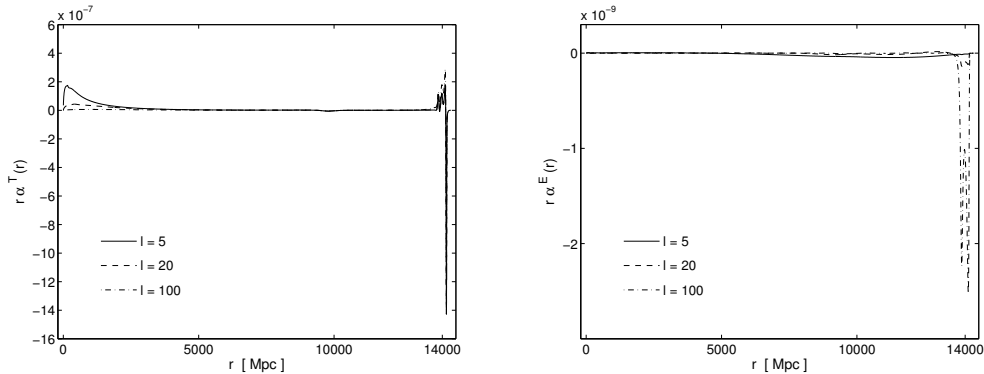
[3]Obtained from `http://camb.info`

Figure 2.1: Real space transfer functions. We show examples of the real space transfer functions of temperature (*left panel*) and polarization (*right panel*) for three different multipole moments $\ell = 5$, 20, and 100. At low ℓ, the effect of the late time ISW effect is clearly visible. Reionization occurred at about $r = 10 \ Gpc$.

$\Phi_{\mathrm{L} \ \ell m}(r_i)$, $\Phi_{\mathrm{NL} \ \ell m}(r_i)$ and numerically solve the radial integral Eq. 2.5 to obtain simulated non-Gaussian CMB maps. However, significant improvement in the numerical evaluation of the integral is achievable by choosing both weights and quadrature points in an optimal way, as we will show in the following.

Keeping the multipole moment (ℓ, m) fixed for simplicity, we want to accurately compute the integral

$$I = \int dr \, r^2 \, \alpha(r) \, \Phi(r) \,. \tag{2.10}$$

This is done in a two step process: We first approximate Eq. 2.10 with a discrete sum over N_{tot} shells. Then, we try to obtain comparable accuracy with fewer shells $N \ll N_{tot}$ introducing weights,

$$\hat{I} = \sum_{i=1}^{N} w_i \, \Phi(r_i) \,, \tag{2.11}$$

49

where the gravitational potential is evaluated at the nodes r_i and weighted by the factors w_i. Now, we can derive the expectation value of the quadratic error

$$\langle(\hat{I}-I)^2\rangle = \sum_{k=1}^{N_{tot}} \lambda_k \left(\int dr\, r^2\, \alpha(r)\, \phi_k(r)\right)^2 - w^T P_\Phi w\,, \qquad (2.12)$$

where we have introduced the eigenvalues λ_k and eigenvectors ϕ_k of the covariance matrix of the potential on the fine grid with $N_{tot} = 400$ elements. We show λ_k for several multipole moments in the left panel of Fig. 2.3. If the eigenvalues decrease sufficiently fast, the error is expected to be low already for a small number of quadrature points N. This seems especially to be true on large angular scales. However, this finding is partially counterbalanced by the fact that the transfer functions are significantly different from zero at small radii for low multipole moments (late ISW effect, reionization), enforcing the inclusion of additional nodes.

Based on the expression for the expected quadratic error, it is straightforward to calculate optimal weights by satisfying the condition $\frac{\partial}{\partial w_i}\langle(\hat{I}-I)^2\rangle = 0$, which leads to a system of N linear equations,

$$\sum_{j=1}^{N} P_{\Phi\,ij}(r_i, r_j)\, w_j = \sum_{k=1}^{N_{tot}} \lambda_k\, \phi_k(r_i) \int dr\, r^2\, \alpha(r)\, \phi_k(r)\,. \qquad (2.13)$$

Even more important, Eq. 2.12 allows us to formulate a greedy algorithm to compute optimal quadrature points. We select a subset of nodes out of the fine radial grid with 400 elements iteratively, in each step including the point that most efficiently reduces the remaining error. To simultaneously optimize for temperature and polarization, we add the expectation values of the two errors with equal weights. We use the outcome of the procedure to tune the radii of the input grid with 400 elements. We choose a smaller spacing down to $\Delta r = 1.2\ Mpc$ at the last scattering surface, where nodes were selected with the highest priority, and a larger step size up to $\Delta r = 140\ Mpc$ at distances, where the quadrature points were classified as less important. Then, we repeated the optimization process a second time. In the right panel of Fig. 2.3, we visualize the first 100 iterations of the optimization scheme. We display the expectation value of the relative quadratic error for $N = 30$, 50 and $N = 70$ quadrature points in Fig. 2.3. The raise in error towards the largest angular scales is caused by the increasing contribution from late ISW effect and reionization.
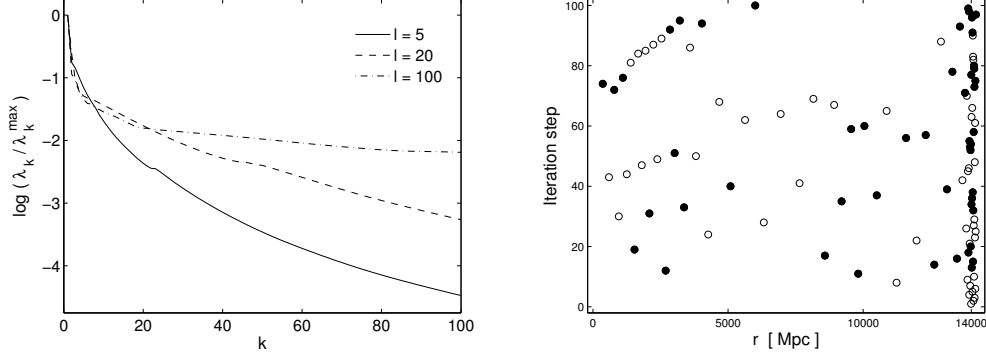
Figure 2.2: Optimization scheme. *Left panel:* We display the largest 100 eigenvalues λ_k of the covariance matrix of $\Phi_{L\,\ell}(r)$, normalized and in descending order for $\ell = 5$, 20, and 100. For low multipole moments, the number of quadrature points can be reduced most efficiently. *Right panel:* The radial positions of the shells included in the first 100 iteration steps. For illustrative purposes, we interchanged open and filled symbols every 10 iterations. The most important nodes are included first.
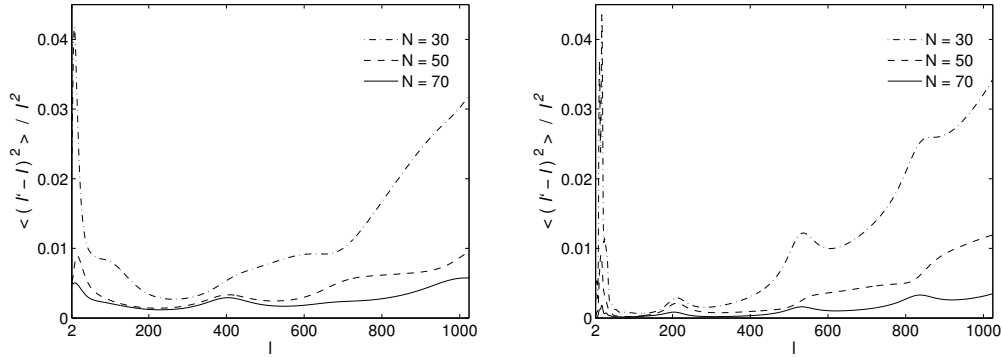

Figure 2.3: Error of integration. We depict the relative mean quadratic error introduced by approximating the integral Eq. 2.5 by a sum over $N = 30$, 50, and 70 elements for temperature (*left panel*) and polarization (*right panel*).

As a last step, we show how to reduce the memory consumption of the code. Whereas the potentials $\Phi_{\text{L} \ \ell m}(r)$ and $\Phi_{\text{NL} \ \ell m}(r)$ can be co–added to the spherical harmonic coefficients of the CMB map $a^i_{\text{L} \ \ell m}$ and $a^i_{\text{NL} \ \ell m}$ (Eq. 2.5) one shell after another, the radial correlation of $\Phi_{\text{L}}(r)$ forces one to generate it at all N shells simultaneously, potentially requiring large amounts of memory. To circumvent this problem, we keep the random seeds that were used to draw the potential. By means of the seeds, we are able to easily regenerate the gravitational potential at any radii $(r_1, r_2, \ldots, r_N)$. Thus, we only store its real space representation at the radius that is currently added to the CMB map, substantially reducing the overall memory consumption of the algorithm.

Having optimized the simulation algorithm in this way, we generated $N_{sim} = 1000$ realizations of temperature and polarization CMB maps. We chose a HEALPix resolution parameter of $n_{side} = 512$ and a maximum multipole moment of $\ell_{max} = 1024$. We used $N = 70$ quadrature points for evaluation of Eq. 2.5, although we stress that this choice is conservative and it is possible to derive reasonable results with smaller values of N.

With these input parameters, we aim for sub–percentage accuracy of the final map over the entire range of multipole moments, guided by the intrinsic precision of the underlying transfer functions, running CAMB with RECFAST at standard accuracy. An example is displayed in Fig. 2.3, where we illustrate a realization of temperature and polarization maps of the linear and non–linear part of the CMB. We show the averaged power spectra of all simulations along with a comparison to the theoretical values in Fig. 2.3. A detailed comparison to the expected statistical fluctuations ($\propto N_{sim}^{-1/2}$) reveals remaining slight systematic deviations for the TT and EE spectra at high ℓ at the level of less than 1% of the input power spectrum. If required this error could be further reduced by adding integration nodes. It takes about 20 minutes to generate a single map with the given resolution on a single Intel Xenon processor with a clock rate of 2.33 GHz, requiring only a modest amount of memory ($\approx 400 \ MB$). The most time consuming part is the evaluation of the spherical harmonic transforms necessary to compute the non-Gaussian potential.

The algorithm described here generates valid realizations of primordial curvature perturbations in real space. This itself is an interesting quantity and can be used to e.g. test the performance of reconstruction techniques as we will show in the next section. We visualize the 3D gravitational potential

$\Phi_{\mathrm{L}}(r)$ and $\Phi_{\mathrm{NL}}(r)$ in Fig. 2.3; long–distance correlations on large scales are in evidence.

Our simulation algorithm is conceptually very similar to the method proposed in Liguori et al. (2007), where the authors generate the gravitational potential on 400 shells, requiring 800 spherical harmonic transforms to calculate a single non-Gaussian CMB map, and report a runtime of 3 hours for $\ell_{max} = 500$. By applying our optimized quadrature scheme, we have demonstrated that it is possible to reduce the number of transforms considerably, resulting in an increase of computational efficiency. Another, albeit more formal difference is the way the gravitational potential is generated. We use the real space covariance matrix to draw $\Phi_{\mathrm{L}}(r)$ directly, whereas the authors of Liguori et al. (2007) compute the gravitational potential by performing an integral over uncorrelated random numbers weighted by 'filter' functions.

In Smith & Zaldarriaga (2006), where the authors focused on a perturbative reproduction of the correct bispectrum in the regime of weak non-Gaussianity, a runtime of about three minutes is reported to simulate one non-Gaussian CMB temperature map at an angular resolution of $\ell_{max} = 1000$. Although slower by an order of magnitude, and tuned for local non-Gaussianity, the algorithm presented here is capable of simulating both temperature and polarization maps (i.e. three maps for the stokes parameter I, Q, and U) within the same framework and with nearly the same computational cost compared to temperature alone. Furthermore, as recently pointed out by Hanson et al. (2009), in the case of local non-Gaussianity an additional modification of the algorithm of Smith & Zaldarriaga (2006) is necessary to suppress the power spectrum of the non-Gaussian part of a simulated map, found to be artificially enhanced by several orders of magnitudes on large angular scales.

Notwithstanding the aforementioned higher computational costs, we regard our method as useful for the study of local non-Gaussianity, because the simulated maps are well suited to test any kind of estimator, e.g. based on Minkowsky functionals (Spergel et al. 2007; Hikage et al. 2008), or a wavelet analysis (Martínez-González et al. 2002; Mukherjee & Wang 2004). If a detection of nonzero f_{NL} is reported, it will be important to confirm the result with alternative statistical tools, as they are sensitive to different systematic effects.

In the following section, we apply the KSW estimator (Komatsu et al. 2005) to our set of simulated maps with known non-Gaussian contribution to test whether the input values for f_{NL} can be recovered.
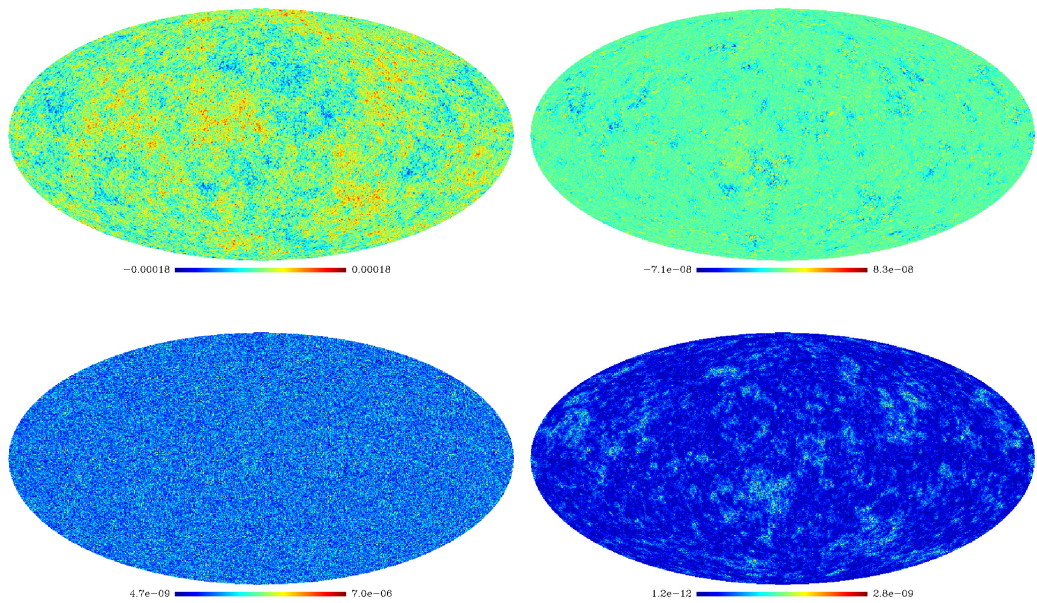
Figure 2.4: Example of simulated non-Gaussian map. We show the linear (*left column*) and the associated non–linear part (*right column*) of a realization of temperature (*first row*) and polarization intensity (*second row*) CMB data. The polarization intensity is defined as $I = \sqrt{Q^2 + U^2}$, where Q and U are the Stokes parameters.
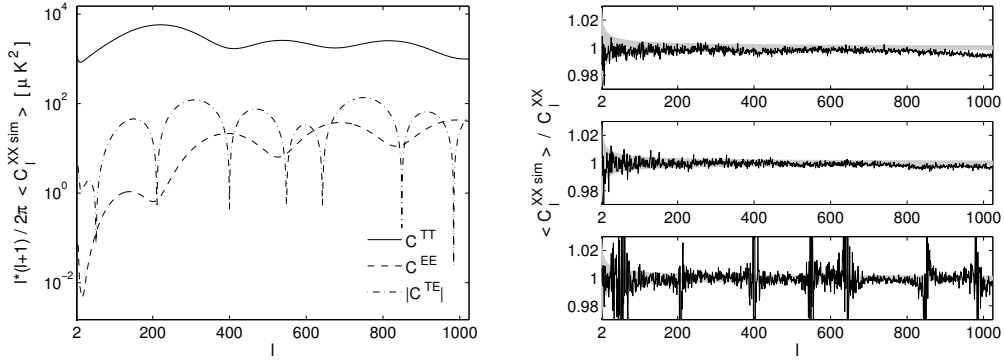
Figure 2.5: Averaged power spectra. *Left panel:* We display the power spectra $\mathcal{C}^{TT}$, $\mathcal{C}^{EE}$, and $\mathcal{C}^{TE}$ of the linear part of the simulated CMB maps, averaged over 1000 simulations. We do not show the input power spectra here, as the lines cannot be discerned in this view. *Right panels:* The ratio of the power spectra divided by their theoretical values for temperature ($XX = TT$, *upper sub–panel*), polarization ($XX = EE$, *middle sub–panel*), and cross–power spectrum ($XX = TE$, *lower sub–panel*). Oscillatory features in the latter are caused by roots of the denominator. The grayish area indicates the 2-σ bounds of an ideal simulation code. Sub-percentage, systematic deviations for the TT and EE spectra remain but are consistent with the precision goal.
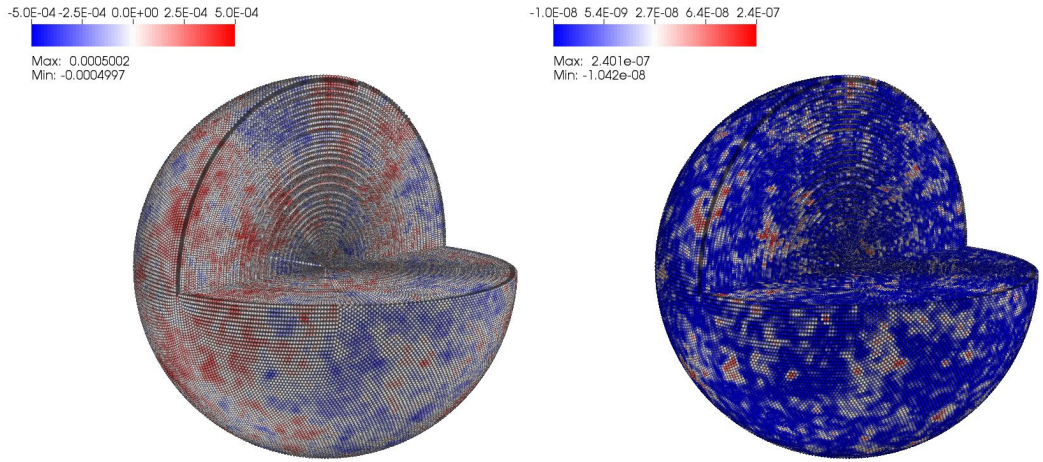
Figure 2.6: Examples for simulated curvature perturbations. *Left panel:* We visualize the linear gravitational potentials $\Phi_L(r)$, generated on $N = 70$ shells from the origin (*center*) to the last scattering surface (*outermost shells*). *Right panel:* The associated non-Gaussian potential, displayed at nonlinear scale.

2.4 Bispectrum Analysis

As we do not aim to describe the fast estimator in detail, we include a brief summary here and refer the reader to the extensive literature for further details and a comprehensive discussion (e.g. in Komatsu et al. 2005; Smith & Zaldarriaga 2006; Creminelli et al. 2007; Yadav et al. 2007).

To estimate the non-Gaussianity of a CMB map, one constructs the statistic $\mathcal{S}_{prim}$ out of a cubic combination of the data,

$$\mathcal{S}_{prim} = \int dr\, r^2 \int d^2\hat{n}\; A(r,\hat{n})\; B^2(r,\hat{n})\,. \qquad (2.14)$$

The radial integral runs over two filtered maps,

$$A(r,\hat{n}) = \sum_{i,j=T,E}\; \sum_{\ell,m} (\mathcal{C}^{-1})_\ell^{ij} \alpha_\ell^i(r)\; a_{\ell m}^j\; Y_{\ell m}(\hat{n})\,, \qquad (2.15)$$

$$B(r,\hat{n}) = \sum_{i,j=T,E}\; \sum_{\ell,m} (\mathcal{C}^{-1})_\ell^{ij} \beta_\ell^i(r)\; a_{\ell m}^j\; Y_{\ell m}(\hat{n})\,, \qquad (2.16)$$

56

that are constructed using the auxiliary functions

$$\alpha_\ell^i(r) = \frac{2}{\pi} \int dk\, k^2\, g_\ell^i(k)\, j_\ell(kr)\,, \tag{2.17}$$

$$\beta_\ell^i(r) = 4\pi \int dk\, \frac{\Delta_\mathcal{R}^2(k)}{k}\, g_\ell^i(k)\, j_\ell(kr)\,, \tag{2.18}$$

and the inverse of the matrix containing the CMB power spectrum elements,

$$\mathcal{C}_\ell^{-1} = \begin{pmatrix} \mathcal{C}_\ell^{TT} & \mathcal{C}_\ell^{TE} \\ \mathcal{C}_\ell^{TE} & \mathcal{C}_\ell^{EE} \end{pmatrix}^{-1}. \tag{2.19}$$

One of these maps, $B(r, \hat{n})$, is exactly the Wiener filter reconstruction of the underlying gravitational potential $\Phi(r)$. With the simulation algorithm presented in Sect. 2.2, it is possible to compare the potential used to synthesize the map with its reconstruction directly. An example is shown in Fig. 2.4, where we depict the reconstruction of the potential around last scattering using only temperature, and using both, temperature and polarization information.

As the estimator $\mathcal{S}_{prim}$ is proportional to the non-Gaussianity parameter f_{NL}, we can calculate its expectation value by applying a suitable normalization,

$$f_{\mathrm{NL}} = \left[\sum_{\substack{i,j,k,o,p,q \\ =T,E}} \sum_{\ell_1 \le \ell_2 \le \ell_3} \frac{1}{\Delta_{\ell_1\ell_2\ell_3}} B_{\ell_1\ell_2\ell_3}^{ijk,\,prim} (\mathcal{C}^{-1})_{\ell_1}^{io} (\mathcal{C}^{-1})_{\ell_2}^{jp} (\mathcal{C}^{-1})_{\ell_3}^{kq} \right.$$

$$\left. \times B_{\ell_1\ell_2\ell_3}^{opq,\,prim} \right]^{-1} \cdot \mathcal{S}_{prim}\,, \quad (2.20)$$

where $\Delta_{\ell_1\ell_2\ell_3} = 6$, when $\ell_1 = \ell_2 = \ell_3$, 2, when $\ell_1 = \ell_2 \ne \ell_3$ or $\ell_1 \ne \ell_2 = \ell_3$, and 1 otherwise. We further introduced the theoretical bispectrum for $f_{\mathrm{NL}} = 1$, $B_{\ell_1\ell_2\ell_3}^{ijk,prim}$, which is defined as

$$B_{\ell_1\ell_2\ell_3}^{ijk,\,prim} = 2\, I_{\ell_1\ell_2\ell_3} \int dr\, r^2\, [\beta_{\ell_1}^i(r)\beta_{\ell_2}^j(r)\alpha_{\ell_3}^k(r) + \beta_{\ell_3}^k(r)\beta_{\ell_1}^i(r)\alpha_{\ell_2}^j(r)$$

$$+ \beta_{\ell_2}^j(r)\beta_{\ell_3}^k(r)\alpha_{\ell_1}^i(r)]\,, \quad (2.21)$$

where the prefactor is given by

$$I_{\ell_1 \ell_2 \ell_3} = \sqrt{\frac{(2\ell_1 + 1)(2\ell_2 + 1)(2\ell_3 + 1)}{4\pi}} \begin{pmatrix} \ell_1 & \ell_2 & \ell_3 \\ 0 & 0 & 0 \end{pmatrix}. \qquad (2.22)$$

We used the equations above to implement the fast estimator for temperature and polarization. As our primary goal is to validate our simulation algorithm, we do not take into account possible instrumental effects, sky cut, or noise. To test our simulations, we generate two sets of 1000 CMB temperature and polarization maps with resolution parameter $n_{side} = 512$, and $\ell_{max} = 1024$. We consider one sample of purely Gaussian realizations of the CMB sky ($f_{NL} = 0$), and one non-Gaussian sample with a fiducial value of $f_{NL} = 100$. We then run the fast estimator on the maps to compute an estimate of f_{NL}. We show the distribution of the derived values in Fig. 2.4. We find the input parameters to be recovered well, the means of the distributions are $\langle f_{NL}^{G} \rangle = -0.1$ and $\langle f_{NL}^{NG} \rangle = 98.4$ for the Gaussian and non-Gaussian simulations, respectively. The estimated standard deviations are $\sigma_{f_{NL}^{G}} = 2.4$ and $\sigma_{f_{NL}^{NG}} = 8.4$, compared to the expected error predicted from a Fisher information matrix analysis of $\sigma_{f_{NL}}^{Fisher} = 2.4$. We conclude that the algorithm outlined in Sect. 2.2 and implemented as described in Sect. 2.3 produces valid realizations of non-Gaussian CMB temperature and polarization maps.

2.5   Summary

In this paper, we introduced a new algorithm to simulate temperature and polarization CMB maps containing non-Gaussianity of arbitrary local type. In the proposed scheme, we generate spherical harmonic coefficients of the Gaussian potential as a function of conformal distance, taking into account the proper radial correlations. Then, the potential is transformed to pixel space to compute the associated non-Gaussian contribution. Finally, we make use of the real space representation of the transfer functions to perform the line of sight integral in order to calculate Gaussian and non-Gaussian contribution to the CMB maps.

We developed and applied a quadrature scheme that allows us to increase the numerical efficiency of the code. As a starting point, we derived an expression to quantitatively calculate the mean error introduced by replacing the radial integral by a finite sum. On that basis, we were able to choose
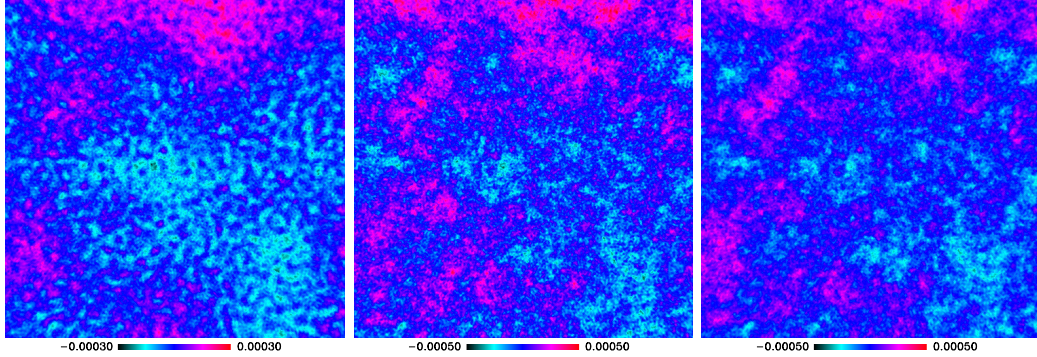
Figure 2.7: Wiener filter reconstruction of the gravitational potential. We illustrate the input gravitational potentials $\Phi_L(r)$ at the last scattering surface $r = 14.0$ *Gpc* (*middle panel*) used to generate a simulated CMB map and its Wiener filter reconstruction based solely on temperature data (*left panel*), and based on both, temperature and polarization data (*right panel*) of the same map. Each patch is 50° on the side.
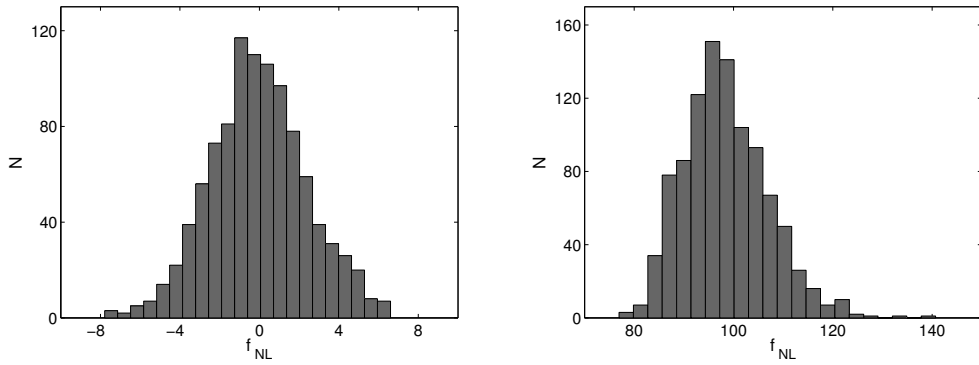

Figure 2.8: Histogram of the recovered f_{NL} values. We display the distribution of estimated f_{NL} values when applying the fast estimator to 1000 realization of temperature and polarization CMB maps. The input values used for the simulations were $f_{\mathrm{NL}} = 0$ (*left panel*), and $f_{\mathrm{NL}} = 100$ (*right panel*).

both, nodes and weights for numerical quadrature in an optimal way. As a last step, we successfully reduced the memory consumption of the algorithm.

For WMAP5+BAO+SN cosmological parameters, we simulated 1000 realizations of non-Gaussian CMB temperature and polarization maps with resolution parameters $n_{side} = 512$ and $\ell_{max} = 1024$. To validate the algorithm, we applied the well studied and widely accepted fast cubic (bispectrum) estimator to the simulations. For both, a set of Gaussian and non-Gaussian realizations of CMB sky maps, the input parameters were consistently recovered. We make our simulations publicly available at `http://planck.mpa-garching.mpg.de/cmb/fnl-simulations`.

Bibliography

Alishahiha, M., Silverstein, E., & Tong, D. 2004, Phys. Rev. D, 70, 123505

Bardeen, J. M., Steinhardt, P. J., & Turner, M. S. 1983, Phys. Rev. D, 28, 679

Chen, X. 2005, Phys. Rev. D, 72, 123518

Creminelli, P., Senatore, L., & Zaldarriaga, M. 2007, J. Cosmology Astropart. Phys., 3, 19

Enqvist, K. & Sloth, M. S. 2002, Nuclear Physics B, 626, 395

Górski, K. M., Hivon, E., Banday, A. J., et al. 2005, ApJ, 622, 759

Guth, A. H. 1981, Phys. Rev. D, 23, 347

Hanson, D., Smith, K. M., Challinor, A., & Liguori, M. 2009, Phys. Rev. D, 80, 083004

Hikage, C., Matsubara, T., Coles, P., et al. 2008, MNRAS, 389, 1439

Khoury, J., Ovrut, B. A., Steinhardt, P. J., & Turok, N. 2001, Phys. Rev. D, 64, 123522

Komatsu, E., Kogut, A., Nolta, M. R., et al. 2003, ApJS, 148, 119

Komatsu, E. & Spergel, D. N. 2001, Phys. Rev. D, 63, 063002

Komatsu, E., Spergel, D. N., & Wandelt, B. D. 2005, ApJ, 634, 14

Langlois, D., Renaux-Petel, S., Steer, D. A., & Tanaka, T. 2008, Phys. Rev. D, 78, 063523

Lehners, J.-L. & Steinhardt, P. J. 2008, Phys. Rev. D, 77, 063533

Lewis, A., Challinor, A., & Lasenby, A. 2000, ApJ, 538, 473

Liguori, M., Matarrese, S., & Moscardini, L. 2003, ApJ, 597, 57

Liguori, M., Yadav, A., Hansen, F. K., et al. 2007, Phys. Rev. D, 76, 105016

Lyth, D. H., Ungarelli, C., & Wands, D. 2003, Phys. Rev. D, 67, 023503

Martínez-González, E., Gallegos, J. E., Argüeso, F., Cayón, L., & Sanz, J. L. 2002, MNRAS, 336, 22

Moroi, T. & Takahashi, T. 2001, Physics Letters B, 522, 215

Mukhanov, V. F., Feldman, H. A., & Brandenberger, R. H. 1992, Phys. Rep., 215, 203

Mukherjee, P. & Wang, Y. 2004, ApJ, 613, 51

Senatore, L. 2005, Phys. Rev. D, 71, 043512

Smith, K. M. & Zaldarriaga, M. 2006, ArXiv Astrophysics e-prints

Spergel, D. N., Bean, R., Doré, O., et al. 2007, ApJS, 170, 377

Steinhardt, P. J. & Turok, N. 2002, Phys. Rev. D, 65, 126003

Verde, L., Wang, L., Heavens, A. F., & Kamionkowski, M. 2000, MNRAS, 313, 141

Yadav, A. P. S., Komatsu, E., & Wandelt, B. D. 2007, ApJ, 664, 680

Chapter 3

Probing local non-Gaussianities within a Bayesian framework

Franz Elsner[1], Benjamin D. Wandelt[2,3], and Michael D. Schneider[4]

[1]Max-Planck-Institut für Astrophysik, Karl-Schwarzschild-Straße 1, 85748 Garching, Germany

[2]Department of Physics, University of Illinois at Urbana-Champaign, 1110 W. Green Street, Urbana, IL 61801, USA

[3]Department of Astronomy, University of Illinois at Urbana-Champaign, 1002 W. Green Street, Urbana, IL 61801, USA

[4]Institute for Computational Cosmology, Department of Physics, Durham University, South Road, Durham, DH1 3LE, UK

Abstract

Aims. We outline the Bayesian approach to inferring f_{NL}, the level of non-Gaussianities of local type. Phrasing f_{NL} inference in a Bayesian framework takes advantage of existing techniques to account for instrumental effects and foreground contamination in CMB data and takes into account uncertainties in the cosmological parameters in an unambiguous way.

Methods. We derive closed form expressions for the joint posterior of f_{NL} and the reconstructed underlying curvature perturbation, Φ, and deduce the conditional probability densities for f_{NL} and Φ. Completing the inference problem amounts to finding the marginal density for f_{NL}. For realistic data sets the necessary integrations are intractable. We propose an exact Hamiltonian sampling algorithm to generate correlated samples from the f_{NL} posterior. For sufficiently high signal-to-noise ratios, we can exploit the assumption of weak non-Gaussianity to find a direct Monte Carlo technique to generate *independent* samples from the posterior distribution for f_{NL}. We illustrate our approach using a simplified toy model of CMB data for the simple case of a 1-D sky.

Results. When applied to our toy problem, we find that, in the limit of high signal-to-noise, the sampling efficiency of the approximate algorithm outperforms that of Hamiltonian sampling by two orders of magnitude. When f_{NL} is not significantly constrained by the data, the more efficient, approximate algorithm biases the posterior density towards $f_{\mathrm{NL}} = 0$.

3.1 Introduction

The analysis of cosmic microwave background (CMB) radiation data has considerably improved our understanding of cosmology and played a crucial role in constraining the set of fundamental cosmological parameters of the universe (Spergel et al. 2007; Hinshaw et al. 2009). This success is based on the intimate link between the temperature fluctuations we observe today and the physical processes taking place in the very early universe. Inflation is currently the favored theory predicting the shape of primordial perturbations (Guth 1981; Linde 1982), which in its canonical form leads to very small non-Gaussianities that are far from being detectable by means of present-day experiments (Acquaviva et al. 2003; Maldacena 2003). However, inflation scenarios producing larger amounts of non-Gaussianity can naturally be constructed by breaking one or more of the following properties of canonical inflation: slow-roll, single-field, Bunch-Davies vacuum, or a canonical kinetic term (Bartolo et al. 2004). Thus, a positive detection of primordial non-Gaussianity would allow us to rule out the simplest models. Combined with improving constraints on the scalar spectral index n_s, the test for non-Gaussianity is therefore complementary to the search for gravitational waves as a means to test the physics of the early Universe.

A common strategy for estimating primordial non-Gaussianity is to examine a cubic combination of filtered CMB sky maps (Komatsu et al. 2005). This approach takes advantage of the specific bispectrum signatures produced by primordial non-Gaussianity and yields to a computationally efficient algorithm. When combined with the variance reduction technique first described by Creminelli et al. (2006) these bispectrum-based techniques are close to optimal, where optimality is defined as saturation of the Cramer-Rao bound. Lately, a more computationally costly minimum variance estimator has been implemented and applied to the WMAP5 data (Smith et al. 2009).

Recently, a Bayesian approach has been introduced in CMB power spectrum analysis and applied successfully to WMAP data making use of Gibbs-sampling techniques (Jewell et al. 2004; Wandelt et al. 2004). Within this framework, one draws samples from the posterior probability density given the data without explicitly calculating it. The target probability distribution is finally constructed out of the samples directly, thus computationally costly evaluations of the likelihood function or its derivatives are not necessary. Another advantage of the Bayesian analysis is that the method naturally offers the possibility to include a consistent treatment of the uncertainties

associated with foreground emission or instrumental effects (Eriksen et al. 2008). As it is possible to model CMB and foregrounds jointly, statistical interdependencies can be directly factored into the calculations. This is not straightforward in the frequentist approach where the data analysis is usually performed in consecutive steps. Yet another important and desirable feature is the fact that a Bayesian analysis obviates the necessity to specify fiducial parameters, whereas in the frequentist approach it is only possible to test one individual null hypothesis at a time.

In this paper, we pursue the modest goal of developing the formalism for the extension of the Bayesian approach to the analysis of non-Gaussian signals, in particular to local models, where the primordial perturbations can be modeled as a spatially local, non-linear transformation of a Gaussian random field. Utilizing this method, we are able to write down the full posterior probability density function (PDF) of the level of non-Gaussianity. We demonstrate the principal aspects of our approach using a 1-D toy sky model. Although we draw our discussion on the example of CMB data analysis, the formalism presented here is of general validity and may also be applied within a different context.

The paper is organized as follows. In Sect. 3.2 we give a short overview of the theoretical background used to characterize primordial perturbations. We present a new approximative approach to extract the amplitude of non-Gaussianities from a map in Sect. 3.3 and verify the method by means of a simple synthetic data model (Sect. 3.4). After addressing the question of optimality in Sect. 3.5, we compare the performance of our technique to an exact Hamiltonian Monte Carlo sampler which we develop in Sect. 3.6 and discuss the extensions of the model required to deal with a realistic CMB sky map (Sect. 3.7). Finally, we summarize our results in Sect. 3.8.

3.2 Model of non-Gaussianity

The expansion coefficients $a_{\ell m}$ of the observed CMB temperature anisotropies in harmonic space can be related to the primordial fluctuations via

$$a_{\ell m} = \frac{2b_\ell}{\pi} \int k^2 dk \, r^2 dr \, [\, \Phi_{\ell m}(r) \, g_\ell^{adi}(k) + S_{\ell m}(r) \, g_\ell^{iso}(k) \,] \, j_\ell(kr) + n_{\ell m} \,, \quad (3.1)$$

where $\Phi_{\ell m}(r)$ and $S_{\ell m}(r)$ are the primordial curvature and isocurvature perturbations at comoving distance r, $g_\ell^{adi}(k)$ and $g_\ell^{iso}(k)$ their corresponding

transfer functions in momentum space. The spherical Bessel function of order ℓ is denoted by $j_\ell(kr)$, b_ℓ includes beam smearing effects, and $n_{\ell m}$ describes instrumental noise. As curvature perturbations dominate over isocurvature perturbations (Bean et al. 2006; Trotta 2007), we will neglect the contribution of $S_{\ell m}$ in our subsequent analysis.

Any non-Gaussian signature imprinted in the primordial perturbations will be transferred to the $a_{\ell m}$ according to Eq. 3.1 and is therefore detectable, in principle. Theoretical models predicting significant levels of non-Gaussian contributions to the observed signal can be subdivided into two broad classes (Babich et al. 2004): one producing non-Gaussianity of *local* type, the other of *equilateral* type. The former kind of non-Gaussianity is achieved to very good approximation in multi-field inflation as described by the curvaton model (Moroi & Takahashi 2001; Lyth et al. 2003), or in cyclic/ekpyrotic universe models (Khoury et al. 2001; Enqvist & Sloth 2002; Steinhardt & Turok 2002). The latter type of non-Gaussianity is typically a result of single field models with non-minimal Lagrangian including higher order derivatives (Alishahiha et al. 2004; Senatore 2005).

Concentrating on *local* models, we can parametrize the non-Gaussianity of Φ by introducing an additional quadratic dependence on a purely Gaussian auxiliary field Φ_L, that is local in real space, of the form (Verde et al. 2000; Komatsu & Spergel 2001)

$$\Phi_{NL}(r) = \Phi_L(r) + f_{NL}[\Phi_L^2(r) - \langle \Phi_L^2(r) \rangle]\,, \tag{3.2}$$

where f_{NL} is a dimensionless measure of the amplitude of non-Gaussianity.

3.3 Bayesian inference of non-Gaussianity

It has been shown to be feasible to reconstruct the primordial curvature potential out of temperature or temperature and polarization sky maps (Yadav & Wandelt 2005; Elsner & Wandelt 2009), which allows searching for primordial non-Gaussianities more sensitively. Although the mapping from a 3D potential to a 2D CMB sky map is not invertible unambiguously, a unique solution can be found by requiring that the result minimizes the variance. In this conventional frequentist approach, the level of non-Gaussianity and an estimate of its error is derived from a cubic combination of filtered sky maps (Komatsu et al. 2005). We will show in the following sections how to

sample f_{NL} from the data and unveil the full posterior PDF using a Bayesian approach.

3.3.1 Joint probability distribution

In our analysis we assume the data vector d to be a superposition of the CMB signal s and additive noise n

$$
\begin{aligned}
d &= Bs + n \\
&= BM\Phi + n \,,
\end{aligned}
\tag{3.3}
$$

where information about observing strategy and the optical system are encoded in a pointing matrix B and M is a linear transformation matrix. In harmonic space, the signal is related to the primordial scalar perturbation as

$$
\begin{aligned}
s_{\ell m} &= \frac{2}{\pi} \int k^2 dk \, r^2 dr \, \Phi_{\ell m}(r) \, g_\ell^{adi}(k) \, j_\ell(kr) \\
&\approx \sum_i M_i \Phi_{\ell m}(r_i) \\
&\equiv M\Phi_{\ell m} \,.
\end{aligned}
\tag{3.4}
$$

Our aim is to construct the posterior PDF of the amplitude of non-Gaussianities given the data, $P(f_{\mathrm{NL}}|d)$. To do so, we subsume the remaining set of cosmological parameters to a vector θ and calculate the joint distribution as

$$
P(d, \Phi_{\mathrm{L}}, f_{\mathrm{NL}}, \theta) = P(d|\Phi_{\mathrm{L}}, f_{\mathrm{NL}}, \theta) P(\Phi_{\mathrm{L}}|\theta) P(\theta) P(f_{\mathrm{NL}}) \,.
\tag{3.5}
$$

Now, we can use Eq. 3.2 to express the probability for data d given Φ_{L}, f_{NL}, and θ

$$
\begin{aligned}
P(d|\Phi_{\mathrm{L}}, f_{\mathrm{NL}}, \theta) = &\frac{1}{\sqrt{|2\pi N|}} \\
&\times \mathrm{e}^{-1/2\,[d-BM(\Phi_{\mathrm{L}}+f_{\mathrm{NL}}(\Phi_{\mathrm{L}}^2-\langle\Phi_{\mathrm{L}}^2\rangle))]^\dagger N^{-1}[d-BM(\Phi_{\mathrm{L}}+f_{\mathrm{NL}}(\Phi_{\mathrm{L}}^2-\langle\Phi_{\mathrm{L}}^2\rangle))]} \,,
\end{aligned}
\tag{3.6}
$$

where N is the noise covariance matrix. The prior probability distribution for Φ_{L} given θ can be expressed by a multivariate Gaussian by definition. Using the covariance matrix P_Φ of the potential, we derive

$$
P(\Phi_{\mathrm{L}}|\theta) = \frac{1}{\sqrt{|2\pi P_\Phi|}} \mathrm{e}^{-1/2\,\Phi_{\mathrm{L}}^\dagger P_\Phi^{-1}\Phi_{\mathrm{L}}} \,.
\tag{3.7}
$$

For flat priors $P(f_{\mathrm{NL}})$, $P(\theta)$ we finally obtain

$$P(d, \Phi_{\mathrm{L}}, f_{\mathrm{NL}}, \theta) \propto \exp \left\{ -\frac{1}{2} \left[(d - BM(\Phi_{\mathrm{L}} + f_{\mathrm{NL}}(\Phi_{\mathrm{L}}^2 - \langle \Phi_{\mathrm{L}}^2 \rangle)))^\dagger N^{-1} \right. \right.$$
$$\left. \left. \times (d - BM(\Phi_{\mathrm{L}} + f_{\mathrm{NL}}(\Phi_{\mathrm{L}}^2 - \langle \Phi_{\mathrm{L}}^2 \rangle))) + \Phi_{\mathrm{L}}^\dagger P_\Phi^{-1} \Phi_{\mathrm{L}} \right] \right\} \quad (3.8)$$

as an exact expression for the joint distribution up to a normalization factor.

To derive the posterior density, $P(f_{\mathrm{NL}}|d)$, one has to marginalize the joint distribution over Φ_{L} and θ. As it is not possible to calculate the high dimensional Φ_{L} integral directly, an effective sampling scheme must be found to evaluate the expression by means of a Monte Carlo algorithm. One possibility would be to let a Gibbs sampler explore the parameter space. Unfortunately, we were not able to find an efficient sampling recipe from the conditional densities for f_{NL} and Φ_{L} as the variables are highly correlated. An algorithm that also generates correlated samples, but is potentially suitable for non-Gaussian densities and high degrees of correlation is the Hamiltonian Monte Carlo approach. We will return to this approach in Sect. 3.6.

For now we attempt to go beyond correlated samplers and see whether we can develop an approximate scheme, valid in the limit of weak non-Gaussianity, to sample f_{NL} independently. We start out by expanding the target posterior distribution into an integral of conditional probabilities over the non-linear potential Φ_{NL},

$$P(f_{\mathrm{NL}}|d) = \int d\Phi_{\mathrm{NL}} d\theta \, P(f_{\mathrm{NL}}|\Phi_{\mathrm{NL}}, \theta) P(\Phi_{\mathrm{NL}}|d, \theta) P(\theta|d) \,. \quad (3.9)$$

To construct the conditional probability $P(\Phi_{\mathrm{NL}}|d, \theta)$ in the integrand, we need to find an equivalent equation for the joint distribution (Eq. 3.8) as a function of the field Φ_{NL}. However, a simple analytic expression for the prior distribution of Φ_{NL} does not exist because it is a non-linear transform of the Gaussian auxiliary field Φ_{L}. To quantify the expected correction, we calculate its covariance matrix,

$$\begin{aligned}
(P_{\Phi_{\mathrm{NL}}})_{ij} &= \langle (\Phi_{\mathrm{NL}})_i (\Phi_{\mathrm{NL}})_j \rangle \\
&= \langle (\Phi_{\mathrm{L}})_i (\Phi_{\mathrm{L}})_j \rangle + f_{\mathrm{NL}}^2 [\langle (\Phi_{\mathrm{L}})_i^2 (\Phi_{\mathrm{L}})_j^2 \rangle - \langle (\Phi_{\mathrm{L}})_i^2 \rangle \langle (\Phi_{\mathrm{L}})_j^2 \rangle] \\
&= (P_{\Phi_{\mathrm{L}}})_{ij} + 2 f_{\mathrm{NL}}^2 (P_{\Phi_{\mathrm{L}}})_{ij}^2 \,.
\end{aligned} \quad (3.10)$$

As the covariance matrix $P_{\Phi_{\mathrm{L}}}$ is of the order $\mathcal{O}(10^{-10})$ and the non-Gaussian contribution to Φ_{NL} is known to be small, we neglect the higher order

correction in the prior distribution in what follows. That is, we approximate the true prior probability function by a Gaussian distribution in Φ_{NL} and in this way derive a simple expression for the joint density, as a function of Φ_{NL},

$$P(d, \Phi_{\mathrm{NL}}, \theta) \propto \exp \left\{ -\frac{1}{2} \left[(d - BM\Phi_{\mathrm{NL}})^\dagger N^{-1} (d - BM\Phi_{\mathrm{NL}}) \right. \right.$$
$$\left. \left. + \Phi_{\mathrm{NL}}^\dagger P_\Phi^{-1} \Phi_{\mathrm{NL}} \right] \right\} . \quad (3.11)$$

Note, that the approximation applies to the second term only, the first part of the expression remains unaffected. As this approximation is equivalent to imposing the prior belief of purely Gaussian primordial perturbations, we expect to underestimate f_{NL} in the low signal-to-noise regime, as we tend to replace the Wiener filtered noise with purely Gaussian signal. Contrary, the method is unbiased when the likelihood dominates over the prior which is unlikely for data derived by the Planck mission.

The direct evaluation of the joint distributions over a grid in the high dimensional parameter space is computationally not feasible. One option would be to approximate the PDF around its maximum to get an expression for the attributed errors (Tegmark 1997; Bond et al. 1998). These methods are still computationally expensive and can also not recover the full posterior. An alternative approach to overcome these problems is to draw samples from the PDF which is to be evaluated as we will discuss in the next section.

3.3.2 Conditional probabilities

To construct the target posterior density Eq. 3.9, we have to find expressions for the conditional probabilities $P(\Phi_{\mathrm{NL}}|d, \theta)$ and $P(f_{\mathrm{NL}}|\Phi_{\mathrm{NL}}, \theta)$. The former distribution can easily be derived from the joint probability density Eq. 3.11. Since the exponent is quadratic in Φ_{NL} in our approximation, the conditional PDF of Φ_{NL} given d and θ is Gaussian. Therefore, we can calculate mean and variance of the distribution via differentiating the expression,

$$\langle \Phi_{\mathrm{NL}} \rangle = \langle (\Phi_{\mathrm{NL}} - \langle \Phi_{\mathrm{NL}} \rangle)^2 \rangle \, M^\dagger B^\dagger N^{-1} d$$
$$\langle (\Phi_{\mathrm{NL}} - \langle \Phi_{\mathrm{NL}} \rangle)^2 \rangle = \left[M^\dagger B^\dagger N^{-1} BM + P_\Phi^{-1} \right]^{-1} . \quad (3.12)$$

As a next step, we derive the conditional probability distribution of f_{NL} for given Φ_{NL}. This expression is not affected by the approximation and can be derived from a marginalization over Φ_{L},

$$
\begin{aligned}
P(f_{\mathrm{NL}}|\Phi_{\mathrm{NL}}, \theta) &= \int d\Phi_{\mathrm{L}}\, P(f_{\mathrm{NL}}|\Phi_{\mathrm{L}}, \Phi_{\mathrm{NL}})\, P(\Phi_{\mathrm{L}}|\theta) \\
&= \int d\Phi_{\mathrm{L}}\, \delta(\Phi_{\mathrm{NL}} - \Phi_{\mathrm{L}} - f_{\mathrm{NL}}(\Phi_{\mathrm{L}}^2 - \langle\Phi_{\mathrm{L}}^2\rangle))\, P(\Phi_{\mathrm{L}}|\theta)\,. \quad (3.13)
\end{aligned}
$$

Using Eq. 3.7, we can calculate the integral and obtain

$$
P(f_{\mathrm{NL}}|\Phi_{\mathrm{NL}}, \theta) \propto \left| \prod_i \frac{1}{1 + 2f_{\mathrm{NL}}(\tilde{\Phi}_{\mathrm{L}})_i} \right|\, \mathrm{e}^{-1/2\, \tilde{\Phi}_{\mathrm{L}}^\dagger P_\Phi^{-1} \tilde{\Phi}_{\mathrm{L}}}\,, \qquad (3.14)
$$

where $\tilde{\Phi}_{\mathrm{L}}$ is a function of f_{NL} and can be regarded as inversion of Eq. 3.2,

$$
\tilde{\Phi}_{\mathrm{L}} = \frac{1}{2f_{\mathrm{NL}}}\left[-1 + \sqrt{1 + 4f_{\mathrm{NL}}(\Phi_{\mathrm{NL}} + f_{\mathrm{NL}}\langle\Phi_{\mathrm{L}}^2\rangle)}\right]\,. \qquad (3.15)
$$

Note that we can resolve the ambiguity in sign in the weakly non-Gaussian limit (Babich 2005). Because the absolute value of the elements of the second solution is typically larger by orders of magnitude, the probability of its realization is strongly disfavored by the prior $P(\Phi_{\mathrm{L}})$. The factor of suppression is typically less than 10^{-1000} and further vanishing with decreasing f_{NL}.

After setting up the conditional densities, we now can sample from the distributions iteratively. First, we draw Φ_{NL} from a Gaussian distribution using Eqs. 3.12. Then, f_{NL} can be sampled according to Eq. 3.14 using the value of Φ_{NL} derived in the preceding step. Thus, the sampling scheme reads as

$$
\begin{aligned}
\Phi_{\mathrm{NL}}^i &\hookleftarrow P(\Phi_{\mathrm{NL}}|d, \theta) \\
f_{\mathrm{NL}}^i &\hookleftarrow P(f_{\mathrm{NL}}|\Phi_{\mathrm{NL}}^i, \theta)\,.
\end{aligned} \qquad (3.16)
$$

Note that this is *not* Gibbs sampling. For a fixed set of cosmological parameters, we can chain together samples from the conditional densities above, producing *independent* f_{NL} samples. The efficiency of such a direct Monte Carlo sampler is therefore expected to be much higher than that of a Gibbs sampler, which, in the general case, would produce correlated samples.

As an extension of the sampling scheme presented so far, we sketch an approach to account for uncertainties in cosmological parameters and foreground contributions. Complementing the scheme (Eqs. 3.16) by an additional step allows to take into account the error in the parameters θ,

$$
\begin{aligned}
\Phi_{\mathrm{NL}}^i &\hookleftarrow P(\Phi_{\mathrm{NL}}|d, \theta^{i-1}) \\
f_{\mathrm{NL}}^i &\hookleftarrow P(f_{\mathrm{NL}}|\Phi_{\mathrm{NL}}^i, \theta^{i-1}) \\
\theta^i &\hookleftarrow P(\theta|d, f_{\mathrm{NL}}^i)\,,
\end{aligned}
\tag{3.17}
$$

where the last equation updates the cosmological parameters that can be sampled from the data by means of standard Monte Carlo analysis tools[1]. Now, the scheme formally reads as a Gibbs sampler and can in principle take into account the correlation among f_{NL} and the other cosmological parameters exactly. In practice, however, the impact of a non-vanishing f_{NL} is expected to be negligible, i.e. $P(\theta|d, f_{\mathrm{NL}}) \approx P(\theta|d)$. Likewise, we can allow for an additional sampling step to deal with foreground contributions, e.g. from synchrotron, free-free, and dust emission. Foreground templates $f^{sync, free, dust}$, that are available for these sources, can be subtracted with amplitudes $c^{sync, free, dust}$ which are sampled from the data in each iteration, $c^i \hookleftarrow P(c|d, f^{sync, free, dust}, \theta^i)$ (Wandelt et al. 2004). Alternatively, component separation techniques could be used to take foreground contaminants into account without the need to rely on a priori defined templates (Eriksen et al. 2006). The traditional approach to deal with point sources is to mask affected regions of the sky to exclude them from the analysis. Discrete object detection has been demonstrated to be possible within a Bayesian framework (Hobson & McLachlan 2003; Carvalho et al. 2009), and can be fully included into the sampling chain. However, as sources are only successfully detected down to an experiment-specific flux limit, a residue-free removal of their contribution is in general not possible.

As the angular resolution of sky maps produced by existing CMB experiments like WMAP is high and will further increase once data of the Planck satellite mission becomes available, computational feasibility of an analysis tool is an issue. The speed of our method in a full implementation is limited by harmonic transforms which scale as $\mathcal{O}(N_{pix}^{3/2})$ and are needed to calculate the primordial perturbations at numerous shells at distances from the cosmic horizon to zero. Thus, it shows the same scaling relation as fast cubic

---

[1]E.g. as described in Lewis & Bridle (2002)

72

estimators (Komatsu et al. 2005; Yadav et al. 2007), albeit with a larger prefactor.

3.4 Implementation and Discussion

To verify our results and demonstrate the applicability of the method, we implemented a simple 1-D toy model. We considered a vector Φ_{L} of random numbers generated from a heptadiagonal covariance matrix with elements

$$
P_\Phi = \begin{pmatrix} & & & \ddots & & & & & \\ \ldots\, 0 & 0.1 & 0.2 & 0.5 & 1.0 & 0.5 & 0.2 & 0.1 & 0 \ldots \\ & & & & \ddots & & & & \end{pmatrix} \times 10^{-10}. \quad (3.18)
$$

Then, a data vector with weak non-Gaussianity according to Eq. 3.2 was produced and superimposed with Gaussian white noise. Constructed in this way, it is of the order $\mathcal{O}(10^{-5})$, thus the amplitude of the resulting signal s is comparable to CMB anisotropies.

The data vector had a length of 10^6 pixels; for simplicity, we set the beam function B and the linear transformation matrix M to unity. This setup allows a brute force implementation of all equations at a sufficient computational speed. We define the signal-to-noise ratio (S/N) per pixel as the standard deviation of the input signal divided by the standard deviation of the additive noise. It was chosen in the range 0.5-10 to model the typical S/N per pixel of most CMB experiments. To reconstruct the signal, we draw 1000 samples according to the scheme in Eq. 3.16.

Whereas the Φ_{NL} can be generated directly from a simple Gaussian distribution with known mean and variance, the construction of the f_{NL} is slightly more complex. For each Φ_{NL}, we ran a Metropolis Hastings algorithm with symmetric Gaussian proposal density with a width comparable to that of the target density and started the chain at $f_{\mathrm{NL}} = 0$. We run the f_{NL} chain to convergence. We ensured that after ten accepted steps the sampler has decorrelated from the starting point. Our tests conducted with several chains run in parallel give $1 < R < 1.01$, where R is the convergence statistic proposed by Gelman & Rubin (1992). We record the last element of the chain as the new f_{NL} sample.

Finally, we compared the obtained sets of values $\{\Phi_{\mathrm{NL}}^i\}$, $\{f_{\mathrm{NL}}^i\}$ to the initial data. An example is shown in Fig. 3.1, where we illustrate the reconstruction of a given potential Φ_{NL} for different signal-to-noise ratios per

pixel. The $1-\sigma$ error bounds are calculated from the 16 % and 84 % quantile of the generated sample. Typical posterior densities for f_{NL} as derived from the samples can be seen in Fig. 3.2. We considered the cases $f_{\mathrm{NL}} = 0$ and $f_{\mathrm{NL}} = 200$ with $S/N = 10$ per pixel and show the distributions generated from 1000 draws. The derived posterior densities possesses a mean value of $f_{\mathrm{NL}} = 6 \pm 40$ and $f_{\mathrm{NL}} = 201 \pm 40$, respectively. The width of the posterior is determined by both the shape of the conditional PDF of f_{NL} for a given Φ_{NL} and the shift of this distribution for different draws of Φ_{NL} (Fig. 3.3). The analysis of several data sets indicate that the approximation does not bias the posterior density if the data are decisive. We illustrate this issue in the left panel of Fig. 3.4, where we show the distribution of the mean values $\langle f_{\mathrm{NL}} \rangle$ of the posterior density constructed from 100 independent simulations. For an input value of $f_{\mathrm{NL}} = 200$ we derive a mean value $\langle f_{\mathrm{NL}} \rangle = 199.3 \pm 34.8$ and conclude that our sampler is unbiased for these input parameters. For a high noise level, however, the Φ_{NL} can always be sampled such that they are purely Gaussian fields and thus the resulting PDF for f_{NL} is then shifted towards $f_{\mathrm{NL}} = 0$. This behavior is demonstrated in Fig. 3.5 where we compare the constructed posterior density for the cases $S/N = 10$ and $S/N = 0.5$ per pixel. If the noise level becomes high, the approximated prior distribution dominates and leads to both, a systematic displacement and an artificially reduced width of the posterior. Therefore, the sampler constructed here is conservative in a sense that it will tend to underpredict the value of f_{NL} if the data are ambiguous.

An example of the evolution of the drawn f_{NL} samples with time can be seen in Fig. 3.6, where we in addition show the corresponding autocorrelation function as defined via

$$\xi(\Delta N) = \frac{1}{N} \sum_i^N \frac{(f_{\mathrm{NL}}^i - \mu) \cdot (f_{\mathrm{NL}}^{i+\Delta N} - \mu)}{\sigma^2} \, , \tag{3.19}$$

where N is the length of the generated f_{NL} chain with mean μ and variance σ^2. The uncorrelated samples of f_{NL} ensure an excellent mixing of the chain resulting in a fast convergence rate.

3.5   Optimality

In a frequentist analysis, parameter inference corresponds to finding an estimator that enables to compute the most probable value of the quantity

of interest as well as a bound for the error. Ideally, the estimator is unbiased and optimal, i.e. it's expectation value coincides with the true value of the parameter and the error satisfies the Cramer-Rao bound. Contrary, in a Bayesian approach, one calculates the full probability distribution of the parameter directly. Strictly speaking, optimality is therefore an ill-defined term within the Bayesian framework. All we have to show is that the approximation adopted in Eq. 3.11 does not affect the outcome of the calculation significantly. Note that the simplification corresponds to imposing the prior of a purely Gaussian data set. In the case of the CMB, this is a very reasonable assumption because up to now no detection of $f_{\rm NL}$ has been reported.

To investigate the effects of the approximation, we checked the dependence of the width of the posterior distribution on $f_{\rm NL}$ by running a set of simulations with varying input values $f_{\rm NL} = 0$, 50, 100, 150, 200, 250. The estimated standard deviation $\sigma_{f_{\rm NL}}$ of the drawn $f_{\rm NL}$ samples, each averaged over 10 simulation runs, are depicted in the right panel of Fig. 3.4. Contrary to the KSW estimator that shows an increase of $\sigma_{f_{\rm NL}}$ with $f_{\rm NL}$, we find no such indication of sub-optimal behavior in the relevant region of small non-Gaussianity. In particular, as the width of the distribution stays constant in the limit $f_{\rm NL} \to 0$ where our approximated equations evolve into the exact expressions, we conclude that the adopted simplification does not affect the result significantly.

This finding can also be interpreted from a different point of view: It is possible to define a frequentist estimator for $f_{\rm NL}$ based on the mean of the posterior distribution. Our results indicate that such an estimator is unbiased in the high signal-to-noise regime.

We apply an additional test in the next section where we compare our sampling algorithm to a slower but exact scheme.

3.6 Hamiltonian Monte Carlo sampling

In addition to the sampling technique presented above, we tested whether an exact Hamiltonian Monte Carlo (HMC) sampler is applicable to the problem. Within this approach one uses the methods developed in classical mechanics to describe the motion of particles in potentials. The quantity of interest is regarded as the spatial coordinate of a particle and the potential well corresponds to the PDF to evaluate (Duane et al. 1987). To each variable $(f_{\rm NL}, \Phi_{\rm L,1}, \ldots, \Phi_{\rm L,n})$, a mass and a momentum is assigned and the system
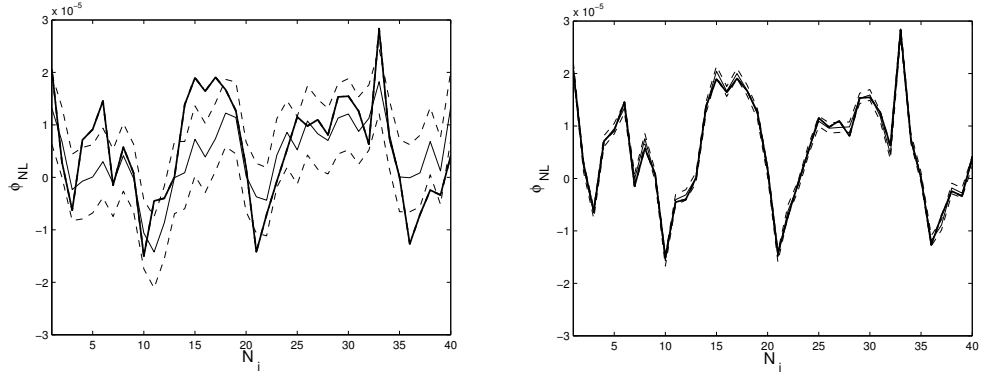
Figure 3.1: Examples of reconstructed potentials Φ_{NL}. *Left panel:* The input parameters for the calculation were $f_{\mathrm{NL}} = 200$ and $S/N = 1$. *Right panel:* Analysis of the same data set for a signal-to-noise ratio of $S/N = 10$. For clarity, we show only 40 elements of the Φ_{NL}-vector (*thick solid line*) and its reconstruction (*thin solid line*) as well as the $1 - \sigma$ error bounds (*dashed lines*). As the difference between Φ_{NL} and the linear potential Φ_{L} is very small, Φ_{L} can not be distinguished from Φ_{NL} in this plot. In both cases 1000 samples were drawn.
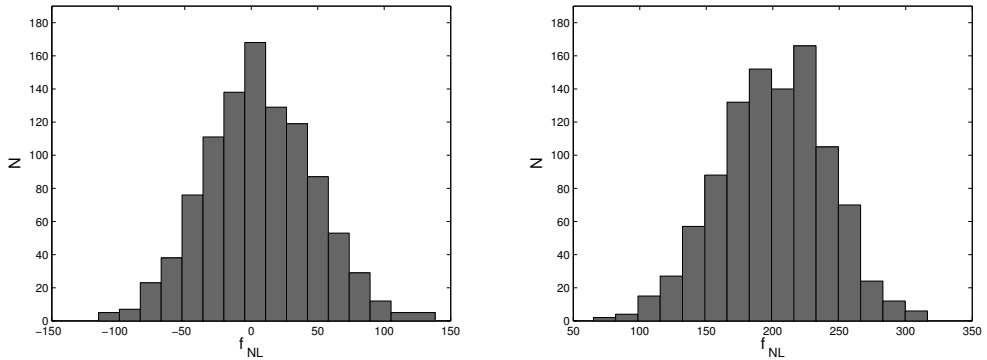

Figure 3.2: Examples of a constructed posterior distribution for f_{NL}. The input parameters used in this runs were $N_{pix} = 10^6$, $S/N = 10$ and $f_{\mathrm{NL}} = 0$ (*left panel*) or $f_{\mathrm{NL}} = 200$ (*right panel*). For each parameter combination 1000 samples were drawn.
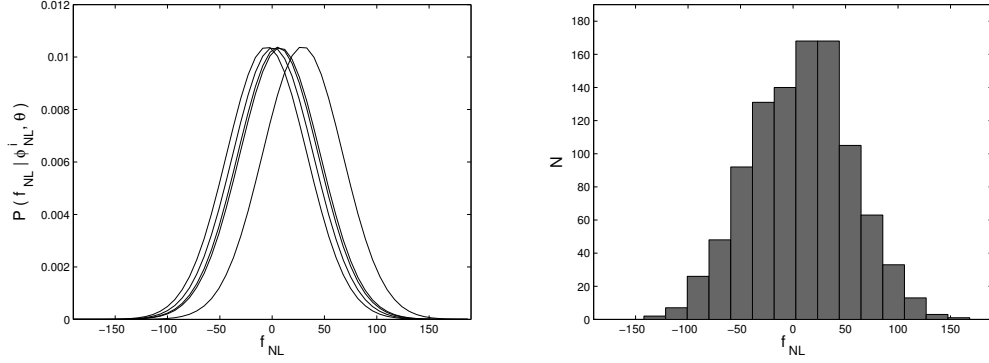
Figure 3.3: Build-up of the posterior distribution of f_{NL}. We depict the conditional probability distributions $P(f_{\mathrm{NL}}|\Phi_{\mathrm{NL}}, \theta)$ for several realizations of Φ_{NL} (*left panel*) and the constructed posterior after 1000 drawn samples (*right panel*). The input parameters were chosen to be $N_{pix} = 10^6$, $f_{\mathrm{NL}} = 0$, and $S/N = 2$.

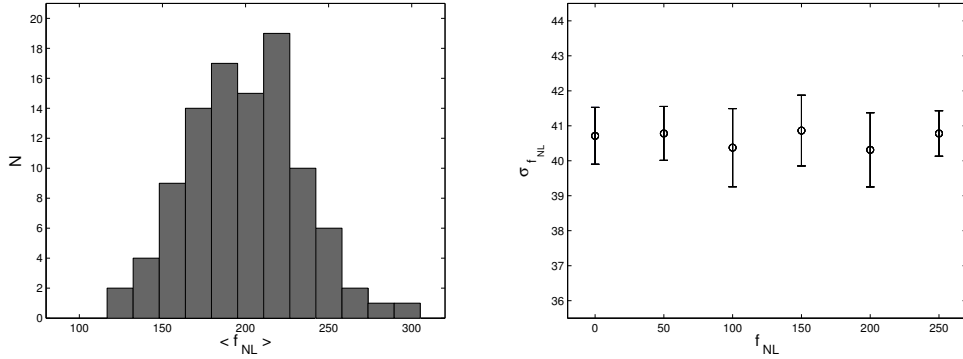Figure 3.4: Properties of the sampler. *Left panel:* Shown is the distribution of the derived mean values of f_{NL} from 100 simulations for a fiducial value of $f_{\mathrm{NL}} = 200$. *Right panel:* We display the estimated standard deviation $\sigma_{f_{\mathrm{NL}}}$ of the drawn f_{NL} samples as a function of f_{NL}. Each data point is averaged over 10 simulations. The input parameters used in this runs were $N_{pix} = 10^6$ and $S/N = 10$, in each simulation 1000 samples were drawn.
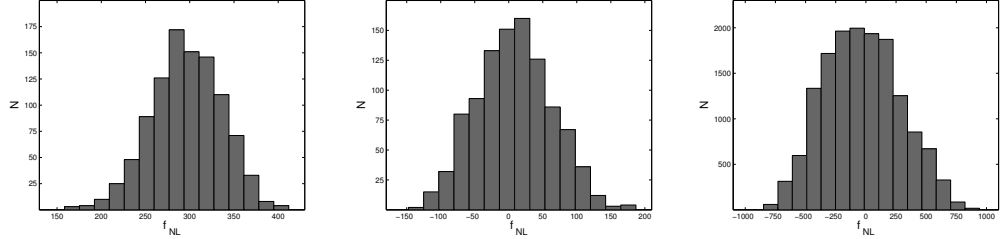
Figure 3.5: Impact of the signal-to-noise ratio on the approximate sampling scheme. *Left panel:* Example of a constructed posterior distribution for $S/N = 10$. *Middle panel:* Analysis of the same data set, but for $S/N = 0.5$. At high noise level, the distribution becomes too narrow and systematically shifted towards $f_{\mathrm{NL}} = 0$. *Right panel:* For comparison, we show the analysis of the data set at $S/N = 0.5$ using exact Hamiltonian Monte Carlo sampling. As input parameters, we used $f_{\mathrm{NL}} = 300$ and $N_{pix} = 10^6$. For the approximate and exact analysis, 1000 and 15 000 samples were drawn, respectively.
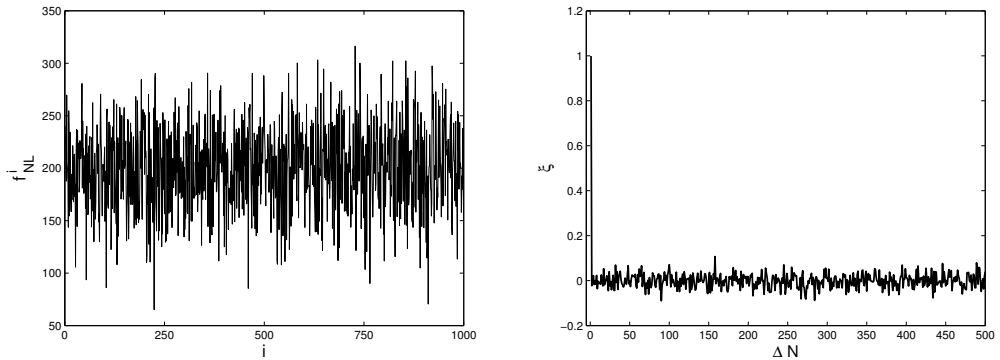

Figure 3.6: Example f_{NL} chain. *Left panel:* We display the chain of 1000 generated f_{NL} samples which built up the histogram plotted on the right hand side in Fig. 3.2. *Right panel:* The autocorrelation function of f_{NL} confirms the uncorrelatedness of the samples.

is evolved deterministically from a starting point according to the Hamilton equations of motion.

The applicability of HMC sampling techniques to cosmological parameter estimation has been demonstrated in Hajian (2007), and the authors of Taylor et al. (2008) compared HMC with Gibbs sampling for CMB power spectrum analysis. To apply HMC sampling to f_{NL} inference, we deduced the expression of the Hamiltonian

$$H = \sum_i \frac{p_i^2}{2\, m_i} - \log[P(d, \Phi_{\mathrm{L}}, f_{\mathrm{NL}}, \theta)] \,, \tag{3.20}$$

where the potential is related to the PDF as defined in Eq. 3.8. The Hamilton equations of motion,

$$\begin{aligned}
\frac{\mathrm{d}x_i}{\mathrm{d}t} &= \frac{\partial H}{\partial p_i} \,, \\
\frac{\mathrm{d}p_i}{\mathrm{d}t} &= -\frac{\partial H}{\partial x_i} = \frac{\partial \log[P(d, \Phi_{\mathrm{L}}, f_{\mathrm{NL}}, \theta)]}{\partial x_i} \,,
\end{aligned} \tag{3.21}$$

are integrated for each parameter $\{x_i;\ p_i\} = \{f_{\mathrm{NL}},\ \Phi_{\mathrm{L}};\ p_{f_{\mathrm{NL}}},\ p_{\Phi_{\mathrm{L}}}\}$ using the leapfrog method with step size δt,

$$\begin{aligned}
p_i(t + \frac{\delta t}{2}) &= p_i(t) + \frac{\delta t}{2} \left.\frac{\partial \log[P(d, \Phi_{\mathrm{L}}, f_{\mathrm{NL}}, \theta)]}{\partial x_i}\right|_{x(t)} \\
x_i(t + \delta t) &= x_i(t) + \frac{\delta t}{m_i} p_i(t + \frac{\delta t}{2}) \\
p_i(t + \delta t) &= p_i(t + \frac{\delta t}{2}) + \frac{\delta t}{2} \left.\frac{\partial \log[P(d, \Phi_{\mathrm{L}}, f_{\mathrm{NL}}, \theta)]}{\partial x_i}\right|_{x(t+\delta t)} \,.
\end{aligned} \tag{3.22}$$

The equations of motion for x_i are straightforward to compute, as they only depend on the momentum variable. To integrate the evolution equations for the p_i, we derive

$$\begin{aligned}
\frac{\partial \log[P(d, \Phi_{\mathrm{L}}, f_{\mathrm{NL}}, \theta)]}{\partial f_{\mathrm{NL}}} &= (\Phi_{\mathrm{L}}^2 - \langle \Phi_{\mathrm{L}}^2 \rangle)^\dagger M^\dagger B^\dagger N^{-1} \\
&\quad \times (d - BM\Phi_{\mathrm{L}} - f_{\mathrm{NL}} BM(\Phi_{\mathrm{L}}^2 - \langle \Phi_{\mathrm{L}}^2 \rangle)) \,, \\
\frac{\partial \log[P(d, \Phi_{\mathrm{L}}, f_{\mathrm{NL}}, \theta)]}{\partial \Phi_{\mathrm{L}}} &\approx M^\dagger B^\dagger N^{-1}(d - BM\Phi_{\mathrm{L}}) - P_\Phi^{-1}\Phi_{\mathrm{L}} \\
&\quad + 2f_{\mathrm{NL}} \operatorname{diag}(M^\dagger B^\dagger N^{-1} d)\Phi_{\mathrm{L}} + \mathcal{O}(\Phi_{\mathrm{L}}^2) \,, \tag{3.23}
\end{aligned}$$

where we have truncated the gradient in the latter equation at order $\mathcal{O}(\Phi_\mathrm{L}^2)$. The final point of the trajectory is accepted with probability p, calculated from $p = \min(1, \exp[-\Delta H])$, where ΔH is the difference in energy between the end- and starting point. This accept/reject step allows us to restore exactness as it eliminates the error introduced by approximating the gradient in Eq. 3.23 and by the numerical integration scheme. In general, only accurate integrations where ΔH is close to zero result in high acceptance rates. Furthermore, the efficiency of a HMC sampler is sensitive to the choice of the free parameters m_i, which corresponds to a mass. This issue is of particular importance if the quantities of interest possess variances varying by orders of magnitude. Following Taylor et al. (2008), we chose the masses inversely proportional to the diagonal elements of the covariance matrix which we reconstructed out of the solution of the sampling scheme from Sect. 3.3. We initialized the algorithm by performing one draw of Φ_NL from the conditional PDF $P(\Phi_\mathrm{NL}|d, \theta)$ and setting $f_\mathrm{NL} = 0$. The outcome of repeated analyses of the data set presented in Fig. 3.3 is shown in Fig. 3.7. The consistency of the distributions confirms the equivalence of the two sampling techniques in the high signal-to-noise regime. However, convergence for the HMC is far slower, even for the idealized choice for m_i and a reasonable starting guess, as can be seen from the large width of the autocorrelation function (see right panel of Fig. 3.7).

We conclude, therefore, that the direct sampling scheme presented in Sect. 3.3 is more efficient than HMC when applied to the detection of local non-Gaussianities in the high signal-to-noise regime. However, as shown in the rightmost panel of Fig. 3.5, the exact analysis using a HMC algorithm remains applicable at high noise level.

3.7 Extension to realistic data

Applying the method to a realistic CMB data set requires recovering the primordial potential Φ_L on shells at numerous distances r_i from the origin to the present time cosmic horizon. Thus, the product of the transfer matrix M with the potential transforms to

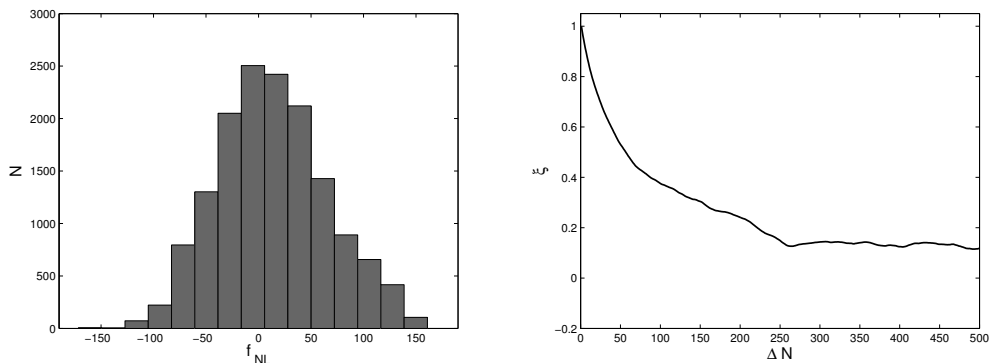$$M\Phi \rightarrow \sum_i M_i \Phi(r_i)\,. \tag{3.24}$$

Figure 3.7: Performance of the Hamiltonian Monte Carlo sampler. *Left panel*: Analysis of the data set of Fig. 3.3 using the HMC sampler. Here, 15 000 samples were draw. *Right panel*: The autocorrelation function of f_{NL}.

Here, the matrix M projects a weighted combination of the $\Phi(r_i)$ at different radii to a resulting two dimensional signal map s. The resolution of the r-grid can be coarser where the transfer functions for radiation are close to zero and must be finer at the distances of recombination and reionization. Another modification concerns the covariance matrix P_Φ of the potential. Now it additionally describes the correlation of Φ on distinct shells at different distances,

$$\Phi^\dagger P_\Phi^{-1} \Phi \rightarrow \sum_{i,j} \Phi(r_i) P_{\Phi(r_i),\Phi(r_j)}^{-1} \Phi(r_j)\,, \qquad (3.25)$$

and can be calculated from the primordial power spectrum $\mathcal{P}(k)$ predicted by inflation

$$P_{\Phi(r_i),\Phi(r_j)\,\ell} = \frac{2}{\pi} \int k^2 dk\, \mathcal{P}(k)\, j_\ell(k\,r_1)\, j_\ell(k\,r_2)\,. \qquad (3.26)$$

To tighten the constraints on Φ, polarization information can be included into the analysis as well simply by replacing the temperature by the polarization transfer function in the expression for M. We plan to study the application of our methods to realistic CMB data in a future publication.

The computational speed of a complete implementation is limited by harmonic transforms that scale as $\mathcal{O}(N_{pix}^{3/2})$.

3.8   Summary

In this paper, we developed two methods to infer the amplitude of the non-Gaussianity parameter f_{NL} from a data set within a Bayesian approach. We focused on the so called local type of non-Gaussianity and derived an expression for the joint probability distribution of f_{NL} and the primordial curvature perturbations, Φ. Despite the methods are of general validity, we tailored our discussion to the case example of CMB data analysis.

We developed an exact Markov Chain sampler that generates correlated samples from the joint density using the Hamiltonian Monte Carlo approach. We implemented the HMC sampler and applied it to a toy model consisting of simulated measurements of a 1-D sky. These simulations demonstrate that the recovered posterior distribution is consistent with the level of simulated non-Gaussianity.

With two approximations that exploit the fact that the non-Gaussian contribution to the signal is next order in perturbation theory, we find a far more computationally efficient Monte Carlo sampling algorithm that produces *independent* samples from the f_{NL} posterior. The regime of applicability for this approximation is for data with high signal-to-noise and weak non-Gaussianity.

By comparison to the exact HMC sampler, we show that our approximate algorithm reproduces the posterior location and shape in its regime of applicability. If non-zero f_{NL} is not supported by the data the method is biased towards Gaussianity. The approximate posterior more strongly prefers zero f_{NL} compared to non-zero values than the exact posterior, as expected given the nature of the approximations which Gaussianize the prior. This method is therefore only applicable if the data contains sufficient support for the presence of non-Gaussianity essentially overruling the preference for Gaussianity in our approximate prior.

Our efficient method enables us to perform a Monte Carlo study of the behavior of the posterior density for our toy model data with high signal-to-noise per pixel. We found that the width of the posterior distribution does not change as a function of the level of non-Gaussianity in the data, contrary to the frequentist estimator where there is an additional, f_{NL} dependent, variance component (Creminelli et al. 2007; Liguori et al. 2007). Our results suggest that this may be an advantage of the Bayesian approach compared to the frequentist approach, motivating further study of the application of

Bayesian statistics to the search for primordial local non-Gaussianity in current and future CMB data.

We close on a somewhat philosophical remark. Even though we chose a Gaussian prior approximation for expediency, it may actually be an accurate model of prior belief for many cosmologists since canonical theoretical models predict Gaussian perturbations. From that perspective our fast, approximate method may offer some (philosophically interesting) insight into the question "what level of signal-to-noise in the data is required to convince someone of the presence of non-Gaussianity whose prior belief is that the primordial perturbations are Gaussian?"

Bibliography

Acquaviva, V., Bartolo, N., Matarrese, S., & Riotto, A. 2003, Nuclear Physics B, 667, 119

Alishahiha, M., Silverstein, E., & Tong, D. 2004, Phys. Rev. D, 70, 123505

Babich, D. 2005, Phys. Rev. D, 72, 043003

Babich, D., Creminelli, P., & Zaldarriaga, M. 2004, J. Cosmology Astropart. Phys., 8, 9

Bartolo, N., Komatsu, E., Matarrese, S., & Riotto, A. 2004, Phys. Rep., 402, 103

Bean, R., Dunkley, J., & Pierpaoli, E. 2006, Phys. Rev. D, 74, 063503

Bond, J. R., Jaffe, A. H., & Knox, L. 1998, Phys. Rev. D, 57, 2117

Carvalho, P., Rocha, G., & Hobson, M. P. 2009, MNRAS, 393, 681

Creminelli, P., Nicolis, A., Senatore, L., Tegmark, M., & Zaldarriaga, M. 2006, J. Cosmology Astropart. Phys., 5, 4

Creminelli, P., Senatore, L., & Zaldarriaga, M. 2007, J. Cosmology Astropart. Phys., 3, 19

Duane, S., Kennedy, A. D., J., P. B., & D., R. 1987, Physics Letters B, 195, 216

Elsner, F. & Wandelt, B. D. 2009, ApJS, 184, 264

Enqvist, K. & Sloth, M. S. 2002, Nuclear Physics B, 626, 395

Eriksen, H. K., Dickinson, C., Jewell, J. B., et al. 2008, ApJ, 672, L87

Eriksen, H. K., Dickinson, C., Lawrence, C. R., et al. 2006, ApJ, 641, 665

Gelman, A. & Rubin, D. B. 1992, Statistical Science, 7, 457

Guth, A. H. 1981, Phys. Rev. D, 23, 347

Hajian, A. 2007, Phys. Rev. D, 75, 083525

Hinshaw, G., Weiland, J. L., Hill, R. S., et al. 2009, ApJS, 180, 225

Hobson, M. P. & McLachlan, C. 2003, MNRAS, 338, 765

Jewell, J., Levin, S., & Anderson, C. H. 2004, ApJ, 609, 1

Khoury, J., Ovrut, B. A., Steinhardt, P. J., & Turok, N. 2001, Phys. Rev. D, 64, 123522

Komatsu, E. & Spergel, D. N. 2001, Phys. Rev. D, 63, 063002

Komatsu, E., Spergel, D. N., & Wandelt, B. D. 2005, ApJ, 634, 14

Lewis, A. & Bridle, S. 2002, Phys. Rev. D, 66, 103511

Liguori, M., Yadav, A., Hansen, F. K., et al. 2007, Phys. Rev. D, 76, 105016

Linde, A. D. 1982, Physics Letters B, 108, 389

Lyth, D. H., Ungarelli, C., & Wands, D. 2003, Phys. Rev. D, 67, 023503

84

Maldacena, J. 2003, Journal of High Energy Physics, 5, 13

Moroi, T. & Takahashi, T. 2001, Physics Letters B, 522, 215

Senatore, L. 2005, Phys. Rev. D, 71, 043512

Smith, K. M., Senatore, L., & Zaldarriaga, M. 2009, J. Cosmology Astropart. Phys., 9, 6

Spergel, D. N., Bean, R., Doré, O., et al. 2007, ApJS, 170, 377

Steinhardt, P. J. & Turok, N. 2002, Phys. Rev. D, 65, 126003

Taylor, J. F., Ashdown, M. A. J., & Hobson, M. P. 2008, MNRAS, 389, 1284

Tegmark, M. 1997, Phys. Rev. D, 55, 5895

Trotta, R. 2007, MNRAS, 375, L26

Verde, L., Wang, L., Heavens, A. F., & Kamionkowski, M. 2000, MNRAS, 313, 141

Wandelt, B. D., Larson, D. L., & Lakshminarayanan, A. 2004, Phys. Rev. D, 70, 083511

Yadav, A. P. & Wandelt, B. D. 2005, Phys. Rev. D, 71, 123004

Yadav, A. P. S., Komatsu, E., & Wandelt, B. D. 2007, ApJ, 664, 680

Chapter 4

Local non-Gaussianity in the Cosmic Microwave Background the Bayesian way

Franz Elsner[1], and Benjamin D. Wandelt[2,3]

[1]Max-Planck-Institut für Astrophysik, Karl-Schwarzschild-Straße 1, 85748 Garching, Germany

[2]UPMC Univ Paris 06, Institut d'Astrophysique de Paris, 98 bis, blvd Arago, 75014 Paris, France

[3]Department of Physics, University of Illinois at Urbana-Champaign, 1110 W. Green Street, Urbana, IL 61801, USA

Abstract

We introduce an exact Bayesian approach to search for non-Gaussianity of local type in Cosmic Microwave Background (CMB) radiation data. Using simulated CMB temperature maps, the newly developed technique is compared against the conventional frequentist bispectrum estimator. Starting from the joint probability distribution, we obtain analytic expressions for the conditional probabilities of the primordial perturbations given the data, and for the level of non-Gaussianity, f_{NL}, given the data and the perturbations. We propose Hamiltonian Monte Carlo sampling as a means to derive realizations of the primordial fluctuations from which we in turn sample f_{NL}. Although being computationally expensive, this approach allows us to exactly construct the full target posterior probability distribution. When compared to the frequentist estimator, applying the Bayesian method to Gaussian CMB maps provides consistent results. For the analysis of non-Gaussian maps, however, the error bars on f_{NL} do not show excess variance within the Bayesian framework. This finding is of particular relevance in the light of upcoming high precision CMB measurements obtained by the Planck satellite mission.

4.1 Introduction

Precise measurements of the cosmic microwave background (CMB) radiation have vastly improved our understanding of cosmology and played a crucial role in constraining the set of fundamental cosmological parameters (Spergel et al. 2003, 2007; Hinshaw et al. 2009; Larson et al. 2010). This success is based on a tight connection between the temperature fluctuations we observe today and the physical processes taking place in the early universe.

Inflation is currently the favored theory predicting the shape of primordial perturbations (Guth 1981; Albrecht & Steinhardt 1982; Linde 1982; Starobinskiĭ 1982). In its simplest form, it is driven by a single scalar field in ground state with quadratic kinetic term that rolled down a flat potential slowly. This configuration leads to very small non-Gaussianities (see Acquaviva et al. 2003; Maldacena 2003 for a first order, and Pitrou et al. 2010 for the full second order calculation). Hence, a clear detection of an excess of primordial non-Gaussianity would allow us to rule out the simplest models. Together with constraints on the scalar spectral index n_S and the search for primordial gravitational waves, the test for non-Gaussianity therefore becomes another important means to probe the physical processes of the early universe.

In this paper, we focus on non-Gaussianity of local type, where the amplitude of non-Gaussianity is measured by a single parameter, f_{NL} (Salopek & Bond 1990). A common strategy for estimating f_{NL} is to evaluate the bispectrum of the CMB (Komatsu et al. 2002, 2003; Spergel et al. 2007; Yadav & Wandelt 2008; Smith et al. 2009). This is usually done indirectly via a cubic combination of filtered CMB maps reconstructing the primordial perturbations (Komatsu et al. 2005; Yadav et al. 2007, 2008). This approach takes advantage of the specific signatures produced by primordial non-Gaussianity, resulting in a computationally efficient algorithm. A variant of this estimator has been successfully applied to the 7-year data release of the Wilkinson Microwave Anisotropy Probe (WMAP), resulting in $-10 < f_{\mathrm{NL}} < 74$ at $95\,\%$ confidence level (Komatsu et al. 2010).

The bispectrum estimator used in previous analyses has been shown to be optimal, i.e. it satisfies the Cramér-Rao bound (Babich 2005). However, this turns out to be true only in the limit of vanishing non-Gaussianity (Creminelli et al. 2007). For a significant detection of f_{NL}, the estimator suffers from excess variance, a finding that has also been verified numerically (Liguori et al.

2007). For the simplified case of a flat sky approximation, neglected transfer functions and instrumental noise, Creminelli et al. (2007) showed that it should be possible to construct an improved version of the estimator that is equivalent to a full likelihood analysis up to terms of the order $\mathcal{O}(1/\ln N_{\text{pix}})$.

Bayesian methods for the analysis of various aspects of CMB data have been successfully developed in the past, e.g., for an exact power spectrum determination using Gibbs sampling (e.g. Jewell et al. 2004; Wandelt et al. 2004; Larson et al. 2007; Jewell et al. 2009), to separate foreground contributions from the CMB anisotropies (e.g. Hobson et al. 1998; Barreiro et al. 2004; Eriksen et al. 2006, 2008a,b; Dickinson et al. 2009), or to probe for non-Gaussian features (e.g. Rocha et al. 2001; Enßlin et al. 2009; Vielva & Sanz 2009; Efstathiou et al. 2010). They offer a natural way to marginalize over uncertainties e.g. attributed to foreground contamination or instrumental effects. This is of particular importance for a reliable analysis of weak signals and an advantage over frequentist methods, where no such procedures exist. Here, we advance the exact scheme introduced in Elsner et al. (2010) to infer the level of non-Gaussianity from realistic CMB data within a Bayesian approach.

We use simulated Gaussian and non-Gaussian CMB temperature maps to compare and contrast the conventional frequentist (bispectrum) estimator with the exact Bayesian approach. We show that the latter method does not suffer from excess variance for non-zero f_{NL}, and can deal with partial sky coverage and anisotropic noise properties, a feature of particular importance for local non-Gaussianity and for any realistic experiment.

The paper is organized as follows. In Sect. 4.2, we briefly outline the theoretical model used to describe primordial non-Gaussianity. We review the conventional frequentist bispectrum estimator and present our exact Bayesian approach to infer the amplitude of non-Gaussianity in Sect. 4.3. Then, we use simulated maps to compare the performance of the newly developed technique to the traditional estimator (Sect. 4.4). We demonstrate the capability of the Bayesian scheme to deal with realistic CMB experiments in Sect. 4.5. Finally, we summarize our results in Sect. 4.6.

Throughout the paper, we assume the WMAP5+BAO+SNALL cosmological parameters (Komatsu et al. 2009): $\Omega_\Lambda = 0.721$, $\Omega_c h^2 = 0.1143$, $\Omega_b h^2 = 0.02256$, $\Delta_\mathcal{R}^2(0.002\ Mpc^{-1}) = 2.457 \cdot 10^{-9}$, $h = 0.701$, $n_s = 0.96$, and $\tau = 0.084$.

4.2 Model of non–Gaussianity

The multipole coefficients $a_{\ell m}$ of the CMB temperature anisotropies are related to the primordial fluctuations,

$$a_{\ell m} = \frac{2}{\pi} \int k^2 dk\, r^2 dr\, \Phi_{\ell m}(r)\, g_\ell(k)\, j_\ell(kr) + n_{\ell m}$$
$$\equiv M\Phi_{\ell m} + n_{\ell m}\,, \qquad\qquad (4.1)$$

where $\Phi_{\ell m}$ are the primordial adiabatic perturbations at comoving distance r, g_ℓ the transfer function in momentum space, and j_ℓ the spherical Bessel function of order ℓ. Additive noise is taken into account by $n_{\ell m}$, for a compact notation we will use the operator M as a shorthand for the radial integral in what follows. Traces of non-Gaussianity in the primordial fluctuations will be transferred to the multipole moments $a_{\ell m}$ according to Eq. 4.1, potentially making them accessible to CMB experiments.

We focus on non-Gaussianity of local type, which is realized to very good approximation in multi-field inflationary models as described by the curvaton model (Moroi & Takahashi 2001; Lyth et al. 2003), or in ekpyrotic/cyclic universe models (Khoury et al. 2001; Enqvist & Sloth 2002; Steinhardt & Turok 2002). Here, we can parametrize the non-Gaussianity of Φ via a quadratic dependency on a Gaussian auxiliary field Φ_L, that is local in real space, of the form (Salopek & Bond 1990; Gangui et al. 1994)

$$\Phi(r) = \Phi_L(r) + f_{NL}[\Phi_L^2(r) - \langle\Phi_L^2(r)\rangle] + \mathcal{O}(\Phi_L^3)\,, \qquad (4.2)$$

where f_{NL} is a dimensionless measure of the amplitude of non-Gaussianity and we truncate the expansion at third order in Φ_L.

4.3 Analysis techniques

4.3.1 Frequentist estimator

In the following, we briefly review the fast estimator as proposed by Komatsu et al. (2005). This estimator is optimal for uniform observation of the full sky. More general least-square cubic estimators have been found for data with partial sky coverage and anisotropic noise (Creminelli et al. 2006, see also the review of, e.g., Yadav & Wandelt 2010).

To estimate the non-Gaussianity of a CMB temperature map, one constructs the statistic $\mathcal{S}_{prim}$ out of a cubic combination of the data,

$$\mathcal{S}_{prim} = \int dr\, r^2 \int d^2\hat{n}\, A(r,\hat{n})\, B^2(r,\hat{n})\,. \tag{4.3}$$

The spatial integral runs over two filtered maps,

$$A(r,\hat{n}) = \sum_{\ell,m} \mathcal{C}_\ell^{-1}\, \alpha_\ell(r)\, a_{\ell m}\, Y_{\ell m}(\hat{n})\,, \tag{4.4}$$

$$B(r,\hat{n}) = \sum_{\ell,m} \mathcal{C}_\ell^{-1}\, \beta_\ell(r)\, a_{\ell m}\, Y_{\ell m}(\hat{n})\,, \tag{4.5}$$

that are constructed using the auxiliary functions

$$\alpha_\ell(r) = \frac{2}{\pi} \int dk\, k^2\, g_\ell(k)\, j_\ell(kr)\,, \tag{4.6}$$

$$\beta_\ell(r) = \frac{2}{\pi} \int dk\, k^2 \mathcal{P}(k)\, g_\ell(k)\, j_\ell(kr)\,, \tag{4.7}$$

and the inverse of the CMB plus noise power spectrum, $\mathcal{C}_\ell^{-1}$. The power spectrum of the primordial perturbations is denoted by $\mathcal{P}(k)$. Now, we can calculate the expectation value of f_{NL} from the statistics $\mathcal{S}_{prim}$ by applying a suitable normalization,

$$f_{\mathrm{NL}} = \left[\sum_{\ell_1 \le \ell_2 \le \ell_3} \frac{1}{\Delta_{\ell_1\ell_2\ell_3}} (B^{prim})^2_{\ell_1\ell_2\ell_3}\, \mathcal{C}_{\ell_1}^{-1}\, \mathcal{C}_{\ell_2}^{-1}\, \mathcal{C}_{\ell_3}^{-1} \right]^{-1} \cdot \mathcal{S}_{prim}\,, \tag{4.8}$$

where $\Delta_{\ell_1\ell_2\ell_3} = 6$, when $\ell_1 = \ell_2 = \ell_3$, 2, when $\ell_1 = \ell_2 \ne \ell_3$ or $\ell_1 \ne \ell_2 = \ell_3$, and 1 otherwise. The theoretical bispectrum for $f_{\mathrm{NL}} = 1$, $B^{prim}_{\ell_1\ell_2\ell_3}$, is given by

$$B^{prim}_{\ell_1\ell_2\ell_3} = 2\, I_{\ell_1\ell_2\ell_3} \int dr\, r^2\, [\beta_{\ell_1}(r)\beta_{\ell_2}(r)\alpha_{\ell_3}(r) + \beta_{\ell_3}(r)\beta_{\ell_1}(r)\alpha_{\ell_2}(r)$$
$$+ \beta_{\ell_2}(r)\beta_{\ell_3}(r)\alpha_{\ell_1}(r)]\,, \tag{4.9}$$

where a combinatorial prefactor is defined as

$$I_{\ell_1\ell_2\ell_3} = \sqrt{\frac{(2\ell_1+1)(2\ell_2+1)(2\ell_3+1)}{4\pi}} \begin{pmatrix} \ell_1 & \ell_2 & \ell_3 \\ 0 & 0 & 0 \end{pmatrix}\,. \tag{4.10}$$

Recently, the Bayesian counterpart of the fast estimator has been developed within the framework of information field theory by expanding the logarithm of the posterior probability to second order in f_{NL} (Enßlin et al. 2009). Here, the equivalent of the normalization factor in Eq. 4.8 becomes data dependent, accounting for the fact that the ability to constrain f_{NL} varies from data set to data set. We will go beyond this level of accuracy and present an exact Bayesian scheme in the next section.

4.3.2 Exact Bayesian inference

We now introduce a Bayesian method that, in contrast to the bispectrum estimator, includes information from *all* correlation orders. Our aim is to construct the posterior distribution of the amplitude of non-Gaussianities given the data, $P(f_{\mathrm{NL}}|d)$. To this end, we subsume the remaining set of cosmological parameters to a vector θ and rewrite the joint distribution as

$$P(d, \Phi_{\mathrm{L}}, f_{\mathrm{NL}}, \theta) = P(d|\Phi_{\mathrm{L}}, f_{\mathrm{NL}}, \theta)\, P(\Phi_{\mathrm{L}}|\theta)\, P(f_{\mathrm{NL}})\, P(\theta)\,. \qquad (4.11)$$

Substituting the noise vector in terms of data and signal, we can use Eq. 4.1 et seq. to express the probability for data d given Φ_{L}, f_{NL}, and θ up to an overall prefactor

$$P(d|\Phi_{\mathrm{L}}, f_{\mathrm{NL}}, \theta) \propto \mathrm{e}^{-1/2\,[d-M(\Phi_{\mathrm{L}}+f_{\mathrm{NL}}(\Phi_{\mathrm{L}}^2-\langle\Phi_{\mathrm{L}}^2\rangle))]^\dagger N^{-1}[d-M(\Phi_{\mathrm{L}}+f_{\mathrm{NL}}(\Phi_{\mathrm{L}}^2-\langle\Phi_{\mathrm{L}}^2\rangle))]}\,,$$
$$(4.12)$$

where we introduced the noise covariance matrix N. The prior probability $P(\Phi_{\mathrm{L}}|\theta)$ can be expressed as multivariate Gaussian distribution by construction, thus, we eventually obtain

$$P(d, \Phi_{\mathrm{L}}, f_{\mathrm{NL}}, \theta) \propto \exp\left\{-1/2\,\left[d - M(\Phi_{\mathrm{L}} + f_{\mathrm{NL}}(\Phi_{\mathrm{L}}^2 - \langle\Phi_{\mathrm{L}}^2\rangle))\right]^\dagger N^{-1}\right.$$
$$\left.\times\,\left[d - M(\Phi_{\mathrm{L}} + f_{\mathrm{NL}}(\Phi_{\mathrm{L}}^2 - \langle\Phi_{\mathrm{L}}^2\rangle))\right] - 1/2\,\Phi_{\mathrm{L}}^\dagger P_\Phi^{-1}\Phi_{\mathrm{L}} - f_{\mathrm{NL}}^2/2\sigma_{f_{\mathrm{NL}}}^2\right\} \quad (4.13)$$

as an exact expression for the joint distribution up to a normalization factor, assuming a Gaussian prior for f_{NL} with zero mean and variance $\sigma_{f_{\mathrm{NL}}}^2$, and a flat prior for the cosmological parameters. The covariance matrix P_Φ is constrained by the primordial power spectrum predicted by inflation, $\mathcal{P}(k)$, and given by (Liguori et al. 2003)

$$\left\langle \Phi_{\mathrm{L}\ \ell_1 m_1}(r_1)\, \Phi_{\mathrm{L}\ \ell_2 m_2}^*(r_2)\right\rangle = \frac{2}{\pi}\,\delta_{\ell_2}^{\ell_1}\,\delta_{m_2}^{m_1}\int dk\, k^2 \mathcal{P}(k)\, j_{\ell_1}(kr_1)\, j_{\ell_2}(kr_2)\,. \quad (4.14)$$

To evaluate the joint distribution (Eq. 4.13) directly would require to perform a numerical integration over a high dimensional parameter space. For realistic data sets this turns out to be impossible computationally. We pursue a different approach here. First, we note that the exponent in Eq. 4.13 is quadratic in f_{NL} and hence the conditional density $P(f_{\mathrm{NL}}|d, \Phi_{\mathrm{L}}, \theta)$ is Gaussian with mean and variance

$$\langle f_{\mathrm{NL}} \rangle = \langle (f_{\mathrm{NL}} - \langle f_{\mathrm{NL}} \rangle)^2 \rangle (\Phi_{\mathrm{L}}^2 - \langle \Phi_{\mathrm{L}}^2 \rangle)^\dagger M^\dagger N^{-1} (d - M\Phi_{\mathrm{L}})$$
$$\langle (f_{\mathrm{NL}} - \langle f_{\mathrm{NL}} \rangle)^2 \rangle = \left[(\Phi_{\mathrm{L}}^2 - \langle \Phi_{\mathrm{L}}^2 \rangle)^\dagger M^\dagger N^{-1} M (\Phi_{\mathrm{L}}^2 - \langle \Phi_{\mathrm{L}}^2 \rangle) + 1/\sigma_{f_{\mathrm{NL}}}^2 \right]^{-1} .$$
$$(4.15)$$

Thus, for any realization of Φ_{L}, Eqs. 4.15 permit us to calculate the distribution of f_{NL} given the data. Similarly, we can calculate the conditional probability $P(\Phi_{\mathrm{L}}|d, \theta)$ by analytically marginalizing Eq. 4.13 over f_{NL},

$$P(\Phi_{\mathrm{L}}|d, \theta) = \int df_{\mathrm{NL}} \, P(\Phi_{\mathrm{L}}, f_{\mathrm{NL}}|d, \theta)$$
$$\propto [\sigma_{f_{\mathrm{NL}}}^2 (\Phi_{\mathrm{L}}^2 - \langle \Phi_{\mathrm{L}}^2 \rangle)^\dagger M^\dagger N^{-1} M (\Phi_{\mathrm{L}}^2 - \langle \Phi_{\mathrm{L}}^2 \rangle) + 1]^{-1/2}$$
$$\times \, \mathrm{e}^{-1/2 \, (d - M\Phi_{\mathrm{L}})^\dagger \left[N^{-1} - \frac{\sigma_{f_{\mathrm{NL}}}^2 \, N^{-1} M (\Phi_{\mathrm{L}}^2 - \langle \Phi_{\mathrm{L}}^2 \rangle)(\Phi_{\mathrm{L}}^2 - \langle \Phi_{\mathrm{L}}^2 \rangle)^\dagger M^\dagger N^{-1}}{\sigma_{f_{\mathrm{NL}}}^2 (\Phi_{\mathrm{L}}^2 - \langle \Phi_{\mathrm{L}}^2 \rangle)^\dagger M^\dagger N^{-1} M (\Phi_{\mathrm{L}}^2 - \langle \Phi_{\mathrm{L}}^2 \rangle) + 1} \right]}$$
$$\times (d - M\Phi_{\mathrm{L}}) - 1/2 \, \Phi_{\mathrm{L}}^\dagger P_\Phi^{-1} \Phi_{\mathrm{L}} .$$
$$(4.16)$$

Now we can outline our approach to infer the level of non-Gaussianity from CMB data iteratively. First, for given data d, we draw Φ_{L} from the distribution Eq. 4.16. Then, f_{NL} can be sampled according to Eqs. 4.15 using the value of Φ_{L} derived in the preceding step. If the sampling scheme is iterated for a sufficient amount of cycles, the derived set of f_{NL} values resembles an unbiased representation of the posterior distribution $P(f_{\mathrm{NL}}|d, \theta)$.

Unfortunately, there exists no known way to draw uncorrelated samples of Φ_{L} from its non-Gaussian distribution function directly. Here, we propose Hamiltonian Monte Carlo (HMC) sampling to obtain correlated realizations of the primordial perturbations. In this approach, the variable is regarded as the spatial coordinate of a particle moving in a potential well described by the probability distribution function to evaluate (Duane et al. 1987). A generalized mass matrix W and momentum variables p are assigned to the system to define its Hamiltonian

$$H = 1/2 \, p^\dagger W^{-1} p - \log[P(\Phi_{\mathrm{L}}|d, \theta)] , \quad\quad\quad (4.17)$$

where the potential is related to the posterior distribution as defined in Eq. 4.16. The system is evolved deterministically from a starting point according to the Hamilton's equations of motion

$$\frac{d\Phi_L}{dt} = \frac{\partial H}{\partial p},$$
$$\frac{dp}{dt} = -\frac{\partial H}{\partial \Phi_L} = \frac{\partial \log[P(\Phi_L | d, \theta)]}{\partial \Phi_L}, \tag{4.18}$$

which are integrated by means of the second order leapfrog scheme with step size δt,

$$p(t + \frac{\delta t}{2}) = p(t) + \frac{\delta t}{2} \left. \frac{\partial \log[P(\Phi_L | d, \theta)]}{\partial \Phi_L} \right|_{\Phi_L(t)}$$

$$\Phi_L(t + \delta t) = \Phi_L(t) + \delta t \, W^{-1} p(t + \frac{\delta t}{2})$$

$$p(t + \delta t) = p(t + \frac{\delta t}{2}) + \frac{\delta t}{2} \left. \frac{\partial \log[P(\Phi_L | d, \theta)]}{\partial \Phi_L} \right|_{\Phi_L(t + \delta t)}. \tag{4.19}$$

The equation of motion for Φ_L can easily be solved, as it only depends on the momentum variable. To integrate the evolution equation for p, we derive

$$\frac{\partial \log[P(\Phi_L | d, \theta)]}{\partial \Phi_L} \approx M^\dagger \left[N^{-1} \right.$$
$$\left. - \frac{\sigma_{f_{NL}}^2 N^{-1} M(\Phi_L^2 - \langle \Phi_L^2 \rangle)(\Phi_L^2 - \langle \Phi_L^2 \rangle)^\dagger M^\dagger N^{-1}}{\sigma_{f_{NL}}^2 (\Phi_L^2 - \langle \Phi_L^2 \rangle)^\dagger M^\dagger N^{-1} M(\Phi_L^2 - \langle \Phi_L^2 \rangle) + 1} \right] (d - M\Phi_L) - P_\Phi^{-1} \Phi_L \tag{4.20}$$

as an approximate expression neglecting higher order terms in Φ_L. The final point of the trajectory is accepted with probability $p = \min(1, \exp[-\Delta H])$, where ΔH is the difference in energy between the end- and starting point. This accept/reject step allows us to restore exactness as it eliminates the error introduced by approximating the gradient in Eq. 4.20 and by the numerical integration scheme. In general, only accurate integrations where ΔH is close to zero result in high acceptance rates. This can usually be archived by choosing small time steps or an accurate numerical integration scheme. However, as the time integration requires the calculation of spherical harmonic transforms with inherently limited precision, higher order methods

turn out to be unrewarding. Furthermore, the efficiency of a HMC sampler is sensitive to the choice of the mass matrix W. In agreement with Taylor et al. (2008), we found best performance when choosing W as inverse of the posterior covariance matrix of the primordial perturbations, which we derive from the Wiener filter equation for purely Gaussian perturbations to good approximation,

$$P(d, \Phi^G, \theta) \propto \exp \left\{ -1/2 \left[d - M\Phi^G \right]^\dagger N^{-1} \left[d - M\Phi^G \right] - 1/2\, \Phi^{G\dagger} P_\Phi^{-1} \Phi^G \right\},$$

(4.21)

with mean and variance of the distribution $P(\Phi^G | d, \theta)$

$$\langle \Phi^G \rangle = \langle (\Phi^G - \langle \Phi^G \rangle)^2 \rangle M^\dagger N^{-1} d$$

$$\langle (\Phi^G - \langle \Phi^G \rangle)^2 \rangle = \left[M^\dagger N^{-1} M - P_\Phi^{-1} \right]^{-1} ,\ \text{hence} \tag{4.22}$$

$$W = M^\dagger N^{-1} M - P_\Phi^{-1} . \tag{4.23}$$

For the calculation of the mass matrix W in the presence of anisotropic noise or partial sky coverage, we still adopt a simple power spectrum as approximation for N at the cost of a reduced sampling efficiency.

We initialize the algorithm by performing one draw of the primordial perturbations from the Gaussian posterior $P(\Phi^G | d, \theta)$ (Eqs. 4.22).

4.4 Scheme comparison

We use simulated CMB temperature maps obtained with the algorithm described in Elsner & Wandelt (2009) to compare the newly developed Bayesian scheme to the conventional frequentist approach. We chose a Gaussian ($f_{\mathrm{NL}} = 0$) and a non-Gaussian ($f_{\mathrm{NL}} = 100$) CMB realization at a HEALPix resolution of $n_{side} = 256$ and $\ell_{max} = 512$, superimposed by isotropic noise with a constant power spectrum amplitude of $\mathcal{C}_\ell^{noise} = 10^{-7}\mathrm{mK}^2$. We show the non-Gaussian temperature map besides the input signal and noise power spectra in Fig. 4.4.

Performing the analysis within the frequentist framework, we get $\langle f_{\mathrm{NL}} \rangle = 4$ for the Gaussian and $\langle f_{\mathrm{NL}} \rangle = 97$ for the non-Gaussian simulation. To obtain an estimate of the attributed error, we conducted 1000 Monte Carlo simulations with the input parameters as quoted above. For the Gaussian

realization, we find a standard deviation of $\sigma_{f_{\mathrm{NL}}}^{MC} = 15$, in perfect agreement with the value predicted form a fisher information matrix forecast. For the non-Gaussian simulation, however, the derived error $\sigma_{f_{\mathrm{NL}}}^{MC} = 20$ is already considerably larger than in the Gaussian case—the sub-optimality of the bispectrum estimator at non-zero f_{NL} becomes manifest.

In the Bayesian analysis, we construct the full posterior distribution out of the samples drawn from it. We chose a Gaussian prior for f_{NL} with zero mean and a very large width of $\sigma_{f_{\mathrm{NL}}}^{prior} = 500$ in order to not introduce any bias to the results. For an efficient sampling process, we tuned the time step size δt of the HMC algorithm to realize a mean acceptance rate of about $40\,\%$. To reduce the overall wall clock time needed for the analysis of one CMB map, we ran 32 chains in parallel and eventually combine all the samples. For reliable results, it is imperative to quantitatively assess the convergence of the Monte Carlo process. Here, we apply the statistics of Gelman & Rubin (1992) to the obtained samples. It compares the variance among different chains with the variance within a chain and returns a number in the range of $0 \leq R < \infty$ which reflects the quality of the convergence of the chains with a given length. In general, a value close to $R = 1$ reflects good convergence. As this value refers to the convergence of a single chain, we in fact obtain a significantly better result after a combination of all of the 32 independent chains we generated.

For the Gaussian simulation, we run chains with a length of $25\,000$ samples each, discarding the first 5000 samples during burn-in. With these parameters, we find excellent convergence as confirmed by the Gelman-Rubin statistics, $R = 1.04$. The final result along with a comparison to the frequentist scheme is shown in Fig. 4.2. In the Bayesian analysis, we find a mean value of $\langle f_{\mathrm{NL}} \rangle = 3$ and a width of the distribution $\sigma_{f_{\mathrm{NL}}} = 15$. As the bispectrum estimator is known to be optimal in the limit of vanishing non-Gaussianity, the two different approaches lead to consistent results.

To repeat the analysis of the non-Gaussian map, we again generated 32 independent chains with a length of $40\,000$ samples each. After dropping the first $10\,000$ elements to account for the period of burn-in, we estimated the convergence of the individual chains by means of the Gelman-Rubin statistics and find $R = 1.4$. The inferred mean of $\langle f_{\mathrm{NL}} \rangle = 99$ at an 1-σ error of $\sigma_{f_{\mathrm{NL}}} = 15$ is in good agreement with the input value of the simulation. We directly compare the Bayesian to the frequentist result in Fig. 4.3, where we now find an important difference in the outcomes. Whereas for a significant detection of non-Gaussianity the frequentist estimator suffers from excess

variance, the Bayesian scheme still provides the same error bars as for the Gaussian simulation.

We stress that the computational cost for the Bayesian analysis with the exact marginalization of the high-dimensional Φ parameter space is quite demanding. With the setup as described here, the runtime for the Gaussian and the non-Gaussian simulation amounts to about 80 000 CPUh and 150 000 CPUh, respectively. The reason for the inefficiency lies in the large correlation length of the f_{NL} sampling chains. We illustrate this fact in Fig. 4.4, where we display three out of the 32 chains of the non-Gaussian simulation. In addition, we show the autocorrelation function of a chain as defined via

$$\xi(\Delta N) = \frac{1}{N} \sum_i^N \frac{(f_{\mathrm{NL}}^i - \mu)(f_{\mathrm{NL}}^{i+\Delta N} - \mu)}{\sigma^2} \,, \qquad (4.24)$$

where N is the length of the f_{NL} chains with mean μ and variance σ^2.

It is interesting to note that the derived values of f_{NL} and their error bars will in general not agree exactly between the two approaches, even for a Gaussian data set. The frequentist estimator is unbiased with respect to all possible realizations of signal and noise. The error bars, calculated via Monte Carlo simulations, are the same for all data sets with identical input parameters by definition. The Bayesian approach, on the other hand, returns the entire information contained about the local model in the particular realization subject to the analysis. Thus, the uncertainty in the parameter is computed from the data itself and will vary from data set to data set, as cosmic variance or accidental alignments between signal and noise may impact the ability to constrain the level of non-Gaussianity. Furthermore, the Bayesian method constructs the full posterior probability function instead of simply providing an estimate of the error under the implicit assumption of a Gaussian distribution.

4.5   Application to more realistic simulations

In the previous section, we have demonstrated the Bayesian approach under idealized conditions such as isotropic noise properties and a full sky analysis. However, applying the method to a realistic CMB data set requires the ability to deal with spatially varying noise properties and partial sky coverage.

In this context, a general problem is the mixture of preferred basis representations. Whereas the covariance matrix of the primordial perturbations
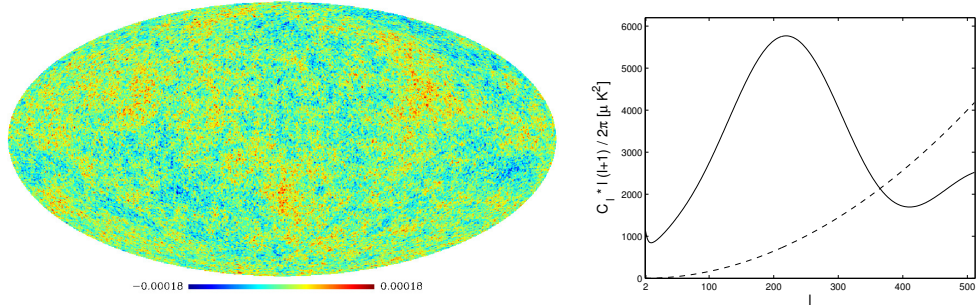
Figure 4.1: Properties of the maps analyzed. *Left panel:* Our non-Gaussian CMB signal simulation in dimensionless units. *Right panel:* The input signal (solid line) and noise (dashed line) power spectra.
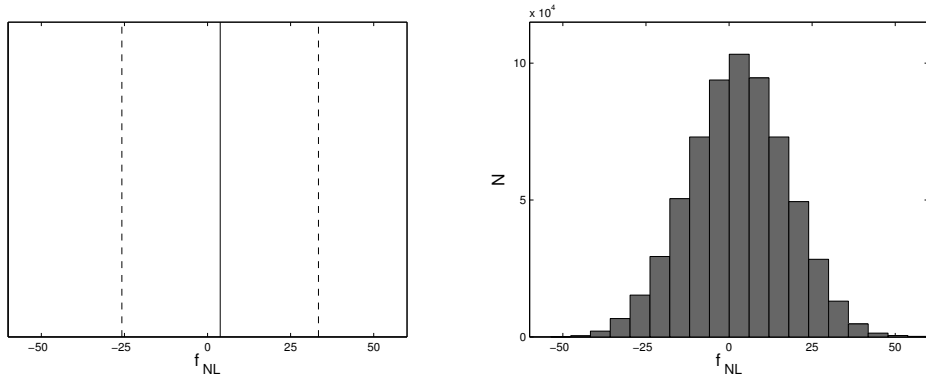

Figure 4.2: Analysis of the Gaussian simulation ($f_{\mathrm{NL}} = 0$). *Left panel:* We show the analysis of the Gaussian CMB map by means of the frequentist estimator. Plotted are the recovered value $\langle f_{\mathrm{NL}} \rangle = 4$ (*solid line*) and the $2-\sigma$ error (*dashed lines*) as derived from Monte Carlo simulations, $\sigma^{MC}_{f_{\mathrm{NL}}} = 15$. *Right panel:* The analysis of the same data set within a Bayesian framework constructs the full posterior distribution $P(f_{\mathrm{NL}}|d, \theta)$. We obtain a mean value of $\langle f_{\mathrm{NL}} \rangle = 3$ and a standard deviation of $\sigma_{f_{\mathrm{NL}}} = 15$.
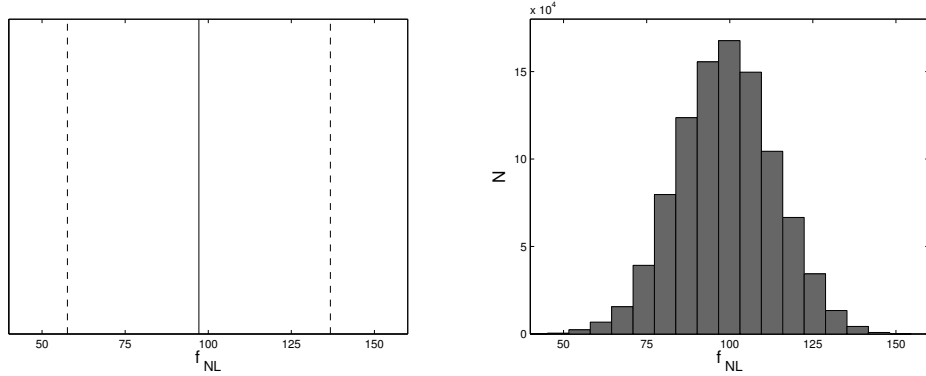
Figure 4.3: Same as Fig. 4.2, but for the non-Gaussian simulation ($f_{\mathrm{NL}} = 100$). The results from a frequentist analysis are $\langle f_{\mathrm{NL}} \rangle = 97$, $\sigma_{f_{\mathrm{NL}}}^{MC} = 20$. Using the Bayesian method, we obtain $\langle f_{\mathrm{NL}} \rangle = 99$ and $\sigma_{f_{\mathrm{NL}}} = 15$. For a significant detection of f_{NL}, the bispectrum estimator shows excess variance, whereas the analysis on the basis of the exact Bayesian approach still provides tight error bounds.
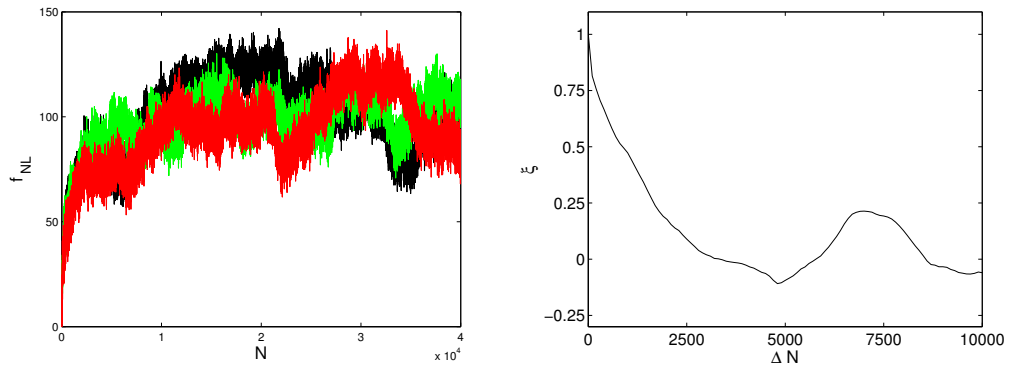

Figure 4.4: Performance of the sampling algorithm. *Left panel:* We plot a random selection of three of the 32 f_{NL} sampling chains that build up the histogram in Fig. 4.3. We discarded the first 10 000 samples during burn-in. *Right panel:* The autocorrelation function of a sampling chain.

can naturally be expressed in spherical harmonic space, the noise covariance matrix and the sky mask are defined best in pixel space. For the frequentist estimator, this is known to be problematic as e.g. in the calculation of the auxiliary map $B(r, \hat{n})$ in Eq. 4.5 (the Wiener filtered primordial fluctuations, see also Eqs. 4.22 for an equivalent, but more didactic expression), the inversion of a combination of the two covariance matrices has to be computed. For anisotropic noise, this can only be done by means of iterative solvers, whose numerical efficiencies depend crucially on the ability to identify powerful preconditioners[1].

For the Bayesian analysis scheme as presented here, however, the relevant equations do not contain any terms of this structure. Therefore, the computations remain straightforward even in the presence of arbitrary anisotropic noise properties and sky cuts. To demonstrate this ability, we performed a reanalysis of the simulated non-Gaussian temperature map of Sect. 4.4, now superimposed by anisotropic noise as typically expected for a high frequency WMAP channel. With these parameters, the average noise power spectrum roughly remains at a level of about $\mathcal{C}_\ell^{noise} \approx 10^{-7} \text{mK}^2$, but the noise is no longer spatially invariant. Including the KQ75y7 extended temperature mask, we we show the diagonal elements of the inverse noise covariance matrix in Fig. 4.5.

Again, for the analysis, we generated 32 independent Monte Carlo chains with 105 000 samples. After discarding the first 15 000 elements during burn-in, we applied the Gelman-Rubin convergence diagnostics to the chains and obtain a value of $R = 1.5$. The computed mean of $\langle f_{\text{NL}} \rangle = 88$ and the 1-σ error of $\sigma_{f_{\text{NL}}} = 16$ are in agreement with the input values of the simulation. We show the constructed histogram on the right hand panel of Fig. 4.5, demonstrating the applicability of the algorithm to realistic data sets.

4.6   Summary

In this paper, we introduced an exact Bayesian approach to infer the level of non-Gaussianity of local type, f_{NL}, from realistic CMB temperature maps. We derived conditional probabilities for the primordial perturbations given the data, $P(\Phi_{\text{L}}|d, \theta)$, and for f_{NL} given the data and the perturbations, $P(f_{\text{NL}}|d, \Phi_{\text{L}}, \theta)$. We used Hamiltonian Monte Carlo sampling to draw valid

---

[1]This can be very difficult, see, e.g., the discussion in Smith et al. (2007)
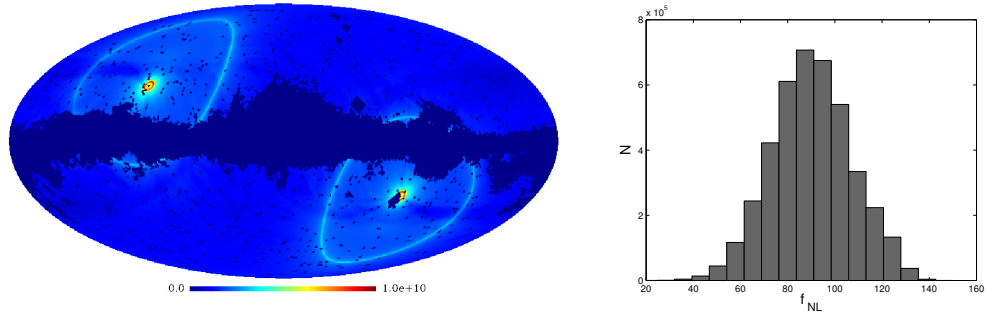
Figure 4.5: Analysis in case of a realistic CMB experiment. *Left panel:* We show the diagonal elements of the inverse noise covariance matrix in dimensionless units adopted for the more realistic simulation. When expressed in real space basis, off-diagonal terms vanish exactly. Pixel within the KQ75y7 mask are set to zero, corresponding to assigning infinite variance to them. *Right panel:* The constructed posterior distribution $P(f_{\mathrm{NL}}|d,\theta)$ of the simulated map. Obtaining $\langle f_{\mathrm{NL}}\rangle = 88$ and $\sigma_{f_{\mathrm{NL}}} = 16$ for the mean and standard deviation, respectively, the input value $(f_{\mathrm{NL}} = 100)$ gets consistently recovered.

realizations of Φ_{L} from which we in turn sample f_{NL}. After convergence these are samples from the full Bayesian posterior density of f_{NL} given the data.

For a direct comparison of the newly developed scheme to the conventional fast (bispectrum) estimator, we used simulated Gaussian and non-Gaussian CMB maps superimposed by isotropic noise. Estimates of the error bars within the frequentist approach were derived from Monte Carlo simulations. As a result, we find consistent outcomes between the two approaches for the analyzed Gaussian map, in agreement with the fact that the fast estimator is optimal in the limit of vanishing non-Gaussianity. In the non-Gaussian case, however, the advantage of the exact Bayesian approach becomes important. Here, the uncertainty in f_{NL} remains at the same level as for the Gaussian simulation, whereas the frequentist technique suffers from excess variance. Our results give the first example of an estimator (the "mean posterior estimator") that saturates the Cramer-Rao bound for f_{NL} even if the signal is detectably non-Gaussian.

Finally, we demonstrate the applicability of the newly developed method to a realistic data set with spatially varying noise properties and partial sky

102

coverage. Considering a WMAP-like noise covariance matrix and imposing the KQ75y7 extended temperature analysis mask, we analyze a non-Gaussian simulation and recover the input value consistently.

In the limit of undetectable non-Gaussianity, the Bayesian approach ought to yield the same information as the optimal bispectrum estimator (Babich 2005; Creminelli et al. 2007). Even in that limit it is useful as a cross-check since it is implemented in a completely different way. Although being computationally expensive, we conclude that the method presented here is a viable tool to exactly infer the level of non-Gaussianity of local type from CMB radiation experiments within a Bayesian framework.

Bibliography

Acquaviva, V., Bartolo, N., Matarrese, S., & Riotto, A. 2003, Nuclear Physics B, 667, 119

Albrecht, A. & Steinhardt, P. J. 1982, Physical Review Letters, 48, 1220

Babich, D. 2005, Phys. Rev. D, 72, 043003

Barreiro, R. B., Hobson, M. P., Banday, A. J., et al. 2004, MNRAS, 351, 515

Creminelli, P., Nicolis, A., Senatore, L., Tegmark, M., & Zaldarriaga, M. 2006, J. Cosmology Astropart. Phys., 5, 4

Creminelli, P., Senatore, L., & Zaldarriaga, M. 2007, J. Cosmology Astropart. Phys., 3, 19

Dickinson, C., Eriksen, H. K., Banday, A. J., et al. 2009, ApJ, 705, 1607

Duane, S., Kennedy, A. D., J., P. B., & D., R. 1987, Physics Letters B, 195, 216

Efstathiou, G., Ma, Y., & Hanson, D. 2010, MNRAS, 407, 2530

Elsner, F. & Wandelt, B. D. 2009, ApJS, 184, 264

Elsner, F., Wandelt, B. D., & Schneider, M. D. 2010, A&A, 513, A59+

Enqvist, K. & Sloth, M. S. 2002, Nuclear Physics B, 626, 395

Enßlin, T. A., Frommert, M., & Kitaura, F. S. 2009, Phys. Rev. D, 80, 105005

Eriksen, H. K., Dickinson, C., Jewell, J. B., et al. 2008a, ApJ, 672, L87

Eriksen, H. K., Dickinson, C., Lawrence, C. R., et al. 2006, New Astronomy
    Review, 50, 861

Eriksen, H. K., Jewell, J. B., Dickinson, C., et al. 2008b, ApJ, 676, 10

Gangui, A., Lucchin, F., Matarrese, S., & Mollerach, S. 1994, ApJ, 430, 447

Gelman, A. & Rubin, D. B. 1992, Statistical Science, 7, 457

Górski, K. M., Hivon, E., Banday, A. J., et al. 2005, ApJ, 622, 759

Guth, A. H. 1981, Phys. Rev. D, 23, 347

Hinshaw, G., Weiland, J. L., Hill, R. S., et al. 2009, ApJS, 180, 225

Hobson, M. P., Jones, A. W., Lasenby, A. N., & Bouchet, F. R. 1998, MN-
    RAS, 300, 1

Jewell, J., Levin, S., & Anderson, C. H. 2004, ApJ, 609, 1

Jewell, J. B., Eriksen, H. K., Wandelt, B. D., et al. 2009, ApJ, 697, 258

Khoury, J., Ovrut, B. A., Steinhardt, P. J., & Turok, N. 2001, Phys. Rev. D,
    64, 123522

Komatsu, E., Dunkley, J., Nolta, M. R., et al. 2009, ApJS, 180, 330

Komatsu, E., Kogut, A., Nolta, M. R., et al. 2003, ApJS, 148, 119

Komatsu, E., Smith, K. M., Dunkley, J., et al. 2010, ArXiv e-prints

Komatsu, E., Spergel, D. N., & Wandelt, B. D. 2005, ApJ, 634, 14

Komatsu, E., Wandelt, B. D., Spergel, D. N., Banday, A. J., & Górski, K. M. 2002, ApJ, 566, 19

Larson, D., Dunkley, J., Hinshaw, G., et al. 2010, ArXiv e-prints

Larson, D. L., Eriksen, H. K., Wandelt, B. D., et al. 2007, ApJ, 656, 653

Liguori, M., Matarrese, S., & Moscardini, L. 2003, ApJ, 597, 57

Liguori, M., Yadav, A., Hansen, F. K., et al. 2007, Phys. Rev. D, 76, 105016

Linde, A. D. 1982, Physics Letters B, 108, 389

Lyth, D. H., Ungarelli, C., & Wands, D. 2003, Phys. Rev. D, 67, 023503

Maldacena, J. 2003, Journal of High Energy Physics, 5, 13

Moroi, T. & Takahashi, T. 2001, Physics Letters B, 522, 215

Pitrou, C., Uzan, J., & Bernardeau, F. 2010, ArXiv e-prints

Rocha, G., Magueijo, J., Hobson, M., & Lasenby, A. 2001, Phys. Rev. D, 64, 063512

Salopek, D. S. & Bond, J. R. 1990, Phys. Rev. D, 42, 3936

Smith, K. M., Senatore, L., & Zaldarriaga, M. 2009, J. Cosmology Astropart. Phys., 9, 6

Smith, K. M., Zahn, O., & Doré, O. 2007, Phys. Rev. D, 76, 043510

Spergel, D. N., Bean, R., Doré, O., et al. 2007, ApJS, 170, 377

Spergel, D. N., Verde, L., Peiris, H. V., et al. 2003, ApJS, 148, 175

Starobinskiĭ, A. A. 1982, Physics Letters B, 117, 175

Steinhardt, P. J. & Turok, N. 2002, Phys. Rev. D, 65, 126003

Taylor, J. F., Ashdown, M. A. J., & Hobson, M. P. 2008, MNRAS, 389, 1284

Vielva, P. & Sanz, J. L. 2009, MNRAS, 397, 837

Wandelt, B. D., Larson, D. L., & Lakshminarayanan, A. 2004, Phys. Rev. D, 70, 083511

Yadav, A. P. S., Komatsu, E., & Wandelt, B. D. 2007, ApJ, 664, 680

Yadav, A. P. S., Komatsu, E., Wandelt, B. D., et al. 2008, ApJ, 678, 578

Yadav, A. P. S. & Wandelt, B. D. 2008, Physical Review Letters, 100, 181301

Yadav, A. P. S. & Wandelt, B. D. 2010, Advances in Astronomy, 2010

Chapter 5

Summary

In the standard model of cosmology, the universe arose out of a hot big bang followed by a phase of cool-down due to an adiabatic expansion (Linde 1990b; Dodelson 2003; Mukhanov 2005). This simple model is very successful in explaining the most important cosmological observations, namely the black body nature of the cosmic microwave background (CMB) radiation, the abundance patterns of the light elements generated during the primordial nucleosynthesis, and Hubble's law. Although being in good agreement with these findings, some observations lack a sound explanation within this framework. To be more specific, the flatness of the universe, the absence of relic particles as magnetic monopoles, the almost perfect isotropy of the CMB radiation, and the source of the seeds for structure formation put challenges to standard cosmology. Albeit not in strict conflict with experiments, the initial conditions of the universe have to be fine tuned to very high accuracy in order to make the model consistent with observations.

The theory of inflation provides a valuable extension to the standard model of cosmology that remedies the aforementioned discrepancies (Guth 1981; Linde 1982; Albrecht & Steinhardt 1982). In its simplest realization, it proposes the existence of a scalar field, the inflaton, which triggered a short epoch of exponential expansion immediately after the big bang. Because in this scenario today's observable universe has emerged out of a tiny patch in thermal equilibrium that was stretched to macroscopic sizes, the predictions for some of its fundamental properties change and now are in agreement with observations in a natural way.

The forecasts of inflation are largely independent of the details of the particular underlying model. As a result, to distinguish between competitive

versions of inflationary theories, one has to probe experimental data for very subtle effects. For example, the simplest inflationary scenarios predict the primordial perturbations to be almost perfectly Gaussian (Acquaviva et al. 2003; Maldacena 2003). However, if the physical mechanisms responsible for generating the perturbations deviate from the simplest setup, a non-Gaussian signature is generically introduced.

As any non-Gaussian contribution present in the primordial fluctuations gets imprinted onto the CMB radiation, the search for non-Gaussianity in CMB data becomes an important test of the physical processes in the very early universe. With the advent of full-sky CMB temperature measurements conducted by the *Cosmic Background Explorer* (COBE) and the *Wilkinson Microwave Anisotropy Probe* (WMAP) satellites, it was possible to impose stringent limits on the amplitude of non-Gaussianity (e.g. Bennett et al. 1996; Komatsu et al. 2003). The situation will further improve considerably once data of the Planck satellite mission become available which do not only supersede WMAP's temperature maps in resolution and noise level, but also provide high quality full-sky polarization information (Efstathiou et al. 2005).

A classification scheme has been introduced to group inflationary models according to their non-Gaussian signature. It is based on the characteristic momentum modes dominating the contribution to the bispectrum, the Fourier transform of the 3-point correlation function. Regarding non-Gaussianity of equilateral type, for example, the important modes roughly form a triangle of equilateral shape in momentum space, i.e. they are of comparable absolute value. This kind of non-Gaussianity is predicted by models with modified kinetic term in the inflaton Lagrangian (Babich et al. 2004). Models where the inflaton vacuum expectation value deviates from the simple Bunch-Davies ground state fall into another class. Here, the bispectrum shape function peaks at folded triangle configurations, i.e. when one momentum is considerably larger than the other two (Chen et al. 2007). A third class is defined by multi-field inflationary models, where the processes responsible for generating the primordial fluctuations were driven (or at least affected) by another field. In this case, the relevant momentum configuration can be described by a squeezed triangle, that is, one momentum is considerably smaller than the other two (Babich et al. 2004). In this thesis, we focused on the search for primordial non-Gaussianity of local type.

Non-Gaussianity of local type is generically predicted in multi-field inflationary models (Moroi & Takahashi 2001; Lyth et al. 2003). Also, models encountered in string theory as the cyclic/ekpyrotic universe model fall

108

within this class (Khoury et al. 2001; Enqvist & Sloth 2002; Steinhardt & Turok 2002b). According to these theories, the primordial fluctuations Φ can be perturbational expanded in terms of a Gaussian auxiliary field Φ_{L} and its non-linear transform (Salopek & Bond 1990; Gangui et al. 1994),

$$\Phi(r) = \Phi_{\mathrm{L}}(r) + f_{\mathrm{NL}}\left(\Phi_{\mathrm{L}}^2(r) - \langle\Phi_{\mathrm{L}}^2(r)\rangle\right) + \mathcal{O}(\Phi_{\mathrm{L}}^3), \qquad (5.1)$$

where f_{NL} is the dimensionless amplitude of non-Gaussianity and we have truncated the expansion at third order in Φ_{L}. By the addition of a quadratic contribution to the primordial fluctuations Φ, we introduce a phase correlation among the different formerly uncoupled Fourier modes.

The main objective of this work was to develop and implement a Bayesian method to infer the level of non-Gaussianity from CMB maps. To assess the performance and validity of a newly introduced scheme, the analysis of simulated yet realistic data sets with known statistical properties is mandatory. To this end, we first proposed an efficient method to generate temperature and polarization CMB maps with an arbitrary level of local non-Gaussianity. In this algorithm, we synthesize the 3-dimensional Gaussian primordial perturbations Φ_{L} in spherical harmonic space, properly accounting for the radial correlations. The non-Gaussian contribution is calculated according to Eq. 5.1, where the expression is to be evaluated in pixel space. Then, the curvature perturbations get projected onto a 2-dimensional CMB map by means of a line-of-sight integral using the radiation transfer functions. To increase the accuracy as well as numerical efficiency of the method, we proposed a new optimization scheme which aims at finding both optimal nodes and optimal weights needed for the numerical quadrature. Given the cosmological parameters as inferred from WMAP 5-year data, baryonic acoustic oscillations, and supernova distance measurements, we generated 1000 realizations of simulated CMB temperature and polarization maps. After validating the results using the traditional frequentist bispectrum estimator (Komatsu et al. 2005), we provided them to the community[1].

As a next step, we derived the basic equations to measure the level of non-Gaussianity of local type in CMB data using Bayesian statistics. We obtained an expression for the joint probability distribution of the primordial perturbations, Φ, the level of non-Gaussianity, f_{NL}, the remaining cosmological parameters, θ, and the data, d. However, the very high dimensionality

---

[1]Available at `http://planck.mpa-garching.mpg.de/cmb/fnl-simulations`

109

of the parameter space prohibits to evaluate the equation directly. To circumvent this problem, we proposed a Hamiltonian Monte Carlo algorithm to draw f_{NL}-samples from the target distribution. Once this process has been repeated sufficiently often, the samples build up the exact posterior distribution of f_{NL} given the data. For the case of weak non-Gaussianity and high signal-to-noise ratios, we also identified a numerically much more efficient yet approximate method to sample from the posterior distribution.

We demonstrated the applicability of the newly developed scheme by studying a simplified 1-dimensional toy model of the CMB radiation. Analyzing data sets with varying non-Gaussian contribution, we found the width of the posterior distribution to be constant. In contrast, this is not the case for the conventional frequentist estimator, where an f_{NL}-dependent excess variance has been observed (Creminelli et al. 2007; Liguori et al. 2007), pointing towards a fundamental advantage of the newly developed Bayesian approach.

After a further refinement of the method, we fully implemented a parallelized version of the algorithm which is capable of calculating the level of non-Gaussianity from realistic CMB temperature maps using Hamiltonian Monte Carlo sampling. This is done in a two-step process. We first produce a valid realization of the Gaussian auxiliary field from the f_{NL}-marginalized conditional probability $\Phi_{\mathrm{L}} \hookleftarrow P(\Phi_{\mathrm{L}}|d, \theta)$. Then, we draw a f_{NL} sample from the Gaussian conditional density given the previously derived primordial perturbation, $f_{\mathrm{NL}} \hookleftarrow P(f_{\mathrm{NL}}|\Phi_{\mathrm{L}}, d, \theta)$. After iterating this process for a sufficient amount of cycles, the generated set of f_{NL} values is an unbiased representation of the target posterior distribution.

We compared our exact Bayesian approach to the frequentist estimator which only takes into account information from the 3-point correlation function of the data set. For the analysis of a simulated Gaussian CMB map with isotropic noise characteristics, we find the two schemes to produce results in good agreement with each other. For simulations containing a significant amount of non-Gaussianity, however, the bispectrum estimator is no longer optimal, i.e. its variance is artificially enhanced. Contrary, the Bayesian method still provides the tightest possible error bounds.

As a last step, we analyzed a non-Gaussian simulation with anisotropic noise and partial sky coverage to demonstrate the applicability of the Bayesian scheme to CMB maps obtained from realistic experiments. We find that all relevant equations can be extended straightforwardly. We conclude, there-

110

fore, that the newly developed scheme is an important tool to infer the level of non-Gaussianity of local type from CMB data in an optimal way.

Although being a very valuable extension to the standard model of cosmology, in inflation some problems of principle remain. For example, if a scalar field was the driving force behind the inflationary epoch, tracing back the evolution of the universe inevitably leads to a singularity at the time of the big bang (Hawking & Penrose 1970; Borde & Vilenkin 1994). Because the initial values of physical quantities like the energy density are indefinite, the theory must be considered incomplete.

A somewhat similar problem is known as trans-Planckian problem. If inflation has sustained long enough (i.e. if the universe expanded by a factor of at least 70 e-folds), all fluctuations within the Hubble radius today originally stem from a tiny patch smaller than the Planck length. Because our theoretical description of space-time must be expected to brake down at this scales, new and as yet not understood physics may have played a role during the process of generating the primordial perturbations. And it is still an open question, whether the predictions of inflation are robust to or depend sensitively on trans-Planckian phenomenons (Easther et al. 2001, 2002; Shiu & Wasserman 2002).

Over the last decades, people tried to construct theories that are capable of consistently explaining the evolution of the universe from the very beginning, either embedding or completely replacing the inflationary mechanism discussed so far. As this goal is very ambitious, a much more comprehensive framework must be worked out, going far beyond the well tested standard model of physics. Such a theory has to include an unification of general relativity and quantum mechanics, presumably resulting in the need to modify the most fundamental properties of the universe as increasing the number of spatial dimensions in string theory (e.g. Green et al. 1986; Lüst & Theisen 1989; Zwiebach 2004), or quantizing space-time in loop quantum gravity (e.g. Ashtekar & Tate 1991; Rovelli 1998; Thiemann 2001). For the time being, the success of these efforts is unpredictable; whatever theory will finally emerge out of today's approaches, however, it must be able to explain the observed features of the universe, including any non-Gaussian signatures in the CMB.

Appendix A

Supplement to the simulation algorithm

In the following, we provide supplementary information to Chap. 2.

The power spectrum of the Gaussian CMB radiation anisotropies can be related to the statistical properties of the linear primordial perturbations (e.g. Dodelson 2003),

$$
\begin{aligned}
\mathcal{C}_\ell &= \langle a_{\ell m}\, a_{\ell m}^* \rangle \\
&= \frac{2}{\pi} \int dk\, k^2 g_\ell^2(k)\, \mathcal{P}(k)\,,
\end{aligned}
\tag{A.1}
$$

where the $g_\ell(k)$ represent the radiation transfer functions and $\mathcal{P}(k)$ denotes the primordial power spectrum.

Retaining the notation introduced above, we now derive the corresponding expression for the CMB radiation power spectrum of the non-Gaussian

part, $\mathcal{C}_\ell^{\mathrm{NL}}$, by solving the line-of-sight integral over the non-Gaussian primordial perturbations for $f_{\mathrm{NL}} = 1$:

$$
\begin{aligned}
\mathcal{C}_\ell^{\mathrm{NL}} &= \langle a_{\ell m}^{\mathrm{NL}} \, a_{\ell m}^{\mathrm{NL}*} \rangle \\
&= \langle 4\pi(-i)^l \int \frac{d^3 k_1}{(2\pi)^3} \Phi^{\mathrm{NL}}(\vec{k}_1) g_\ell(k_1) Y_{\ell m}^*(\hat{k}_1) \\
&\quad \times 4\pi(-i)^{l*} \int \frac{d^3 k_2}{(2\pi)^3} \Phi^{\mathrm{NL}*}(\vec{k}_2) g_\ell(k_2) Y_{\ell m}(\hat{k}_2) \rangle \\
&= \frac{1}{4\pi^4} \int dk_1 k_1^2 d\Omega_{\hat{k}_1} \, dk_2 k_2^2 d\Omega_{\hat{k}_2} g_\ell(k_1) g_\ell(k_2) \\
&\quad \times \langle \Phi^{\mathrm{NL}}(\vec{k}_1) \, \Phi^{\mathrm{NL}*}(\vec{k}_2) \rangle Y_{\ell m}^*(\hat{k}_1) Y_{\ell m}(\hat{k}_2) \,. \qquad \text{(A.2)}
\end{aligned}
$$

The expectation value of the non-Gaussian potential can be written down explicitly making use of Eq. 1.36 transformed to Fourier space,

$$
\begin{aligned}
\langle \Phi^{\mathrm{NL}}(\vec{k}_1) \, \Phi^{\mathrm{NL}*}(\vec{k}_2) \rangle = \langle &\left(\int \frac{d^3 p_1}{(2\pi)^3} \Phi^{\mathrm{L}}(\vec{k}_1 + \vec{p}_1) \Phi^{\mathrm{L}*}(\vec{p}_1) - (2\pi)^3 \sigma^2 \delta^3(\vec{k}_1) \right) \\
&\times \left(\int \frac{d^3 p_2}{(2\pi)^3} \Phi^{\mathrm{L}*}(\vec{k}_2 + \vec{p}_2) \Phi^{\mathrm{L}}(\vec{p}_2) - (2\pi)^3 \sigma^2 \delta^3(-\vec{k}_2) \right) \rangle \,, \quad \text{(A.3)}
\end{aligned}
$$

where $\sigma^2 = (2\pi)^{-3} \int d^3 k \, \mathcal{P}(k)$ is the variance of the linear potential. As we do not consider a monopole contribution here, i.e. $|\vec{k}_i| > 0$, the expression simplifies,

$$
\begin{aligned}
\langle \Phi^{\mathrm{NL}}(\vec{k}_1) \, \Phi^{\mathrm{NL}*}(\vec{k}_2) \rangle \approx \langle &\int \frac{d^3 p_1}{(2\pi)^3} \Phi^{\mathrm{L}}(\vec{k}_1 + \vec{p}_1) \Phi^{\mathrm{L}*}(\vec{p}_1) \\
&\times \int \frac{d^3 p_2}{(2\pi)^3} \Phi^{\mathrm{L}*}(\vec{k}_2 + \vec{p}_2) \Phi^{\mathrm{L}}(\vec{p}_2) \rangle \,. \quad \text{(A.4)}
\end{aligned}
$$

114

Using the theorem of Wick, it is possible to split the expectation value into a sum over products according to the relation $\langle ABCD \rangle = \langle AB \rangle \langle CD \rangle + \langle AC \rangle \langle BD \rangle + \langle AD \rangle \langle BC \rangle$,

$$
\begin{aligned}
\langle \Phi^{\mathrm{NL}}(\vec{k}_1)\, \Phi^{\mathrm{NL}*}(\vec{k}_2) \rangle &= \int \frac{d^3 p_1}{(2\pi)^3} \int \frac{d^3 p_2}{(2\pi)^3} \langle \Phi^{\mathrm{L}}(\vec{k}_1 + \vec{p}_1)\, \Phi^{\mathrm{L}*}(\vec{p}_1) \rangle \\
&\quad \times \langle \Phi^{\mathrm{L}*}(\vec{k}_2 + \vec{p}_2)\, \Phi^{\mathrm{L}}(\vec{p}_2) \rangle \\
&\quad + \int \frac{d^3 p_1}{(2\pi)^3} \int \frac{d^3 p_2}{(2\pi)^3} \langle \Phi^{\mathrm{L}}(\vec{k}_1 + \vec{p}_1)\, \Phi^{\mathrm{L}*}(\vec{k}_2 + \vec{p}_2) \rangle \\
&\quad \times \langle \Phi^{\mathrm{L}*}(\vec{p}_1)\, \Phi^{\mathrm{L}}(\vec{p}_2) \rangle \\
&\quad + \int \frac{d^3 p_1}{(2\pi)^3} \int \frac{d^3 p_2}{(2\pi)^3} \langle \Phi^{\mathrm{L}}(\vec{k}_1 + \vec{p}_1)\, \Phi^{\mathrm{L}}(\vec{p}_2) \rangle \\
&\quad \times \langle \Phi^{\mathrm{L}*}(\vec{p}_1)\, \Phi^{\mathrm{L}*}(\vec{k}_2 + \vec{p}_2) \rangle \,.
\end{aligned} \tag{A.5}
$$

As the Φ^{L} are uncorrelated in momentum space, the expectation values can be computed as

$$
\begin{aligned}
\langle \Phi^{\mathrm{L}}(\vec{k}_1 + \vec{p}_1)\, \Phi^{\mathrm{L}*}(\vec{p}_1) \rangle &= (2\pi)^3\, \mathcal{P}(p_1)\, \delta^3(\vec{k}_1) \\
&= 0
\end{aligned} \tag{A.6}
$$

$$
\begin{aligned}
\langle \Phi^{\mathrm{L}*}(\vec{k}_2 + \vec{p}_2)\, \Phi^{\mathrm{L}}(\vec{p}_2) \rangle &= (2\pi)^3\, \mathcal{P}(p_2)\, \delta^3(-\vec{k}_2) \\
&= 0
\end{aligned} \tag{A.7}
$$

$$
\langle \Phi^{\mathrm{L}}(\vec{k}_1 + \vec{p}_1)\, \Phi^{\mathrm{L}*}(\vec{k}_2 + \vec{p}_2) \rangle = (2\pi)^3\, \mathcal{P}(k_1 + p_1)\, \delta^3(\vec{k}_1 + \vec{p}_1 - \vec{k}_2 - \vec{p}_2) \tag{A.8}
$$

$$
\langle \Phi^{\mathrm{L}*}(\vec{p}_1)\, \Phi^{\mathrm{L}}(\vec{p}_2) \rangle = (2\pi)^3\, \mathcal{P}(p_2)\, \delta^3(\vec{p}_2 - \vec{p}_1) \tag{A.9}
$$

$$
\langle \Phi^{\mathrm{L}}(\vec{k}_1 + \vec{p}_1)\, \Phi^{\mathrm{L}}(\vec{p}_2) \rangle = (2\pi)^3\, \mathcal{P}(k_1 + p_1)\, \delta^3(\vec{k}_1 + \vec{p}_1 + \vec{p}_2) \tag{A.10}
$$

$$
\langle \Phi^{\mathrm{L}*}(\vec{p}_1)\, \Phi^{\mathrm{L}*}(\vec{k}_2 + \vec{p}_2) \rangle = (2\pi)^3\, \mathcal{P}(p_1)\, \delta^3(-\vec{p}_1 - \vec{k}_2 - \vec{p}_2) \,. \tag{A.11}
$$

Thus, we derive for the autocorrelation function of the non-linear potential

$$
\begin{aligned}
\langle \Phi^{\mathrm{NL}}(\vec{k}_1)\, \Phi^{\mathrm{NL}*}(\vec{k}_2) \rangle &= \int d^3 p_1\, d^3 p_2\, \mathcal{P}(k_1 + p_1)\, \mathcal{P}(p_2) \\
&\quad \times \delta^3(\vec{k}_1 + \vec{p}_1 - \vec{k}_2 - \vec{p}_2)\delta^3(\vec{p}_2 - \vec{p}_1) \\
&\quad + \int d^3 p_1\, d^3 p_2\, \mathcal{P}(k_1 + p_1)\, \mathcal{P}(p_1) \\
&\quad \times \delta^3(\vec{k}_1 + \vec{p}_1 + \vec{p}_2)\delta^3(-\vec{p}_1 - \vec{k}_2 - \vec{p}_2) \\
&= 2 \int d^3 p\, \mathcal{P}(k_1 + p)\, \mathcal{P}(p)\, \delta^3(\vec{k}_1 - \vec{k}_2) \,,
\end{aligned} \tag{A.12}
$$

where we used $\vec{p}_2 = \vec{p}_1$ and $\vec{p}_2 = -\vec{k}_1 - \vec{p}_1$ to combine the first and second term, respectively.

Substituting Eq. A.12 in Eq. A.2, we obtain a simplified relation for the non-Gaussian CMB radiation power spectrum,

$$\mathcal{C}_\ell^{\mathrm{NL}} = \frac{1}{2\pi^4} \int d^3p \, dk_1 k_1^2 d\Omega_{\hat{k}_1} \, dk_2 k_2^2 d\Omega_{\hat{k}_2} \, g_\ell(k_1) g_\ell(k_2) \, \mathcal{P}(k_1 + p) \, \mathcal{P}(p)$$
$$\times \, \delta^3(\vec{k}_1 - \vec{k}_2) Y_{\ell m}^*(\hat{k}_1) Y_{\ell m}(\hat{k}_2) \,. \quad \text{(A.13)}$$

Rewriting the delta function by means of a Fourier transform,

$$\delta^3(\vec{k}_1 - \vec{k}_2) = \frac{1}{(2\pi)^3} \int d^3r \, \mathrm{e}^{i(\vec{k}_1 - \vec{k}_2)\cdot\vec{r}} \,, \quad \text{(A.14)}$$

and making use of the plane wave expansion of the complex exponential,

$$\mathrm{e}^{i\vec{k}\cdot\vec{r}} = 4\pi \sum_{\ell m} i^\ell Y_{\ell m}(\hat{k}) Y_{\ell m}^*(\hat{r}) j_\ell(kr) \,, \quad \text{(A.15)}$$

we derive

$$\mathcal{C}_\ell^{\mathrm{NL}} = \frac{1}{\pi^5} \int d^3p \, dr r^2 d\Omega_{\hat{r}} \, dk_1 k_1^2 d\Omega_{\hat{k}_1} \, dk_2 k_2^2 d\Omega_{\hat{k}_2} \, g_\ell(k_1) g_\ell(k_2) \, \mathcal{P}(k_1 + p) \, \mathcal{P}(p)$$
$$\times \sum_{\ell_1 \ell_2 m_1 m_2} i^{l_1 - l_2} Y_{\ell_1 m_1}(\hat{k}_1) Y_{\ell_1 m_1}^*(\hat{r}) j_{\ell_1}(k_1 r)$$
$$\times Y_{\ell_2 m_2}^*(\hat{k}_2) Y_{\ell_2 m_2}(\hat{r}) j_{\ell_2}(k_2 r) Y_{\ell m}^*(\hat{k}_1) Y_{\ell m}(\hat{k}_2)$$
$$= \frac{1}{\pi^5} \int d^3p \, dr r^2 d\Omega_{\hat{r}} \, dk_1 k_1^2 d\Omega_{\hat{k}_1} \, dk_2 k_2^2 d\Omega_{\hat{k}_2} \, g_\ell(k_1) g_\ell(k_2) \, \mathcal{P}(k_1 + p) \, \mathcal{P}(p)$$
$$\times j_\ell(k_1 r) j_\ell(k_2 r) \,. \quad \text{(A.16)}$$

Substituting the identity

$$\int dr r^2 \, j_\ell(k_1 r) j_\ell(k_2 r) = \frac{\pi}{2} \frac{1}{k_1^2} \delta(k_1 - k_2) \,, \quad \text{(A.17)}$$

we finally obtain the non-Gaussian part of the CMB radiation power spectrum as convolution integral of the primordial power spectrum times the transfer functions,

$$\mathcal{C}_\ell^{\mathrm{NL}} = \frac{2}{\pi^3} \int dp p^2 \, dk k^2 \, g_\ell^2(k) \, \mathcal{P}(k + p) \, \mathcal{P}(p) \,. \quad \text{(A.18)}$$

We show a comparison of the averaged power spectrum of 1000 non-Gaussian simulations to the theoretical values in Fig. A.1
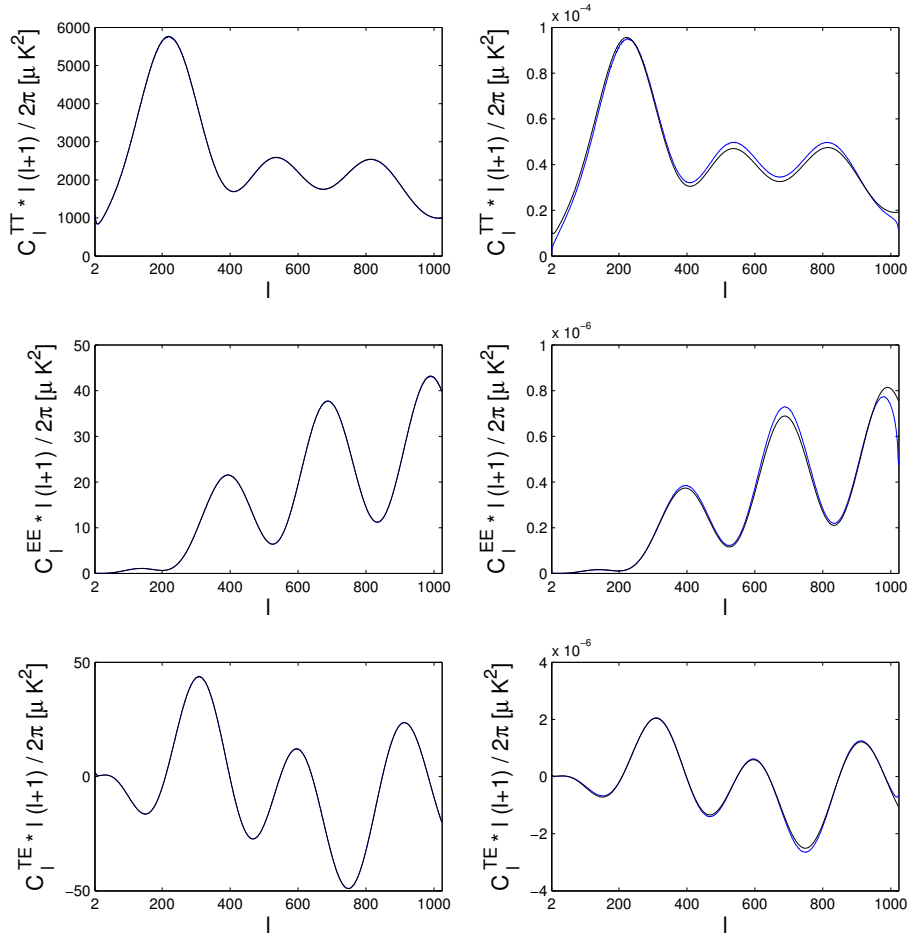
116

Figure A.1: Test of the power spectrum. We compare the theoretically expected power spectrum (*black lines*) to the averaged power spectrum of the 1000 simulated temperature and polarization CMB radiation maps (*blue lines*). We show the temperature ($\mathcal{C}_\ell^{TT}$, *upper row*), polarization ($\mathcal{C}_\ell^{EE}$, *middle row*) and cross power spectrum ($\mathcal{C}_\ell^{TE}$, *lower row*) of the Gaussian part (*left column*) and the non-Gaussian part (*right column*) of the simulation. As the systematic deviation of the Gaussian part is below 1%, the lines cannot be discerned in this view.

Appendix B

Non-Gaussian signatures of higher order

In Chap. 3 et seq., we developed an optimal way to infer the level of non-Gaussianity of local type from CMB data. For the analysis, we focused on the perturbational expansion of the primordial fluctuations up to second order in Φ (see Eq. 1.36). However, as the quality of observational data will considerable improve once CMB maps measured by the Planck satellite experiment are released, it becomes possible to target constraining the next-to-leading order non-Gaussian term.

For local non-Gaussianity, the expansion Eq. 1.36 can be revised to include the term $\mathcal{O}(\Phi_{\mathrm{L}}^3)$,

$$\Phi(r) = \Phi_{\mathrm{L}}(r) + f_{\mathrm{NL}} \left(\Phi_{\mathrm{L}}^2(r) - \langle \Phi_{\mathrm{L}}^2(r) \rangle \right) + g_{\mathrm{NL}}\, \Phi_{\mathrm{L}}^3 + \mathcal{O}(\Phi_{\mathrm{L}}^4)\,, \qquad \text{(B.1)}$$

where g_{NL} is the amplitude of the non-Gaussian contribution proportional to the cubic term of the primordial perturbations. We show an example of a simulated CMB temperature map and its first and second order non-Gaussian contribution in Fig. B.1.

Using WMAP data, first attempts have been made to provide limits to g_{NL} (Vielva & Sanz 2009), currently leading to the weak constrain of $-7.4 \cdot 10^5 \leq g_{\mathrm{NL}} \leq 8.3 \cdot 10^5$ at 2-σ level (Smidt et al. 2010). This result has been derived within a frequentist approach, using estimators similar in construction to the bispectrum estimator.

As several inflationary models predict the first and second order parameter of non-Gaussianity to be correlated, a simultaneous analysis would be
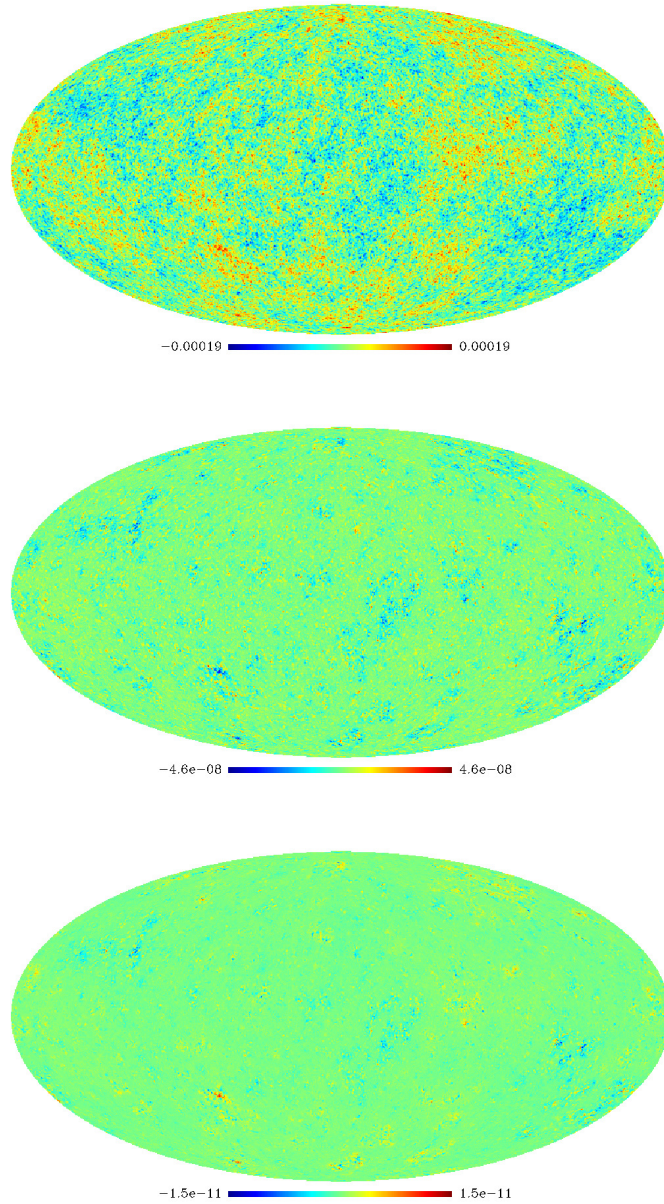
Figure B.1: Higher order non-Gaussianity. We show an example of a set of CMB temperature maps consisting of the Gaussian part (*upper panel*), the first-order non-Gaussian part ($\propto f_{\mathrm{NL}}$, *middle panel*), and the second-order non-Gaussian part ($\propto g_{\mathrm{NL}}$, *lower panel*).

120

beneficial. In the following, we briefly outline how this can be done exactly within a Bayesian framework on the basis of the sampling algorithm presented in the previous chapters.

We revise the joint distribution to include the new variable g_{NL} into the analysis,

$$P(d, \Phi_{\mathrm{L}}, f_{\mathrm{NL}}, g_{\mathrm{NL}}, \theta) = P(d|\Phi_{\mathrm{L}}, f_{\mathrm{NL}}, g_{\mathrm{NL}}, \theta)\, P(\Phi_{\mathrm{L}}|\theta)\, P(\theta)\, P(f_{\mathrm{NL}})\, P(g_{\mathrm{NL}})\,, \tag{B.2}$$

where we introduced the prior distribution $P(g_{\mathrm{NL}})$ which we assume to be Gaussian in what follows. Making use of Eq. B.1, the explicit expression for Eq. B.2 transforms to

$$
\begin{aligned}
P(d, \Phi_{\mathrm{L}}, f_{\mathrm{NL}}, g_{\mathrm{NL}}, \theta) \propto \exp\Big\{ &-1/2\, \big[d - M(\Phi_{\mathrm{L}} + f_{\mathrm{NL}}(\Phi_{\mathrm{L}}^2 - \langle\Phi_{\mathrm{L}}^2\rangle) + g_{\mathrm{NL}}\Phi^3)\big]^\dagger \\
&\times N^{-1}\big[d - M(\Phi_{\mathrm{L}} + f_{\mathrm{NL}}(\Phi_{\mathrm{L}}^2 - \langle\Phi_{\mathrm{L}}^2\rangle) + g_{\mathrm{NL}}\Phi^3)\big] \\
&-1/2\,\Phi_{\mathrm{L}}^\dagger P_\Phi^{-1}\Phi_{\mathrm{L}} - f_{\mathrm{NL}}^2/2\sigma_{f_{\mathrm{NL}}}^2 - g_{\mathrm{NL}}^2/2\sigma_{g_{\mathrm{NL}}}^2 \Big\}\,.
\end{aligned}
\tag{B.3}
$$

Following the procedure outlined in Chap. 4, we first find conditional expressions for the two parameters of non-Gaussianity, $P(f_{\mathrm{NL}}|d, \Phi, g_{\mathrm{NL}}, \theta)$ and $P(g_{\mathrm{NL}}|d, \Phi, f_{\mathrm{NL}}, \theta)$, both of which are Gaussian with mean and variance,

$$
\begin{aligned}
\langle f_{\mathrm{NL}}\rangle &= \langle(f_{\mathrm{NL}} - \langle f_{\mathrm{NL}}\rangle)^2\rangle(\Phi_{\mathrm{L}}^2 - \langle\Phi_{\mathrm{L}}^2\rangle)^\dagger M^\dagger N^{-1} \\
&\quad\times (d - M\Phi_{\mathrm{L}} - g_{\mathrm{NL}}M\Phi_{\mathrm{L}}^3)\,, \\
\langle(f_{\mathrm{NL}} - \langle f_{\mathrm{NL}}\rangle)^2\rangle &= \big[(\Phi_{\mathrm{L}}^2 - \langle\Phi_{\mathrm{L}}^2\rangle)^\dagger M^\dagger N^{-1}M(\Phi_{\mathrm{L}}^2 - \langle\Phi_{\mathrm{L}}^2\rangle) + 1/\sigma_{f_{\mathrm{NL}}}^2\big]^{-1}\,, \text{ and}
\end{aligned}
\tag{B.4}
$$

$$
\begin{aligned}
\langle g_{\mathrm{NL}}\rangle &= \langle(g_{\mathrm{NL}} - \langle g_{\mathrm{NL}}\rangle)^2\rangle\,\Phi_{\mathrm{L}}^{3\dagger} M^\dagger N^{-1} \\
&\quad\times (d - M\Phi_{\mathrm{L}} - f_{\mathrm{NL}}M(\Phi_{\mathrm{L}}^2 - \langle\Phi_{\mathrm{L}}^2\rangle))\,, \\
\langle(g_{\mathrm{NL}} - \langle g_{\mathrm{NL}}\rangle)^2\rangle &= \big[\Phi_{\mathrm{L}}^{3\dagger} M^\dagger N^{-1}M\Phi_{\mathrm{L}}^3 + 1/\sigma_{g_{\mathrm{NL}}}^2\big]^{-1}\,.
\end{aligned}
\tag{B.5}
$$

As a next step, we marginalize the conditional probability of the linear primordial perturbations, $P(\Phi, f_{\mathrm{NL}}, g_{\mathrm{NL}}|d, \theta)$, over f_{NL} and g_{NL} to obtain an expression that only depends on the data and the cosmological parameter,

$$
\begin{aligned}
P(\Phi|d,\theta) &= \int df_{\mathrm{NL}}\, dg_{\mathrm{NL}}\, P(\Phi, f_{\mathrm{NL}}, g_{\mathrm{NL}}|d,\theta) \\
&\propto \int df_{\mathrm{NL}}\, dg_{\mathrm{NL}}\, \mathrm{e}^{-1/2\left[d-M(\Phi_{\mathrm{L}}+f_{\mathrm{NL}}(\Phi_{\mathrm{L}}^2-\langle\Phi_{\mathrm{L}}^2\rangle)+g_{\mathrm{NL}}\Phi^3)\right]^\dagger} \\
&\quad \times N^{-1}\left[d-M(\Phi_{\mathrm{L}}+f_{\mathrm{NL}}(\Phi_{\mathrm{L}}^2-\langle\Phi_{\mathrm{L}}^2\rangle)+g_{\mathrm{NL}}\Phi^3)\right] \\
&\quad -1/2\,\Phi_{\mathrm{L}}^\dagger P_\Phi^{-1}\Phi_{\mathrm{L}}-f_{\mathrm{NL}}^2/2\sigma_{f_{\mathrm{NL}}}^2-g_{\mathrm{NL}}^2/2\sigma_{g_{\mathrm{NL}}}^2\,.
\end{aligned}
\tag{B.6}
$$

Performing the f_{NL} integral first, we find

$$
\begin{aligned}
P(\Phi, g_{\mathrm{NL}}|d,\theta) &\propto \mathrm{e}^{-1/2(d-M(\Phi_{\mathrm{L}}+g_{\mathrm{NL}}\Phi^3))^\dagger N^{-1}(d-M(\Phi_{\mathrm{L}}+g_{\mathrm{NL}}\Phi^3))-1/2\,\Phi_{\mathrm{L}}^\dagger P_\Phi^{-1}\Phi_{\mathrm{L}}-g_{\mathrm{NL}}^2/2\sigma_{g_{\mathrm{NL}}}^2} \\
&\quad \times \int df_{\mathrm{NL}}\, \mathrm{e}^{f_{\mathrm{NL}}(\Phi_{\mathrm{L}}^2-\langle\Phi_{\mathrm{L}}^2\rangle)^\dagger M^\dagger N^{-1}(d-M(\Phi_{\mathrm{L}}+g_{\mathrm{NL}}\Phi^3))} \\
&\quad {}^{-1/2f_{\mathrm{NL}}^2(\Phi_{\mathrm{L}}^2-\langle\Phi_{\mathrm{L}}^2\rangle)^\dagger M^\dagger N^{-1}M(\Phi_{\mathrm{L}}^2-\langle\Phi_{\mathrm{L}}^2\rangle)-f_{\mathrm{NL}}^2/2\sigma_{f_{\mathrm{NL}}}^2} \\
&= \mathrm{e}^{-1/2(d-M(\Phi_{\mathrm{L}}+g_{\mathrm{NL}}\Phi^3))^\dagger N^{-1}(d-M(\Phi_{\mathrm{L}}+g_{\mathrm{NL}}\Phi^3))-1/2\,\Phi_{\mathrm{L}}^\dagger P_\Phi^{-1}\Phi_{\mathrm{L}}-g_{\mathrm{NL}}^2/2\sigma_{g_{\mathrm{NL}}}^2} \\
&\quad \times \int df_{\mathrm{NL}}\, \mathrm{e}^{-\frac{(f_{\mathrm{NL}}-\bar{f}_{\mathrm{NL}})^2}{2\bar{\sigma}_{f_{\mathrm{NL}}}}+\frac{\bar{f}_{\mathrm{NL}}^2}{2\bar{\sigma}_{f_{\mathrm{NL}}}}} \\
&\propto \left[\sigma_{f_{\mathrm{NL}}}^2(\Phi_{\mathrm{L}}^2-\langle\Phi_{\mathrm{L}}^2\rangle)^\dagger M^\dagger N^{-1}M(\Phi_{\mathrm{L}}^2-\langle\Phi_{\mathrm{L}}^2\rangle)+1\right]^{-1/2} \\
&\quad \times \mathrm{e}^{-1/2\,(d-M(\Phi_{\mathrm{L}}+g_{\mathrm{NL}}\Phi_{\mathrm{L}}^3))^\dagger\left[N^{-1}-\frac{\sigma_{f_{\mathrm{NL}}}^2 N^{-1}M(\Phi_{\mathrm{L}}^2-\langle\Phi_{\mathrm{L}}^2\rangle)(\Phi_{\mathrm{L}}^2-\langle\Phi_{\mathrm{L}}^2\rangle)^\dagger M^\dagger N^{-1}}{\sigma_{f_{\mathrm{NL}}}^2(\Phi_{\mathrm{L}}^2-\langle\Phi_{\mathrm{L}}^2\rangle)^\dagger M^\dagger N^{-1}M(\Phi_{\mathrm{L}}^2-\langle\Phi_{\mathrm{L}}^2\rangle)+1}\right]} \\
&\quad {}^{\times(d-M(\Phi_{\mathrm{L}}+g_{\mathrm{NL}}\Phi_{\mathrm{L}}^3))-1/2\,\Phi_{\mathrm{L}}^\dagger P_\Phi^{-1}\Phi_{\mathrm{L}}}\,.
\end{aligned}
\tag{B.7}
$$

Introducing the modified noise covariance matrix $\widetilde{N}$ as a shorthand,

$$
\widetilde{N}^{-1} \equiv N^{-1} - \frac{\sigma_{f_{\mathrm{NL}}}^2 N^{-1}M(\Phi_{\mathrm{L}}^2-\langle\Phi_{\mathrm{L}}^2\rangle)(\Phi_{\mathrm{L}}^2-\langle\Phi_{\mathrm{L}}^2\rangle)^\dagger M^\dagger N^{-1}}{\sigma_{f_{\mathrm{NL}}}^2(\Phi_{\mathrm{L}}^2-\langle\Phi_{\mathrm{L}}^2\rangle)^\dagger M^\dagger N^{-1}M(\Phi_{\mathrm{L}}^2-\langle\Phi_{\mathrm{L}}^2\rangle)+1}\,,
\tag{B.8}
$$

122

we now marginalize over the remaining parameter of non-Gaussianity, g_{NL},

$$P(\Phi, |d, \theta) \propto \left[\sigma_{f_{\mathrm{NL}}}^2 (\Phi_{\mathrm{L}}^2 - \langle \Phi_{\mathrm{L}}^2 \rangle)^\dagger M^\dagger N^{-1} M (\Phi_{\mathrm{L}}^2 - \langle \Phi_{\mathrm{L}}^2 \rangle) + 1\right]^{-1/2}$$
$$\times \mathrm{e}^{-1/2\,(d - M\Phi_{\mathrm{L}})^\dagger \widetilde{N}^{-1}(d - M\Phi_{\mathrm{L}}) - 1/2\,\Phi_{\mathrm{L}}^\dagger P_\Phi^{-1}\Phi_{\mathrm{L}}}$$
$$\times \int dg_{\mathrm{NL}}\, \mathrm{e}^{g_{\mathrm{NL}}\Phi_{\mathrm{L}}^{3\dagger}M^\dagger \widetilde{N}^{-1}(d - M\Phi_{\mathrm{L}}) - 1/2\,g_{\mathrm{NL}}^2 \Phi_{\mathrm{L}}^{3\dagger}M^\dagger \widetilde{N}^{-1}M\Phi_{\mathrm{L}}^3 - g_{\mathrm{NL}}^2/2\sigma_{g_{\mathrm{NL}}}^2}$$

$$= \left[\sigma_{f_{\mathrm{NL}}}^2 (\Phi_{\mathrm{L}}^2 - \langle \Phi_{\mathrm{L}}^2 \rangle)^\dagger M^\dagger N^{-1} M (\Phi_{\mathrm{L}}^2 - \langle \Phi_{\mathrm{L}}^2 \rangle) + 1\right]^{-1/2}$$
$$\times \mathrm{e}^{-1/2\,(d - M\Phi_{\mathrm{L}})^\dagger \widetilde{N}^{-1}(d - M\Phi_{\mathrm{L}}) - 1/2\,\Phi_{\mathrm{L}}^\dagger P_\Phi^{-1}\Phi_{\mathrm{L}}}$$
$$\times \int dg_{\mathrm{NL}}\, \mathrm{e}^{-\frac{(g_{\mathrm{NL}} - \bar{g}_{\mathrm{NL}})^2}{2\bar{\sigma}_{g_{\mathrm{NL}}}} + \frac{\bar{g}_{\mathrm{NL}}^2}{2\bar{\sigma}_{g_{\mathrm{NL}}}}}\,,$$

thus,

$$P(\Phi, |d, \theta) \propto \left[\sigma_{f_{\mathrm{NL}}}^2 (\Phi_{\mathrm{L}}^2 - \langle \Phi_{\mathrm{L}}^2 \rangle)^\dagger M^\dagger N^{-1} M (\Phi_{\mathrm{L}}^2 - \langle \Phi_{\mathrm{L}}^2 \rangle) + 1\right]^{-1/2}$$
$$\times \left[\sigma_{g_{\mathrm{NL}}}^2 \Phi_{\mathrm{L}}^{3\dagger} M^\dagger \widetilde{N}^{-1} M \Phi_{\mathrm{L}}^3 + 1\right]^{-1/2}$$
$$\times \mathrm{e}^{-1/2\,(d - M\Phi_{\mathrm{L}})^\dagger \left[\widetilde{N}^{-1} - \frac{\sigma_{g_{\mathrm{NL}}}^2 \widetilde{N}^{-1} M \Phi_{\mathrm{L}}^3 \Phi_{\mathrm{L}}^{3\dagger} M^\dagger \widetilde{N}^{-1}}{\sigma_{g_{\mathrm{NL}}}^2 \Phi_{\mathrm{L}}^{3\dagger} M^\dagger \widetilde{N}^{-1} M \Phi_{\mathrm{L}}^3 + 1}\right](d - M\Phi_{\mathrm{L}}) - 1/2\,\Phi_{\mathrm{L}}^\dagger P_\Phi^{-1}\Phi_{\mathrm{L}}}\,.$$
$$(\mathrm{B.9})$$

The sampling recipe to simultaneously infer f_{NL} and g_{NL} can now be summarized as follows,

$$\Phi_{\mathrm{L}}^i \hookleftarrow P(\Phi_{\mathrm{L}}|d, \theta)$$
$$f_{\mathrm{NL}}^i \hookleftarrow P(f_{\mathrm{NL}}|d, \Phi_{\mathrm{L}}^i, g_{\mathrm{NL}}^{i-1}, \theta)$$
$$g_{\mathrm{NL}}^i \hookleftarrow P(g_{\mathrm{NL}}|d, \Phi_{\mathrm{L}}^i, f_{\mathrm{NL}}^i, \theta)\,. \qquad (\mathrm{B.10})$$

Again, we propose a Hamiltonian Monte Carlo sampler to obtain valid realizations of Φ_{L}, and to draw the parameters of non-Gaussianity from their Gaussian probability distribution given by Eq. B.4 et seq.

Bibliography

Abbott, L. F., Farhi, E., & Wise, M. B. 1982, Physics Letters B, 117, 29

Abbott, L. F. & Wise, M. B. 1984, Nuclear Physics B, 244, 541

Acquaviva, V., Bartolo, N., Matarrese, S., & Riotto, A. 2003, Nuclear Physics B, 667, 119

Ade, P., Bock, J., Bowden, M., et al. 2008, ApJ, 674, 22

Aghanim, N., Majumdar, S., & Silk, J. 2008, Reports on Progress in Physics, 71, 066902

Albrecht, A. & Steinhardt, P. J. 1982, Physical Review Letters, 48, 1220

Armendáriz-Picón, C., Damour, T., & Mukhanov, V. 1999, Physics Letters B, 458, 209

Ashtekar, A. & Tate, R. S. 1991, Lectures on non-pertubrative canonical gravity (Singapore: World Scientific)

Assadullahi, H., Väliviita, J., & Wands, D. 2007, Phys. Rev. D, 76, 103003

Babich, D., Creminelli, P., & Zaldarriaga, M. 2004, J. Cosmology Astropart. Phys., 8, 9

Babich, D. & Pierpaoli, E. 2008, Phys. Rev. D, 77, 123011

Bardeen, J. M. 1980, Phys. Rev. D, 22, 1882

Bardeen, J. M., Steinhardt, P. J., & Turner, M. S. 1983, Phys. Rev. D, 28, 679

Barrow, J. D. & Ottewill, A. C. 1983, Journal of Physics A Mathematical General, 16, 2757

Bartolo, N., Komatsu, E., Matarrese, S., & Riotto, A. 2004, Phys. Rep., 402, 103

Bartolo, N., Matarrese, S., Pietroni, M., Riotto, A., & Seery, D. 2008, J. Cosmology Astropart. Phys., 1, 15

Bartolo, N., Matarrese, S., & Riotto, A. 2010, ArXiv e-prints

Baumann, D. 2009, ArXiv e-prints

Bayes, T. & Price, R. 1763, Phil. Trans., 53, 370

Beneke, M. & Fidler, C. 2010, ArXiv e-prints

Bennett, C. L., Banday, A. J., Gorski, K. M., et al. 1996, ApJ, 464, L1+

Bennett, C. L., Halpern, M., Hinshaw, G., et al. 2003a, ApJS, 148, 1

Bennett, C. L., Hill, R. S., Hinshaw, G., et al. 2003b, ApJS, 148, 97

Bolstad, W. M. 2007, Introduction to Bayesian statistics (Hoboken, NY: Wiley)

Borde, A. & Vilenkin, A. 1994, Physical Review Letters, 72, 3305

Brandenberger, R. H. 1999, ArXiv High Energy Physics - Phenomenology e-prints

Brandenberger, R. H. 2010, ArXiv e-prints

Buchbinder, E. I., Khoury, J., & Ovrut, B. A. 2007, Phys. Rev. D, 76, 123503

Bunch, T. S. & Davies, P. C. W. 1978, Royal Society of London Proceedings Series A, 360, 117

Burgess, C. P. 2007, Classical and Quantum Gravity, 24, 795

Byrnes, C. T., Sasaki, M., & Wands, D. 2006, Phys. Rev. D, 74, 123519

Castro, P. G. 2003, Phys. Rev. D, 67, 123001

Chen, X. 2010, ArXiv e-prints

Chen, X., Huang, M., Kachru, S., & Shiu, G. 2007, J. Cosmology Astropart. Phys., 1, 2

Choi, K. & Gong, J. 2007, J. Cosmology Astropart. Phys., 6, 7

Coleman, S. & Weinberg, E. 1973, Phys. Rev. D, 7, 1888

Colless, M. 1999, Royal Society of London Philosophical Transactions Series A, 357, 105

Copeland, E. J., Liddle, A. R., Lyth, D. H., Stewart, E. D., & Wands, D. 1994, Phys. Rev. D, 49, 6410

Cox, R. T. 1946, American Journal of Physics, 14, 1

Creminelli, P. & Senatore, L. 2007, J. Cosmology Astropart. Phys., 11, 10

Creminelli, P., Senatore, L., & Zaldarriaga, M. 2007, J. Cosmology Astropart. Phys., 3, 19

Creminelli, P. & Zaldarriaga, M. 2004, J. Cosmology Astropart. Phys., 10, 6

da Costa, L. N., Willmer, C. N. A., Pellegrini, P. S., et al. 1998, AJ, 116, 1

Dodelson, S. 2003, Modern Cosmology (Amsterdam: Academic Press (Elsevier))

Easther, R., Greene, B. R., Kinney, W. H., & Shiu, G. 2001, Phys. Rev. D, 64, 103502

Easther, R., Greene, B. R., Kinney, W. H., & Shiu, G. 2002, Phys. Rev. D, 66, 023518

Efstathiou, G., Lawrence, C., & J., T. 2005, Planck. The Scientific Program, Planck Science Team, `http://www.rssd.esa.int/SA/PLANCK/docs/Bluebook-ESA-SCI%282005%291_V2.pdf`

Einstein, A. 1916, Annalen der Physik, 354, 769

Eisenstein, D. J., Zehavi, I., Hogg, D. W., et al. 2005, ApJ, 633, 560

Enqvist, K. & Nurmi, S. 2005, J. Cosmology Astropart. Phys., 10, 13

Enqvist, K., Nurmi, S., Taanila, O., & Takahashi, T. 2010, J. Cosmology Astropart. Phys., 4, 9

Enqvist, K. & Sloth, M. S. 2002, Nuclear Physics B, 626, 395

Erickson, J. K., Gratton, S., Steinhardt, P. J., & Turok, N. 2007, Phys. Rev. D, 75, 123507

Fabbri, R. & Pollock, M. D. 1983, Physics Letters B, 125, 445

Fergusson, J. R. & Shellard, E. P. S. 2009, Phys. Rev. D, 80, 043510

Finkbeiner, D. P. 2003, ApJS, 146, 407

Finkbeiner, D. P., Davis, M., & Schlegel, D. J. 1999, ApJ, 524, 867

Fixsen, D. J., Cheng, E. S., Gales, J. M., et al. 1996, ApJ, 473, 576

Friedmann, A. 1922, Zeitschrift für Physik, 10, 377

Friedmann, A. 1924, Zeitschrift für Physik, 21, 326

Frieman, J. A. 1994, in Building Blocks of Creation, From Microfermis to Megaparsecs, ed. S. Raby & T. Walker, 421–+

Ganc, J. & Komatsu, E. 2010, ArXiv e-prints

Gangui, A., Lucchin, F., Matarrese, S., & Mollerach, S. 1994, ApJ, 430, 447

Garriga, J. & Mukhanov, V. F. 1999, Physics Letters B, 458, 219

Gill, J. 2002, Bayesian methods (Roca: Chapman & Hall/CRC)

Gold, B., Bennett, C. L., Hill, R. S., et al. 2009, ApJS, 180, 265

Goldberg, D. M. & Spergel, D. N. 1999, Phys. Rev. D, 59, 103002

Gordon, C., Wands, D., Bassett, B. A., & Maartens, R. 2001, Phys. Rev. D, 63, 023506

Green, M. B., Schwarz, J. H., & Witten, E. 1986, Superstring theory (Cambridge: Cambridge University Press)

Gregory, P. C., Scott, W. K., Douglas, K., & Condon, J. J. 1996, ApJS, 103, 427

Griffith, M. R. & Wright, A. E. 1993, AJ, 105, 1666

Guth, A. H. 1981, Phys. Rev. D, 23, 347

Guth, A. H. & Pi, S. 1982, Phys. Rev. Lett., 49, 1110

Hanson, D., Smith, K. M., Challinor, A., & Liguori, M. 2009, Phys. Rev. D, 80, 083004

Haslam, C. G. T., Klein, U., Salter, C. J., et al. 1981, A&A, 100, 209

Hawking, S. W. 1982, Physics Letters B, 115, 295

Hawking, S. W. & Penrose, R. 1970, Royal Society of London Proceedings Series A, 314, 529

Hobson, M. P., Jaffe, A. H., Liddle, A. R., Mukherjee, P., & Parkinson, D. 2010, Bayesian methods in cosmology (Cambridge: Cambridge University Press)

Hořava, P. & Witten, E. 1996, Nuclear Physics B, 475, 94

Huang, Q. 2008, J. Cosmology Astropart. Phys., 11, 5

Hubble, E. 1929, Proceedings of the National Academy of Science, 15, 168

Huchra, J., Davis, M., Latham, D., & Tonry, J. 1983, ApJS, 52, 89

Jarosik, N., Bennett, C. L., Dunkley, J., et al. 2010, ArXiv e-prints

Jenet, F. A., Hobbs, G. B., van Straten, W., et al. 2006, ApJ, 653, 1571

Jones, D. H., Saunders, W., Colless, M., et al. 2004, MNRAS, 355, 747

Kallosh, R., Kang, J. U., Linde, A., & Mukhanov, V. 2008, J. Cosmology Astropart. Phys., 4, 18

Kallosh, R., Kofman, L., & Linde, A. 2001, Phys. Rev. D, 64, 123523

Khatri, R. & Wandelt, B. D. 2009, Phys. Rev. D, 79, 023501

Khoury, J., Ovrut, B. A., Seiberg, N., Steinhardt, P. J., & Turok, N. 2002, Phys. Rev. D, 65, 086007

Khoury, J., Ovrut, B. A., Steinhardt, P. J., & Turok, N. 2001, Phys. Rev. D, 64, 123522

Kinney, W. H. 2009, ArXiv e-prints

Kofman, L., Linde, A., & Starobinskiĭ, A. A. 1994, Physical Review Letters, 73, 3195

Kofman, L., Linde, A., & Starobinskiĭ, A. A. 1997, Phys. Rev. D, 56, 3258

Komatsu, E., Kogut, A., Nolta, M. R., et al. 2003, ApJS, 148, 119

Komatsu, E., Smith, K. M., Dunkley, J., et al. 2010, ArXiv e-prints

Komatsu, E. & Spergel, D. N. 2001, Phys. Rev. D, 63, 063002

Komatsu, E., Spergel, D. N., & Wandelt, B. D. 2005, ApJ, 634, 14

Koyama, K., Mizuno, S., Vernizzi, F., & Wands, D. 2007a, J. Cosmology Astropart. Phys., 11, 24

Koyama, K., Mizuno, S., & Wands, D. 2007b, ArXiv e-prints

Koyama, K. & Wands, D. 2007, J. Cosmology Astropart. Phys., 4, 8

Kuo, C. L., Ade, P. A. R., Bock, J. J., et al. 2004, ApJ, 600, 32

Lehners, J. 2010, ArXiv e-prints

Lehners, J., McFadden, P., Turok, N., & Steinhardt, P. J. 2007, Phys. Rev. D, 76, 103501

Lehners, J. & Renaux-Petel, S. 2009, Phys. Rev. D, 80, 063503

Leitch, E. M., Kovac, J. M., Halverson, N. W., et al. 2005, ApJ, 624, 10

Lemaître, G. 1927, Annales de la Societe Scietifique de Bruxelles, 47, 49

Leonard, T. & Hsu, J. S. J. 2001, Bayesian methods (Cambridge: Cambridge University press)

130

Liddle, A. R. & Lyth, D. H. 2000, Cosmological Inflation and Large-Scale Structure (Cambridge: Cambridge University press)

Liguori, M., Sefusatti, E., Fergusson, J. R., & Shellard, E. P. S. 2010, ArXiv e-prints

Liguori, M., Yadav, A., Hansen, F. K., et al. 2007, Phys. Rev. D, 76, 105016

Linde, A. 1990a, Physics Letters B, 249, 18

Linde, A. 2008, in Lecture Notes in Physics, Berlin Springer Verlag, Vol. 738, Lecture Notes in Physics, Berlin Springer Verlag, ed. M. Lemoine, J. Martin, & P. Peter, 1–+

Linde, A. & Mukhanov, V. 1997, Phys. Rev. D, 56, 535

Linde, A., Mukhanov, V., & Vikman, A. 2010, J. Cosmology Astropart. Phys., 2, 6

Linde, A. D. 1982, Physics Letters B, 108, 389

Linde, A. D. 1983, Physics Letters B, 129, 177

Linde, A. D. 1990b, Particle Physics and Inflationary Cosmology (Chur: Harwood Academic Publishers)

Lukas, A., Ovrut, B. A., Stelle, K. S., & Waldram, D. 1999a, Nuclear Physics B, 552, 246

Lukas, A., Ovrut, B. A., Stelle, K. S., & Waldram, D. 1999b, Phys. Rev. D, 59, 086001

Lüst, D. & Theisen, S. 1989, Lectures on String Theory (Berlin: Springer)

Lyth, D. H. 1997, Physical Review Letters, 78, 1861

Lyth, D. H. 2002, Physics Letters B, 526, 173

Lyth, D. H. 2007, J. Cosmology Astropart. Phys., 12, 16

Lyth, D. H., Malik, K. A., & Sasaki, M. 2005, J. Cosmology Astropart. Phys., 5, 4

Lyth, D. H. & Riotto, U. 1999, 314, 1

Lyth, D. H. & Rodríguez, Y. 2005, Physical Review Letters, 95, 121302

Lyth, D. H., Ungarelli, C., & Wands, D. 2003, Phys. Rev. D, 67, 023503

Lyth, D. H. & Wands, D. 2002, Physics Letters B, 524, 5

MacKay, D. 2005, Information theory, inference, and learning algorithms (Cambridge: Cambridge University press)

Maldacena, J. 2003, Journal of High Energy Physics, 5, 13

Mangilli, A. & Verde, L. 2009, Phys. Rev. D, 80, 123007

Mollerach, S. 1990, Phys. Rev. D, 42, 313

Moroi, T. & Takahashi, T. 2001, Physics Letters B, 522, 215

Mukhanov, V. F. 1985, Soviet Journal of Experimental and Theoretical Physics Letters, 41, 493

Mukhanov, V. F. 2005, Physical Foundations of Cosmology (Cambridge: Cambridge University press)

Mukhanov, V. F. & Chibisov, G. V. 1981, Soviet Journal of Experimental and Theoretical Physics Letters, 33, 532

Mukhanov, V. F., Feldman, H. A., & Brandenberger, R. H. 1992, Phys. Rep., 215, 203

Munshi, D., Valageas, P., Cooray, A., & Heavens, A. 2009, ArXiv e-prints

Netterfield, C. B., Ade, P. A. R., Bock, J. J., et al. 2002, ApJ, 571, 604

Notari, A. & Riotto, A. 2002, Nuclear Physics B, 644, 371

Peacock, J. A., Cole, S., Norberg, P., et al. 2001, Nature, 410, 169

Penzias, A. A. & Wilson, R. W. 1965, ApJ, 142, 419

Pitrou, C. 2009, Classical and Quantum Gravity, 26, 065006

Pitrou, C., Uzan, J., & Bernardeau, F. 2010, ArXiv e-prints

Rees, M. J. & Sciama, D. W. 1968, Nature, 217, 511

Rigopoulos, G. I. & Shellard, E. P. S. 2003, Phys. Rev. D, 68, 123518

Robertson, H. P. 1935, ApJ, 82, 284

Robertson, H. P. 1936a, ApJ, 83, 187

Robertson, H. P. 1936b, ApJ, 83, 257

Rovelli, C. 1998, Living Reviews in Relativity, 1, 1

Ryder, L. H. 1996, Quantum field theory (Cambridge: Cambridge University press)

Sachs, R. K. & Wolfe, A. M. 1967, ApJ, 147, 73

Sahni, V. 1990, Phys. Rev. D, 42, 453

Salopek, D. S. & Bond, J. R. 1990, Phys. Rev. D, 42, 3936

Sasaki, M. & Stewart, E. D. 1996, Progress of Theoretical Physics, 95, 71

Sasaki, M., Väliviita, J., & Wands, D. 2006, Phys. Rev. D, 74, 103003

Sato, K. 1981, MNRAS, 195, 467

Serra, P. & Cooray, A. 2008, Phys. Rev. D, 77, 107305

Shiu, G. & Wasserman, I. 2002, Physics Letters B, 536, 1

Sievers, J. L., Bond, J. R., Cartwright, J. K., et al. 2003, ApJ, 591, 599

Slosar, A., Hirata, C., Seljak, U., Ho, S., & Padmanabhan, N. 2008, J. Cosmology Astropart. Phys., 8, 31

Smidt, J., Amblard, A., Cooray, A., et al. 2010, ArXiv e-prints

Smith, K. M., Senatore, L., & Zaldarriaga, M. 2009, J. Cosmology Astropart. Phys., 9, 6

Smoot, G. F., Bennett, C. L., Kogut, A., et al. 1992, ApJ, 396, L1

Spergel, D. N. & Goldberg, D. M. 1999, Phys. Rev. D, 59, 103001

Spergel, D. N., Verde, L., Peiris, H. V., et al. 2003, ApJS, 148, 175

Starobinskiĭ, A. A. 1979, Soviet Journal of Experimental and Theoretical Physics Letters, 30, 682

Starobinskiĭ, A. A. 1980, Physics Letters B, 91, 99

Starobinskiĭ, A. A. 1982, Physics Letters B, 117, 175

Starobinskiĭ, A. A. 1983, Soviet Astronomy Letters, 9, 302

Starobinskiĭ, A. A. 1985, Soviet Journal of Experimental and Theoretical Physics Letters, 42, 152

Steinhardt, P. J. & Turok, N. 2002a, Science, 296, 1436

Steinhardt, P. J. & Turok, N. 2002b, Phys. Rev. D, 65, 126003

Sunyaev, R. A. & Zeldovich, Y. B. 1970, Ap&SS, 7, 3

The LIGO Collaboration & The Virgo Collaboration. 2009, Nature, 460, 990

Thiemann, T. 2001, ArXiv General Relativity and Quantum Cosmology e-prints

Tseliakhovich, D., Hirata, C., & Slosar, A. 2010, ArXiv e-prints

Verde, L. & Spergel, D. N. 2002, Phys. Rev. D, 65, 043007

Vielva, P. & Sanz, J. L. 2009, MNRAS, 397, 837

Walker, A. G. 1935, MNRAS, 95, 263

Wands, D. 2010, ArXiv e-prints

Weinberg, S. 1996, The quantum theory of fields (Cambridge: Cambridge University press)

Weinberg, S. 2008, Cosmology (Oxford: Oxford University press)

Witten, E. 1996, Nuclear Physics B, 471, 135

Wright, E. L., Meyer, S. S., Bennett, C. L., et al. 1992, ApJ, 396, L13

134

Yadav, A. P. S., Komatsu, E., & Wandelt, B. D. 2007, ApJ, 664, 680

York, D. G., Adelman, J., Anderson, Jr., J. E., et al. 2000, AJ, 120, 1579

Zee, A. 2003, Quantum field theory in a nutshell (Princeton: Princeton University Press)

Zwiebach, B. 2004, A first course in string theory (Cambridge: Cambridge University Press)

Acknowledgements